Dissecting the direct projection from the medial septum to the grid cell network

by

Mina Martine Frey

Thesis

for the degree of Master in Molecular Biosciences

Main field

in neurobiology

60 credits

Program for Molecular Biology

Department of Biosciences

Faculty of Mathematics and Natural Sciences

UNIVERSITY OF OSLO

2017

Acknowledgements

Summary

The medial entorhinal cortex (MEC) spatially modulated neurons, including grid cells, all contribute to the brain's spatial navigation system. The mechanisms behind the grid cells' hexagonal firing pattern in space remain elusive. One question pertains to how distal inputs modulate the grid cell network. The medial septum (MS) densely innervates the MEC and pharmacological inactivation of the MS is found to disrupt the spatial periodicity of grid cell firing and the local field potential (LFP) theta oscillations. The spiking activity of grid cells is in synchrony with the ongoing LFP theta oscillations, suggesting a relationship. In contrast, this relation is not found in bats that seem to lack theta activity, indicating that grid cell activity may be independent of theta oscillations. The MS projection to the MEC consists of inhibitory and excitatory neurons but their relative contributions are not well understood. Moreover, the postsynaptic targets of the MS projections in the MEC have not been thoroughly mapped out. The aim of the present study was to investigate the role of the MS projection in the grid cell network by anatomical and functional assessment of the connectivity of MS projections onto neurons in the MEC. To investigate the contribution of inhibitory and excitatory MS terminals in the MEC, we expressed a fluorescent tag together with the presynaptic component synaptophysin in rat MS neurons by use of a viral vector. Neurochemical mapping was conducted on brain sections for the characterisation of pre-and postsynaptic cells in the MEC. Co-localisation analyses were conducted from confocal images obtained from MEC layer II (LII) and III (LIII). To investigate how perturbations of the MS projection affected single unit and LFP activity in the MEC, we performed optogenetic perturbations of the MS projection and simultaneous electrophysiological recordings in the MEC. The preliminary neuroanatomical findings in the current study suggest that about 80% of MS terminals in the MEC are GABAergic. The postsynaptic targets of the projection are both calbindin positive pyramidal LII cells and parvalbumin positive LII and LIII cells. The parvalbumin positive cells in LII received nearly double the input compared to the other two cell populations. The optogenetic perturbations of the MS projections indicated that the grid cells' firing rate increased with increased power in the LFP theta with no change in the spatial modulation. Activating the MS-MEC projection caused an instantaneous inhibition of narrow spiking putative interneurons, whereas grid cells

showed a delayed increase in response to activation. The anatomical findings suggest direct inhibition of the MS projection onto PV positive interneurons most prominently in MEC LII. Preliminary data from the electrophysiology suggest that the spatial coding of grid cells may be dissociated from LFP theta oscillations, and that the MS may act in disinhibition of the grid cells, through long-range inhibitory neurons.

Preface

My master's project was accomplished in collaboration with PhD candidate Mikkel Lepperød, as part of his research project. The project is partly experimental and partly computational, in which I contributed to the experimental part. In terms of the time constraints of a master's project and the complexity of the major project, we decided to divide the tasks between us. Kristian Lensjø and I did tissue preparations, histology, immunohistochemistry and imaging. Mattis Wigestrand prepared the viral constructs used for anatomical tracing and optogenetic experiments. The surgical procedures were conducted by M. Lepperød and Marianne Fyhn, with my assistance. Kristian Lensjø helped me with the imaging, as well as the first perfusions. The data analysis involving spike sorting and wave form analysis was performed by M. Lepperød, while I did the co-localisation analysis. Alessio Buccino and M. Lepperød wrote a program, enabling optogenetic stimulation inside and outside grid fields. Both M. Lepperød and I contributed to the electrophysiological recordings, and made the optetrode microdrives for electrophysiological recordings and optogenetics.

Contents

1   Introduction

Navigation is the ability to plan and perform a goal-directed path. Activities and behaviours of navigation indicate an internal spatial reference system represented as a 'cognitive map'. Regardless of whether moving over large distances or in unfamiliar environments, the internal map is both anchored to external landmarks and based on self-motion (path integration) (reviewed by McNaughton et al. 2006). Such navigation is found in a great number of species; for example the desert ant, *Cataglyphis fortis*, keeps track of its position relative to its nest, and is able to return straight home after a long journey over featureless terrain (reviewed by Etienne and Jeffery 2004). Navigation depends on position, distance, direction and speed, and is found to be involved in context-dependent episodic memory (Rowland et al., 2016).

1.1   The link between navigation and memory

When we recollect experienced events, the memory circumscribes the "what", "where" and "when" of the event, which forms the basis of episodic memory (Tulving et al., 1972). The function of the hippocampus has been dominated by two major views; as critical for declarative memory formation – retrieving specific experiences and episodic memory (Scoville and Milner, 1957), as well as a role in a spatial reference system (O'Keefe and Nadel, 1978). The importance of the hippocampus for declarative memory processing started with studies of patient Henry Molaison's (H.M.), in which removal of medial temporal lobe structures, including the hippocampus, lead to anterograde amnesia (Scoville and Milner, 1957; Annese et al., 2014). The lesions were subsequently found to impair a number of spatial tasks (Corkin, 1979). Positron emission tomography studies of London taxi drivers have shown activation of hippocampal and parahippocampal regions during virtual navigation in the streets of London (Maguire et al., 1997), and navigational impairments in one driver with bilateral hippocampal lesions (Maguire et al., 2006). Studies in rats with hippocampal or parahippocampal lesions demonstrate that rats fail to find a hidden platform previously visited, in the Morris water maze task (Morris et al., 1982; Steffenach et al., 2005).

O'Keefe and Dostrovsky (1971) performed electrophysiological recordings of hippocampal cells in rats as they navigated an open field. The study revealed specific cells determined by the location of the animal. The cells fire in a given area, a 'place field', within the environment, and were named 'place cells'. The conjoined firing of numerous place cells is thought to give the animal a representation of the current location (Wilson and McNaughton, 1993), and an internal map of the local environment (O'Keefe and Nadel, 1978). A seminal paper showed that removing the input from dorsal cornu ammonis (CA) 3 to the CA1, did not change the spatial firing of place cells, suggesting that spatial computations are not solely intrahippocampal (Brun, 2002).

One major input structure to the dorsal CA1 is the dorsal medial entorhinal cortex (MEC) (Witter and Amaral, 2004). When recording from single units in the dorsal MEC, Fyhn and

co-workers (2004) found spatially modulated units – exhibiting more than one firing field within the recording arena (fig. 1.1). Increasing the area of the recording arena led to the discovery that firing fields of these neurons were at vertices of equilateral triangles, creating a hexagonal pattern tessellating the entire 2D space of the environment. The cells were named 'grid cells' (Hafting et al., 2005).
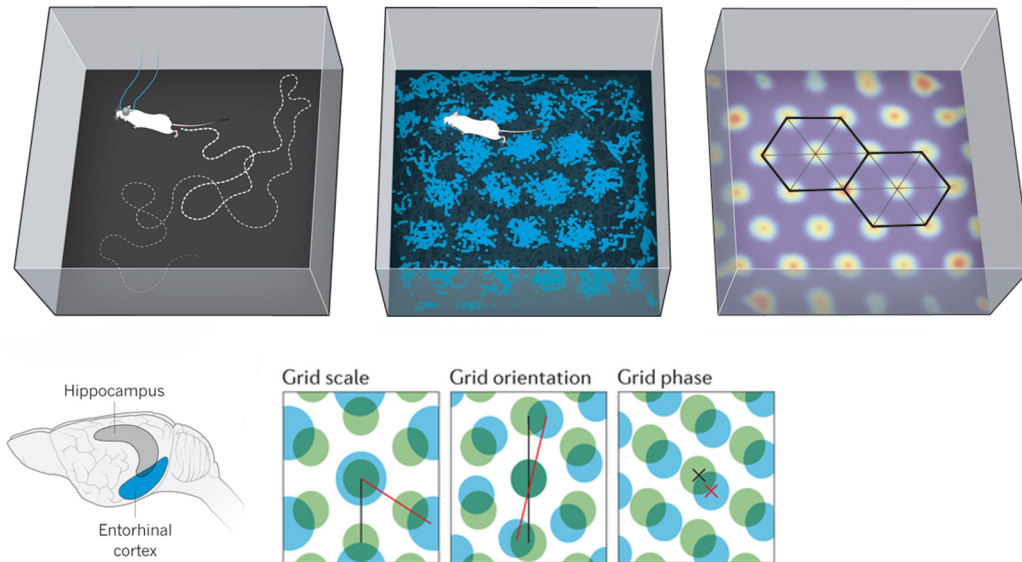
Figure 1.1: Properties of grid cells. Electrophysiological recordings of the firing pattern of grid cells in birds eye view of the recording space (top). The activity pattern of the grid cells is shown as action potentials (blue) and firing rates (red/yellow) along the animal's trajectory revealing spatial periodicity at vertices of equilateral triangles. Grid cells are found in the entorhinal cortex (bottom left), and form discrete modules (bottom right), sharing a common scale, orientation and phase. The grid scale expands from the dorsal to the ventral medial entorhinal cortex. Adapted from Abbott (2014) and Moser et al. (2014).

1.1.1 Spatially modulated cells in the medial entorhinal cortex

Understanding computation in the association cortices, such as the MEC, is a daunting challenge in neuroscience, due to a vast number of firing correlates and the multiple inputs from sensory sources (McNaughton et al., 2006). The MEC is proposed to be the hub of a distributed neural network containing functionally different cell types such as grid cells, place cells, head-direction cells (Sargolini et al., 2006), border cells (Solstad et al., 2008) and speed cells (Kropff et al., 2015) that together represent a navigation system that can aid in animal navigation. The MEC displays a laminar organisation of six layers, divided into the superficial (I-III) and the deep (V-VI) layers. Layer I and IV contains few neurons (Dolorfo and Amaral, 1998). The grid cells were discovered in the dorsal MEC. They are found in layer II, III, V

and VI of the MEC, throughout the DV axis, and in the pre- and parasubiculum (Sargolini et al., 2006; Brun et al., 2008; Stensola et al., 2012). The waveforms and firing rates of grid cells, head direction cells and border cells suggests that they are excitatory principal cells.

The firing fields of grid cells (grid fields) are found to vary in size, spacing and orientation relative to the environment. Each cell has a slight shift in environmental x, y-coordinates, and with a small number of grid cells the firing fields cover the entire environment (Hafting et al., 2005). The spacing of grid fields is topographically organised in the dorsoventral (DV) axis. In the dorsal most part of the MEC the grid fields are smaller and more densely packed, whereas the scale expands towards more ventral parts (Fig. 1.1) (Fyhn et al., 2004; Hafting et al., 2005; Brun et al., 2008). Interestingly populations of grid cells maintain orientation relationship and phase despite shift in environmental input (Fyhn et al., 2007). By recording from many grid cells simultaneously across layers and along DV axis, Stensola and co-workers (2012) found that grid cells form discrete modules of specific spacings and orientations. These anatomically overlapping modules are clusters of cells sharing (fig. 1.1) temporal relation to the local field potential (described in section 1.2). As the MEC is both projecting and receiving synaptic connections from the hippocampus, this lead to the suggestion that grid cells might be involved in the input mechanisms of path-integration and self-motion to place cells in the hippocampus, independent of external cues (Hafting et al., 2005). Following the discovery of grid cells in rats, the cells were found in mice (Fyhn et al., 2008), bats (Yartsev et al., 2011), primates (Killian et al., 2012) and humans (Doeller et al., 2010; Jacobs et al., 2013; Kunz et al., 2015), suggesting that a similar mechanism for spatial representation is evolutionary conserved across mammals.

Several other functionally dedicated cell types in the MEC accompany the grid cells. Head direction cells (Sargolini et al., 2006; Boccara et al., 2010) encode head direction of the animal independent of location in the horizontal plane. Speed cells (Kropff et al., 2015) respond to running speed by proportional increase in firing rate. Together grid cells, head direction cells and speed cells are thought to be involved in context-invariant navigation (Rowland et al., 2016). Another defined cell type found in the MEC is the border cells (Solstad et al., 2008), firing action potentials when the animal is close to environmental borders. Border cells are thought to represent a geometric reference frame for planning trajectories and anchoring grid fields and place fields.

1.2   Theta oscillations and local field potential

Oscillations (brain rhythms) provide a mechanism for coordinating the activity of ensembles of neurons and neurons from different brain areas. Simultaneous electrophysiological recordings in the hippocampus and MEC during exploratory behaviour reveal low frequency oscillations of large amplitude and sinusoidal regularity. The oscillating activity is in the frequency range of 4-12 Hz, known as theta activity. A vast number of studies implicate theta oscillations importance for spatial learning and the grid cell network (reviewed by Colgin, 2016).

1.2.1   Local field potential

The activity of cellular processes in a volume of brain tissue impose electric currents in the extracellular medium. Oscillating activity is generated by synchronized synaptic currents of low frequency, and can be measured electrophysiologically as sum of the electric activity, the local field potential (LFP). By placing electrodes extracellularly in neuronal tissue, the electric field can be measured with sub-millisecond time resolution (Buzsáki et al., 2012; Colgin, 2016). The lower frequencies are believed to attenuate less with distance in brain tissue than the high-frequency (>100 Hz) events of action potentials - therefore, low-frequency activity can be measured over larger distances in extracellular space. All excitable membranes, such as spines, dendrites, soma, axons, and axon terminals, yield extracellular potential at any given point in space, contributing to the LFP. The variation in contributions as well as the distance to the sources, interfering signals, and magnitude and temporal coordination of current sources compose the LFP waveform, including the amplitude and frequency (Buzsáki et al., 2012).

1.2.2   Theta oscillations and the medial septum

The theta oscillations were discovered in the rabbit hippocampus (Jung and Kornmüller, 1938). Since then it has been recorded in many mammalian species; including rats (Vanderwolf, 1969), bats (Ulanovsky and Moss, 2007) and humans (Ekstrom et al., 2005). The theta oscillations have been recorded in other cortical and sub-cortical areas of the brain as well (Mitchell and Ranck, 1980). Seven decades of extensive research on theta oscillations has led to a vast amount of theories on its behavioural significance, generally linked to active behaviour (Buzsáki, 2005).

The theta oscillations has long been thought to originate from pacemaker cells of the medial septum (MS), located in the basal forebrain. The MS sends dense projections to the hippocampus as well as all regions of the cortex with a particularly dense input to the entorhinal cortex (EC) (Alonso and Köhler, 1984). The MEC receives both inhibitory and excitatory MS input, from long-range Gamma-Aminobutyric acid (GABA)ergic, cholinergic (Alonso and Köhler, 1984) and glutamatergic neurons (Manns et al., 2001). Lesions or inactivation of the MS leads to abolishment or disruption of the theta oscillations in regions receiving MS projections (Green and Arduini, 1954; Petsche et al., 1962; Mitchell et al., 1982; Mizumori et al., 1990; Jeffery et al., 1995). Effects of such manipulations have been found to cause deficits in spatial learning and memory (Winson, 1978; Chrobak et al., 1989; Givens and Olton, 1994). The contribution of the MS projection is most extensively studied in the hippocampus, while less is known about its role in the MEC.

1.2.3   Theta oscillations and the grid cell network

The theta oscillations are believed to play an important role in the activity of cells in the MEC (fig. 1.2). The grid cells in layer II fired at progressively earlier phases, from the ascending to the descending slope of theta as the animal crossed the grid field (Hafting et al.,

2008). Hafting and co-workers (2008) found that grid cells' action potentials in the MEC layer II precess relative to the theta oscillations, whereas in layer III tended to be more phase locked to the theta oscillations. This way of coding in neural populations has been suggested to act in compression of temporal sequences (Skaggs et al., 1996). The phase precession in MEC persisted during hippocampal inactivation, suggesting a local or non-hippocampal origin (Hafting et al., 2008). Another study by Bonnevie et al. (2013) found disruption of grid cells spatial firing during inactivation of the hippocampus, and points to a possible excitatory drive from the hippocampus to the MEC. Temporary lesions or inactivation of the MS has been found to abolish the LFP theta oscillations in the MEC, and to alter the spatial periodicity of grid cells (Brandon et al., 2011; Koenig et al., 2011), but these studies used pharmacological methods in which it is difficult to account for possible effects on other brain regions receiving MS input. As a major MS projection goes to the hippocampus, and due to the reciprocal connectivity between the hippocampus and the MEC, the effect cannot be limited to solely be of a septal character.

Combining these studies with the supposition that MS is the generator of the theta oscillations (Green and Arduini, 1954; Petsche et al., 1962; Mitchell et al., 1982; Mizumori et al., 1990) has led to a field of interest in the connectivity of the MS-MEC projection and the function of this connection. Contradictory to the theta modulated grid cells found in rats (Hafting et al., 2008) and mice (Fyhn et al., 2008) are non-theta modulated grid cells found in bats (Egyptian fruit bat; Yartsev et al. 2011), which dissociates the link between grid cell firing and theta oscillations in the bat MEC.

The pharmacological approach used in previous studies (Brandon et al., 2011; Koenig et al., 2011) lack of specificity and temporal precision. Thus, in order to reveal the role of MS projections to the grid cell network, this needs to be revisited using targeted techniques such as optogenetic and genetic perturbations that overcome these limitations.

1.3   Connectivity of medial septal input to medial entorhinal cortex

It remains unresolved how the distal inputs of the MS connect to the intrinsic connectivity within the MEC. More extensively studied is the MEC local connectivity, which is explained before revealing the findings on the connectivity between MS and the MEC.

1.3.1   Local connectivity in the medial entorhinal cortex

There are two classes of excitatory neurons (principal cells) in the MEC; stellate cells and pyramidal cells. Stellate cells are found in MEC layer II, where grid cells are most abundant (Sargolini et al., 2006). Clusters of pyramidal cells are intermingled with stellate cells in layer II and constitute most of the excitatory neurons in other layers of the MEC(Ray et al., 2014). Intracellular recordings have revealed that both pyramidal cells and stellate cells are grid cells (Domnisoru et al., 2013; Sun et al., 2015). Layer II principal cells are subdivided
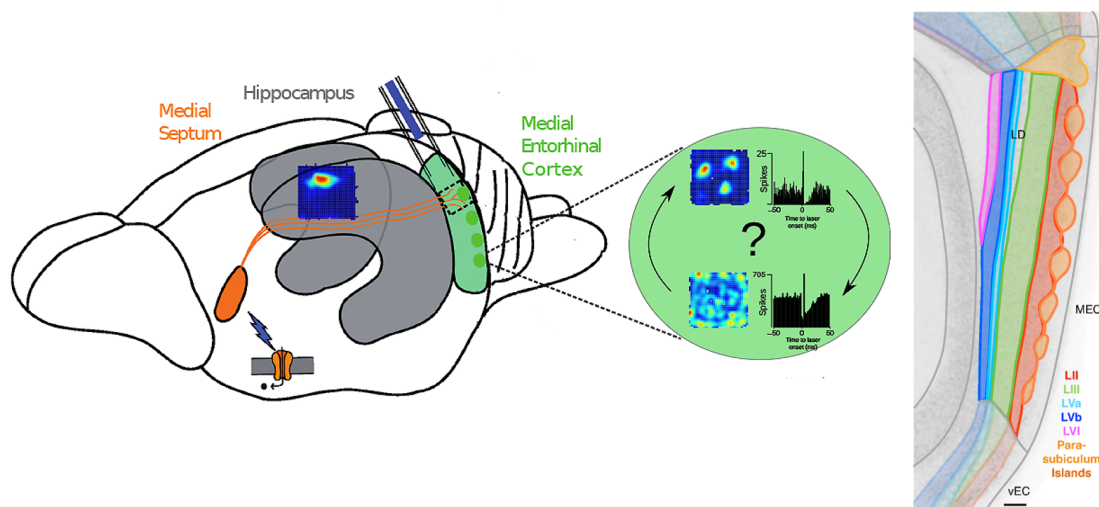
Figure 1.2: Distal input (left panel) from the medial septum projection in orange to the medial entorhinal cortex (MEC) in green. The rate maps show place cells in the hippocampus, and grid cells and interneurons in the MEC. The projection can be studied using optogenetics and simultaneously record the activity of cells in the MEC. The plots show spike time (ms) relative to light stimulations. Adapted from Monyer (2017). The MEC (right panel) consists of distinct cell layers. Grid cells are most abundant in layer II (LII). Adapted from Ramsden et al. (2015).

into intermediate and main classes based on morphology and firing pattern (Canto et al., 2008; Canto and Witter, 2012; Fuchs et al., 2016), and principal cell to principal cell connectivity is sparse (Dhillon and Jones, 2000; Fuchs et al., 2016).

Network models and *in vitro* recordings have proposed that principal cells in MEC interconnect via inhibitory interneurons (Couey et al., 2013; Pastoll et al., 2013; Fuchs et al., 2016). This indicates that they are embedded in a recurrent inhibitory network driven by synchronous activity by excitatory principal cells. Based on their firing patterns, the two subsets of inhibitory interneurons in the MEC layer II are the fast spiking (FS) and the low-threshold spiking (LTS) inhibitory interneurons (Gonzalez-Sulser et al., 2014; Fuchs et al., 2016). Neurochemically, MEC interneurons divide into parvalbumin (PV) positive FS basket cells, somatostatin (SOM) positive LTS interneurons, and 5-hydroxytryptamine 3A (5-HT$_3$A) positive interneurons. The primary reciprocal connectivity between principal cells and interneurons are likely of the PV positive interneurons to stellate cells (Couey et al., 2013; Pastoll et al., 2013; Fuchs et al., 2016). However, connectivity between all three interneurons types and principal cell types has been reported (Fuchs et al., 2016). Most notably, PV positive interneuron connectivity to intermediate pyramidal cells is frequent (Fuchs et al., 2016). The PV positive interneurons are believed to be involved in oscillatory network activity (Freund and Katona, 2007; Hu et al., 2014).

To reveal the functional connectivity of this network, it is necessary to also consider external

input sources. How the local MEC network connects with distal input from the MS remains elusive.

1.3.2   Distal connectivity of the septal projection to the medial entorhinal cortex

There is a reciprocal long-range inhibitory and excitatory connectivity between the MS and the MEC (Alonso and Köhler, 1984; Fuchs et al., 2016). Selective lesioning and immunohistochemistry of the basal forebrain and the MS has evidently shown non-cholinergic neurons (Dunnett et al., 1991; Alonso and Köhler, 1984), and especially GABAergic projections to be crucial in cerebral cortex activity, including the MEC (Freund and Antal, 1988; Gritti et al., 1997). Network activity of GABAergic inhibitory interneurons are believed to be the main candidate for the MS pacemaker cells (Tóth et al., 1997). These cells fire rhythmically at theta frequency, and are found to be phase-locked to the ongoing LFP theta oscillations (Varga et al., 2008; Hangya et al., 2009). The specific contribution of MS excitatory and inhibitory neurons to the MEC remains unanswered, along with how the projection innervates postsynaptic cells in the MEC.

Anterograde viral tracing of the MS reveals dense expression in MEC layer II and V (Gonzalez-Sulser et al., 2014). Targeting the GABAergic projection has shown that MEC layer II and IV are most heavily innervated (Alonso and Köhler, 1984; Unal et al., 2015). Based on patch-clamp recording and viral tracing in mice, the GABAergic projection is found to innervate different types of MEC interneurons, and in particular FS PV positive interneurons are strongly inhibited by this projection, while GABAergic input to principal cells is very small. No direct connectivity is found to stellate cells, and is seldom observed for pyramidal cells (Gonzalez-Sulser et al., 2014; Unal et al., 2015; Fuchs et al., 2016). The glutamatergic projection is found to innervate principal cells to some extent, and most notably a small fraction of non-stellate principal cells (Gonzalez-Sulser et al., 2014). Whereas, the glutamatergic projection negligibly innervates interneurons (Gonzalez-Sulser et al., 2014). Quantitative analyses of the MS-MEC projection has been performed by patch-clamp recordings of the mouse brain (Gonzalez-Sulser et al., 2014; Fuchs et al., 2016). However, quantitative neurochemical analyses and investigations of the rat brain are lacking.

How the MS input affect postsynaptic responses in the MEC, and especially the firing pattern of grid cells is highly questioned. *In vitro* manipulations of the MS projection at theta frequency is found to specifically inhibit interneurons (Gonzalez-Sulser et al., 2014; Fuchs et al., 2016). How this relates to neural processing in the *in vivo* animal remains elusive.

1.4   Tracing neuroanatomical connections

Early structural analysis of the nervous system referring to the function of specific areas relates to brain lesions and functional deficits in the lifetime of experimental animals, such as lesioning the MS (Petsche et al., 1962; Mitchell et al., 1982). Thus causing grave brain damage,

these studies formed the foundation of the current understanding of brain anatomy (Purves et al., 2012). A development of techniques to trace neural connections has enabled detailed neuroanatomy of defined neural networks, whether tracing neural connections anterogradely from source to termination, or retrogradely form termination to source (Purves et al., 2012). Physical brain injections of visual molecules, such as radioactively labelled amino acids or fluorescent molecules, can be taken up by the cell body or terminal, and transported along the cell (Purves et al., 2012). These molecules label the entire cell from dendrites to axons (Purves et al., 2012). A common tracing technique is using biotinylated dextran amines combined with anterograde or retrograde tracers and immunofluorescence (Reiner et al., 2000). However, the method has a tendency to retrogradely label cells from structures not intended to target (Reiner et al., 2000). More recent combinations of neuroanatomical methods and molecular genetics has enabled the visualisation of tracer molecules under control of genetic regulatory sequences in neurons (Purves et al., 2012). This allows for molecular distinction of nerve cells and, in combination with immunohistochemistry, reveal cells expressing specific proteins in certain regions of nerve cells (Purves et al., 2012). The gene can be introduced with viral vector transduction and expressed under a specific promoter.

1.4.1 Viral vector transduction

Adeno-associated virus (AAV, fig. 1.3) has become a widely used tool in neuroscience for expression of genes of interest in cells. The virus induces low immunogenicity, no cytotoxicity, and is non-pathogenic. A vector is typically a single-stranded DNA transgene expression cassette, flanked by inverted terminal repeats (ITRs). The wild type gene and the viral sequence is recombined (rAAV) with a promoter of choice and the transgene of interest (Aschauer et al., 2013).

The vector may also contain a sense transgene, with lox sequences placed in opposite directions on both sides of the gene. Added Cre recombinase (Cre) recognises the lox sites and flips the DNA into the antisense direction, enabling transcription. Variations in lox sites has enabled irreversible Cre-lox recombination. The double-floxed inverse open reading frame (DIO) system exploits a recombination between two pairs of lox sites; loxP and lox2272. The Cre is expressed in a rAAV vector and flips the coding sequence with respect to the promoter. The remaining pair of lox sites are one loxP and one lox2272 on each side of the coding sequence, hence are no longer recognised by Cre (Saunders et al., 2012). For specific targeting of neurons Cre can be expressed virally under a specific promoter (Soudais et al., 2001), or in genetically modified animals expressing Cre in specific cell types.

To circumvent the labelling of entire cells, the synaptophysin-mCherry construct is a beneficial tool for anterograde neuronal tracing of presynaptic terminals. Synaptophysin is a synaptic vesicle protein, present in all neurons, expressed in the cell soma and transported along the axons to the axon terminals (Calhoun et al., 1996), and mCherry is a red fluorescent marker protein. The genes for synaptophysin and mCherry can be inserted in an AAV
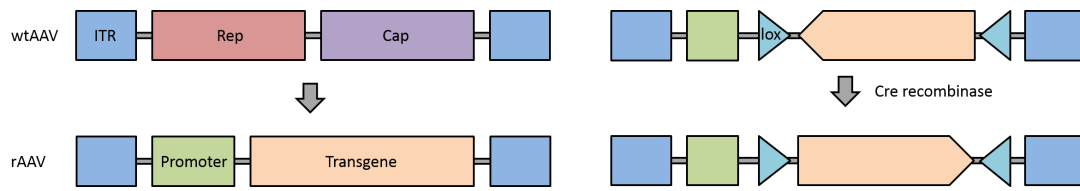
Figure 1.3: The AAV vector is a transgene expression cassette. The wild type gene (left: wtAAV) contains the rep and cap genes, for replication and protein capsule, and is flanked by ITRs. The recombinant (rAAV) vector is removed of rep and cap, in exchange of a promoter and the transgene. The cassette can be recombined with a transgene in the sense directions (right) with lox sites on both sides. Cre recombinase recognises the lox sites and flips the DNA to antisense.

DIO vector and co-expressed with an AAV construct containing genes for Cre. To enhance specificity, immunohistochemistry of vesicular transporters can identify whether the neurons are for example glutamatergic or GABAergic.

1.4.2   Staining for vesicular transporters

The major means by which neurons communicate in the nervous system is through chemical transmission at the synapse. The pre-and postsynaptic events form the basis for plasticity and learning in the central nervous system (CNS). Chemical transmission involves synthesis, storage and release of neurotransmitters at the presynaptic terminal, and the presence of specific receptors at the postsynaptic membrane. The main excitatory neurotransmitter in the brain is glutamate, whereas, the main inhibitory neurotransmitter is GABA. Vesicular transporters are involved in the uptake of neurotransmitters from cytosol to synaptic vesicles. They work as antiporters, exchanging hydrogen ions with neurotransmitters (Siegel et al., 1999). There are three isoforms of vesicular glutamate transporters (VGLUT). VGLUT1 is mainly expressed in the hippocampus and the cortex. VGLUT2 is mainly expressed in lower brain stem regions, hypothalamus, thalamus, striatum and pons (Boulland et al., 2004). VGLUT3 is found to be present in nonglutamatergic neurons, possibly functioning in cotransmitter release (Gras et al., 2008). The vesicular GABA transporter (VGAT) is expressed in GABAergic neurons throughout the brain (Chaudhry et al., 1998). Staining synaptic terminals for vesicular transporters is a highly advantageous and very specific method for characterising presynaptic terminals into inhibitory and excitatory varieties (Zinchuk and Grossenbacher-Zinchuk, 2009).

1.5   Functional analysis of neural networks

To investigate the organisation of neural networks, functional analyses provides the ability to study electrical activity in neurons. One particularly useful method is electrophysiological recordings of single units and the LFP with microelectrodes in neural tissue. This method can be combined with manipulations of neural tissue, such as using pharmacology or electrical

stimulations (Purves et al., 2012). Pharmacological manipulations provide low temporal resolution, and electrical stimulations cannot distinguish cell types and are therefore lacking target specificity. The state of the art technique providing both target specificity and high temporal control is optogenetics, which is readily integrated with electrophysiological recordings.

1.5.1   Optogenetics

Optogenetics is today a commonly used technique for investigating neural circuits (Boyden et al., 2005), integrating optics and genetics. The advantage of using microbial opsin genes is remarkable for millisecond control of action potentials in distinct neuronal populations. Membrane bound ion pumps and channels, such as channelrhodopsin (ChR, fig. 1.4) and halorhodopsin (HR), transport ions in response to light. These proteins are single-component light-sensing systems, meaning that the same protein achieves light sensing and ion transport. ChR is a cation channel with a peak activation at 470 nm (blue light), inducing depolarization by cation flow down the electrochemical gradient. HR is a chloride pump with a peak activation at 590 nm (yellow-red), inducing hyperpolarization by an inward directed ion current. Many genetically modified versions of rhodopsins are constructed with distinct qualities such as switching channels to active and inactive states (Yizhar et al. 2011). One such variant is the Step-Waveform Inhibitory ChR (SwiChR), activated by a pulse of blue light and deactivated by a pulse of yellow-red light, with chloride flow in the active state (Berndt et al., 2014).
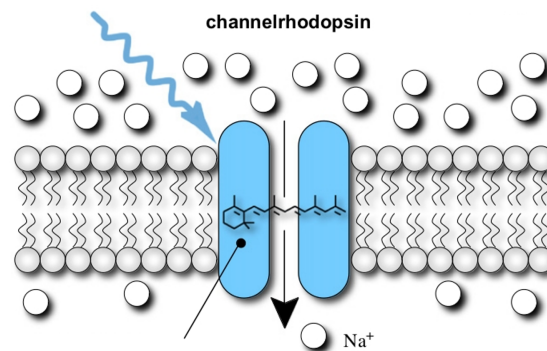
Figure 1.4: Channelrhodopsin is a cation membrane protein channel activated by blue light. This protein is used in optogenetics to specifically manipulate neural circuits. Adapted from Abilez et al. (2011).

Virally expressed rhodopsins are advantageous with the flexibility of multiplexing the protein with anatomically traceable fluorescent proteins, such as GFP. For example; ChR-GFP can be expressed in a variability of AAV vectors under specific promoters. Optogenetic projection (axonal) targeting can ensure great neural circuit specificity. By viral injection in the region containing cell bodies, following implantation of an optic fibre into the area containing neuronal processes, light delivery here will control the specific projection, not biased by pro-

cesses reaching other brain areas. Projection termination labelling is even more specific, by injecting a DIO-virus into the region containing cell bodies, and a Cre-expressing virus in the target areas together with an optic fibre implant. This will ensure manipulation of projections terminating in the target area, excluding processes passing through (Yizhar et al., 2011).

The combined optogenetic-electrophysiology strategy profoundly advances the study of functional properties of postsynaptic MEC neurons targeted by the MS projection. By selectively expressing ChR in the MS projection with a rAAV virus, and electrophysiologically recording single units and LFP in the MEC, functional properties can be investigated with minimal temporal latency to photostimulation. The MS projection can be photoactivated with light in the theta frequency range, and the light can even be controlled to only be activated within or outside the the grid fields of grid cells. This enables a highly precise method for studying functional properties of the MS-MEC projection.

1.6 Aims

The main aim of this study was to investigate the role of the MS projection for different cell types in the MEC. This was constricted to identify the contribution of MS inhibitory and excitatory projections to the MEC, map out the postsynaptic targets of the MS projection in the MEC, and to functionally investigate how perturbations of the MS projection affect cell types in the MEC.

Based on previous studies stating that the MS GABAergic projection primarily targets inhibitory MEC interneurons (Gonzalez-Sulser et al., 2014; Fuchs et al., 2016), and that principal MEC neurons are interconnected via inhibitory interneurons (Couey et al., 2013; Pastoll et al., 2013; Fuchs et al., 2016), one would expect the distal MS GABAergic projection to disinhibit principal MEC neurons. If the theta oscillations from direct connections between the MS and the MEC are required for grid cell spatial coding, one would expect grid cell spatial coding to be disrupted from perturbations of this projection, which has been found during inactivation of the MS (Brandon et al., 2011; Koenig et al., 2011).

To test these predictions, the following sub-goals were addressed:

1. Anatomical tracing and neurochemical analyses to identify

    (a) the inhibitory and excitatory projections from the MS to the MEC
    (b) the synaptic targets of the MS – MEC projection

2. Functionally investigate MEC single unit and LFP responses to optogenetic perturbations of the MS-MEC projection

2 Materials and methods

In order to acquire a sufficient amount of data for both neurochemical and electrophysiological mapping of the projection from medial septum (MS) to the median entorhinal cortex (MEC), all surgical procedures were performed by my supervisors Mikkel Lepperød and Marianne Fyhn, with my assistance. I prepared equipment (microdrives) and then performed electrophysiological recordings, perfusions, histology, imaging and analysis of microscopy data, as described below.

This project consisted of two parts; (1) anatomical and neurochemical analyses of the projection from MS to the MEC and (2) optogenetic and electrophysiological investigation of the projection.

2.1 Subjects

All experiments were approved by the Norwegian Food Safety Authority (Mattilsynet) and the Norwegian Animal Research Authority (FDU) ahead of the project commencement, and performed at the Department of Biosciences (IBV) at the University of Oslo, Norway. Animal treatment and housing followed regulations set by the European Union and the FDU. All participants in the experimental part of the project have completed a course in Experimental Animal Research (similar to a FELASA C certificate), approved by the Norwegian Food Safety Authority.

For this project 12 male Long Evans rats, three for anatomical studies and nine for electrophysiological recording (aged 3-6 months), were housed in polycarbonate cages (35 x 55 x 19 cm) with woodchip bedding (Scanbur A/S) – three to four animals per cage with ad libitum food access. Post-surgery animals with implants were housed individually, minimising risk of injury, in transparent Plexiglass cages (35 x 55 x 30 cm). They were kept on a food deprived schedule of 6-10 food pellets, for motivation during experimental periods. The weight of the rats was 300-500 g at surgery and recordings. All rats were maintained on a 12h light/ 12h dark cycle, and tested in the dark phase. For environmental enrichment during individual housing, animals were provided with toys, wooden logs and climbing rope.

2.2 Part I: Anatomical and neurochemical analyses

In order to investigate neurochemical properties and connectivity of septal input to neurons in the MEC, anterograde viral tracing was combined with immunohistochemistry, followed by imaging and co-localisation analysis.

2.2.1 Virus preparations

Prior to injections, viruses were prepared and loaded in a 500 nl, 33 gauge Hamilton syringe (Neuros Syringe, VWR, USA). For neurochemical tracing in the medial septum the DIO

Cre-lox system (explained in section 1.4.1) was used. A 1:1 solution of Cre recombinase inducible anterograde virus AAV8-hEF1α-DIO-synaptophysin-mCherry (Viral Gene Transfer Core, Massachusettsm USA) and the Cre recombinase (Cre) expressing anterograde virus AAV5-CMV-Cre (Penn Vector Core, Pennsylvania, USA) was mixed. Co-infection of both viruses in a given neuron results in the production of the Synaptophysin-mCherry fusion protein, which allowed for visualization of projecting synaptic terminals.

2.2.2   Surgical procedures

Equipment used for surgery was kept aseptic and sterile during the procedures. Surgery tools were heat sterilized (150ºC, 90 min), and kept in ethanol (70 %) during surgery, and Q-tips were autoclaved.

Anaesthesia and preparations

Rats were initially sedated in a chamber using 5% isoflurane (Baxter, Oslo, Norway). For virus injections rats were anaesthetized with intraperitoneal (i.p.) injection of Ketalar (ketamine, 0.75 mg/kg) and Domitor (dexmedetomidine, 0.75 mg/kg). Anaesthesia levels were controlled by testing hind paw flexes regularly during surgery. Heart rate, breathing rate, blood O_2 saturation and core temperature were monitored with an oximeter and feedback controlled heating pad (MouseStat system; Kent Scientific, USA).

Animals were placed in a stereotaxic frame during surgeries (World Precision Instruments Ltd, Hertfordshire, UK). The head was fixed to the frame by placing ear pins in external auditory meatus, and a height-adjustable nose-clam was regulated to ensure that the midline of the skull was aligned with the frame. Stereotaxic coordinates were followed in accordance with the Paxinos and Watson (2007) rat brain atlas.

Hair was removed from the surgical area using an electric shaver. The area was cleaned with a 70% ethanol, chlorhexidine and iodine solution. Eyes were protected from drying by applying ViscoTears (Thea Laboratories, Oslo, Norway). A longitudinal incision from between the eyes to the back of the skull was made using a scalpel. Periosteum was moved aside with q-tips and kept away using artery clamps. Excessive blood and remaining periosteum were removed using Q-tips. The bone structures bregma, lambda, and the midline, in addition to the sinus vein were used as landmarks to identify coordinates for MS and MEC. The skull and exposed cortex was kept moist using sterile 0.9% saline solution during the procedure.

Virus injections

For virus injections (fig. 2.3), a single hole was drilled using a hand held dental drill (Perfecta-300, WandH Nordic, Sweden) with a polishing drillbit (Dental Burs, USA), above the MS (for coordinates see table 1). The Hamilton syringe was attached to the stereotaxic frame and lowered to 0.1 mm below target depth, to prevent tissue damage, followed by injection at

Table 1: Coordinates for injections in accordance with Paxinos and Watson (2007); anterioposterior (AP) relative to bregma (B) and mediolateral (ML) relative to the midline, and dorsoventral (DV) relative to bregma.

Virus	Injection coorinates			
	AP	ML	DV	Dose (µl)
1:1 rAAV8-hEF1a-DIO-synaptophysin-mCherry and rAAV5-CMV-Cre	B0.6	0	7.3/6.8	0.4/0.4

target depths beginning with the most ventral injection. The dose injection rate was 0.05-0.08 µl/min, followed by a pause of 5-10 minutes before retraction. After injections the wound was cleaned with sterile 0.9 % NaCl and sutured shut.

2.2.3   Post-operative care

Following surgery, the animals were administered subcutaneous (s.c.) injections of Rimadyl (carprofen 5 mg/kg, 1 dose/day) for postoperative analgesia every 24 hours for three days, and the local anaesthetic Xylocain applied to wound edges. In the case of suspected infections, the wound edges were cleaned with saline solution and 70% ethanol. Animals were then left for six weeks before perfusion to secure sufficient expression of the mCherry Synaptophysin fusion protein. Animals were weekly checked for infections.

2.2.4   Histology

Perfusion and brain sectioning

To preserve the brains for histological investigation, rats were deeply anaesthetised with 5% Isoflurane gas and an i.p. overdose of Pentobarbital sodium (52.5 mg/kg; 25 mg/kg), followed by transcardial perfusion with 0.9% saline solution and 4% paraformaldehyde (PFA) in phosphate buffered saline (PBS). The brains were post-fixed in 4% PFA in PBS solution for a minimum of 24 h, and soaked in 30% sucrose solution for a minimum of three days. Prior to freezing, the brains were cut into three to facilitate convenient sampling and identification of the MS and the two hemispheres of MEC; the frontal part was first cut off to allow for coronal sampling from the MS, then the remaining part was cut along the midline to allow for sampling in the sagittal plane of the MEC. The brains were then flash-frozen and mounted in a cryostat (CM1950, Leica Biosystems) holding -19 °C. Sections of 40 µm thickness were made from the MS injection site and from the MEC, and placed directly in 0.01 M PBS containing 0.02% sodium azide.

Staining for Cre recombinase

To determine the viral injection site and viral expression of the synaptophysin-mCherry conjugate, coronal MS sections were stained for Cre. Sections were washed (3x5 min) in 0.1 M

PBS and left for 1 h in blocking solution (1% BSA and 0.02% Triton 100-X in 0.1 M PBS) before incubation in primary antibody solution (1:500 mouse anti-Cre in blocking solution) over night. Sections were washed (3x5 min) in 0.1 M PBS and incubated in secondary antibody (1:400 Alexa Fluor® 594 donkey anti-mouse in blocking solution) for 1 h. Sections were washed (3x5 min) in 0.01 M PBS, mounted on glass slides and left to dry for 30 min. Slides were dipped (3 x) in dH_2O to remove excess salts, and cover slipped using FluorSave. The staining protocol was performed at room temperature, on a shaker with constant agitation.

Co-staining for mCherry and VGLUT1, VGLUT2 or VGAT

For neurochemical mapping of MS input to the MEC, sections were co-stained for the synaptophysin-mCherry fusion protein and vesicular glutamate transporters (VGLUT1 and 2) or vesicular GABA transporter (VGAT), to elucidate whether the inputs were inhibitory (VGAT) or excitatory (VGLUT 1 and 2). Sections were washed (3x5 min) in 0.1 M PBS and left for 1 h in blocking solution (1% BSA and 0.02% Triton 100-X in 0.1 M PBS) before incubation in primary antibody solution (1:20 000 chicken anti-mCherry and 1:5000 rabbit anti-VGLUT1/VGLUT2/VGAT in blocking solution) over night. Sections were washed (3x5 min) in 0.1 M PBS and incubated in secondary antibody (1:200 Alexa Fluor® 594 goat anti-chicken secondary antibody and Alexa Fluor® 488 goat anti-rabbit in blocking solution) for 1 h. Sections were washed (3x5 min) in 0.01 M PBS, mounted on glass slides and left to dry for 30 min. Slides were dipped (3 x) in dH_2O to remove excess salts, and cover slipped using FluorSave. The staining protocol was performed at room temperature, on a shaker with constant agitation.

Co-staining for mCherry, cellular markers and DAPI

For neurochemical mapping of MS input to postsynaptic cells in the MEC, sections were stained for the synaptophysin-mCherry fusion protein and cellular markers for cell types in the MEC. Pyramidal cells were identified by staining for calbindin (CB), parvalbumin (PV) positive interneurons by staining for PV, and stellate cells by staining for reelin (RE). All slides were cover slipped with 4',6-diamidino-2-phenylindole (DAPI) Fluoromount to visualize cell nuclei.

Calbindin, Parvalbumin and Reelin.   Sections were washed (3x5 min) in 0.1 M PBS and left for 1 h in blocking solution (1% BSA and 0.02% Triton 100-X in 0.1 M PBS) before incubation in primary antibody solution (1:20 000 chicken anti-mCherry and antibody for respective marker (table 2) in blocking solution) over night. Sections were washed (3x5 min) in 0.1 M PBS, and incubated in secondary antibody (1:200 goat anti-chicken Alexa Fluor® 488 and antibody for respective marker (table 2) in blocking solution) for 2 h. Sections were washed (3x5 min) in 0.01 M PBS and mounted on glass slides. The staining protocol was performed at room temperature, on a shaker with constant agitation.

Table 2: Antibodies and concentrations used for marking cells positive for calbindin (CB), parvalbumin (PV) and reelin (RE) in the medial entorhinal cortex.

Staining	Primary antibody	Concentration	Secondary antibody	Concentration
CB	rabbit anti-CB D-28k	1:1000	goat anti-rabbit	1:5000
PV	goat anti-PV	1:1000	donkey anti-goat	1:1000
RE	mouse anti-RE	1:1000	donkey anti-mouse	1:1000

2.2.5   Data analysis

Microscopy and imaging

For co-localisation analysis confocal images were obtained using a Leica TCS SP8 inverted scanning confocal microscope (Leica Microsystems, Germany). To visualize the dyes: three two optically pumped semiconductor lasers (OPSLs) were applied, respectively for each dye. Laser emission spectra were adjusted to suit the spectral borders of each dye. The OPSL 552 nm laser was not optimal for the Alexa Fluor® 594 dye, and was adjusted for by increasing the laser intensity. The detectors used were a photomultiplier (PMT) for the green and blue channels (gain 800V) and a hybrid detector (HyD) for the red channel (gain 100%). Collections of Z-axial stacks (2048x2048 pixels) were sampled at 0.33 μm intervals. The zoom was set to 0.75 and the objective of choice was a 63x/1.3 N/A used with glycerol. To minimize pixel saturation and background signal, laser intensities and offset levels were adjusted for each stack. To reduce noise, each pixel was averaged 3 times. Imaging was performed shortly after immunolabeling and sections were kept dark and cold (~4°C) between sessions, to minimize loss of signal.

Co-localisation analysis

The software package Imaris (version 8.1.3, Bitplane AG, Switzerland) was used to semi-automatically analyse the images for co-localisation between the mCherry-synaptophysin fusion protein and presynaptic and postsynaptic markers. Example photos were prepared with ImageJ (NIH). 3D images were conducted from Z-axial stacks of 2D images. Three dorsoventral (DV) sites from MEC layer II (LII) and III (LIII) (fig. 2.1) and one site from the each layer in the opposite hemisphere were analysed as mean of all synaptic puncta.

Punctum-to-punctum analysis.   Punctum-to-punctum analysis was conducted to quantify co-localisation of mCherry with VGAT, VGLUT1 or VGLUT2. The co-localisation of two synaptic puncta was obtained using the spot detection algorithm in Imaris. A region of interest (ROI) was set around the synaptic puncta for each marker to quantify percentage of co-localisation between two synaptic puncta types. To adjust for background noise and false positives, the smallest diameter of objects to be detected was set to 1 μm with background subtraction. An intensity threshold (spot quality) was set for the different markers to be in-
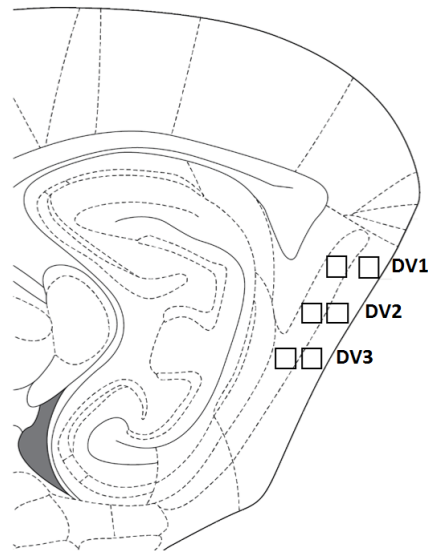
Figure 2.1: Positions from where Z-axial images was acquired from layer II and III and three dorsoventral depths (DV1-3) in the medial entorhinal cortex for all markers except calbindin, from which layer 3 was excluded. Adapted from Paxinos and Watson. (2007).

cluded in the analysis based on manual inspection in 3D space. The threshold (6, 3.5, 5, and 5 for mCherry, vGAT, vGLUT1 and vGLUT2, respectively) was then applied to all image stacks of the respective marker to set a standard during analysis. A lower limit of 50% of occupancy between two puncta was set to be scored as co-localised. To determine the percentage of the MS terminals containing the respective vesicular transporter, data was quantified as percentage of mCherry spots co-localising with VGAT, VGLUT1 or VGLUT2 spots (Hoon et al., 2017).

Punctum-to-cell analysis.   Punctum-to-cell analysis was conducted to quantify co-localisation of mCherry with markers for PV or CB. The co-localisation of synaptic puncta with labelled cells was analysed with the ImarisCell module, enabling the user to make 3D models of cells and localising synaptic puncta onto cells. Adjustments and thresholding for mCherry was performed as described for analysis of synaptic co-localisation. Prior to co-localisation analysis, the detected cell bodies were manually inspected. Several detected cells were discarded from analysis due to high background staining or axons covering large part of the image. To be able to distinguish individual cells the 3D models included to the degree possible solely cell soma, nucleus, and puncta. Additionally, the total number of red puncta in the image was quantified. To limit false positive cells, cells smaller that 100 μm^3 were excluded from the data set.

Statistical analysis

Statistical analysis was performed with GraphPad Prism version 7.02 for Windows (GraphPad Software, USA).

Firstly, the data sets were run through a Shapiro-Wilk normality test (95% confidence interval), to test whether they were normally distributed. As only the data for VGAT passed the normality test, the data was presented in box and whiskers plots (10-90% min-max) to better show the variations in the data sets. Hence, statistical tests were based on the median rather than the mean. To test whether the medians varied significantly, the data was run through a Kruskal-Wallis test. To further analyse the specific sample pairs a Dunn's test was run *post hoc.* Statistical significance was defined as $p < 0.05$.

2.3   Part II: Optogenetics and electrophysiology

In order to investigate how the septal input affects activity of neurons in the MEC, we combined the use of optogenetic manipulations of the septal projection, and at the same time record neural activity in the MEC. To achieve this, the rat was initially injected with a viral vector carrying the optogenetic construct in the medial septum, and implanted with optic fibre in the medial septum and optic fibre and tetrodes in the MEC. Optogenetic manipulations and electrophysiological recordings were conducted as the rat moved freely within the recording arena.

2.3.1   Virus preparations

Prior to surgeries with viral injections viruses were prepared as described in section 1.4.1. For optogenetic excitation the viruses AAV5-hSyn-hChR2(H134R)-EYFP (UNC Vector Core, NC, USA) or AAV8-hsyn-eChR2(H134R)-EYFP was used for injections in the MS. For optogenetic inhibition the Cre recombinase (Cre) inducible anterograde virus AAV8-EF1a-DIO SwiChR++-eYFP was used for injections in the MS, and the Cre was expressed retrogradely with CAV-2 virus (Soudais et al., 2001) injections in the MEC (viruses were gifts from Karl Deisseroth lab, Stanford university, USA).

2.3.2   Optetrode and microdrive construction

Tetrodes were constructed from twisted 17 µm heavy polyamide insulated platinum-iridium wire (90%/10%) (California Fine Wire Company, USA). Both ends of a 20-30 cm wire were assembled, and fastened on a cross shaped metal arm, creating two loops. A hook with a magnet was placed through the loops, and the wire twisted by placing a magnetic stirrer underneath. A heat gun was used to fuse the twisted wire. The tetrode was cut, leaving one long end entangled and the other end into four loose ends. Insulation was burnt off from the tip of the loose ends. Four tetrodes were inserted through a cannula attached on a microdrive (Axona Ltd, Herts, UK), with a larger cannula partly loose on the outside. The loose ends were wired to the free end cables on the microdrive, and attached with conductive silver paint (HK Wentworth, Leicestershire, UK) and covered with nail polish. Electrode tips were electroplated with platinum solution to reduce impedances to <150 kΩ at 1 kHz (Ferguson et al., 2009).

For the optetrode (fig. 2.2) (Anikeeva et al., 2012), an optic fibre ferrule (2.5 mm diameter stainless ferrule, 200 μm diameter core, 0.39 N/A, Thorlabs, USA) was added to the assembly such that the optic fibre shared the inside of the inner cannula with the tetrodes, and beforehand cut with a diamond cutter to protrude 8 mm outside the outer cannula. The ferrule was attached with dental cement to the microdrive. Tetrodes were cut to protrude 0.5 mm beyond the end of the fibre optic shaft, and electroplated.
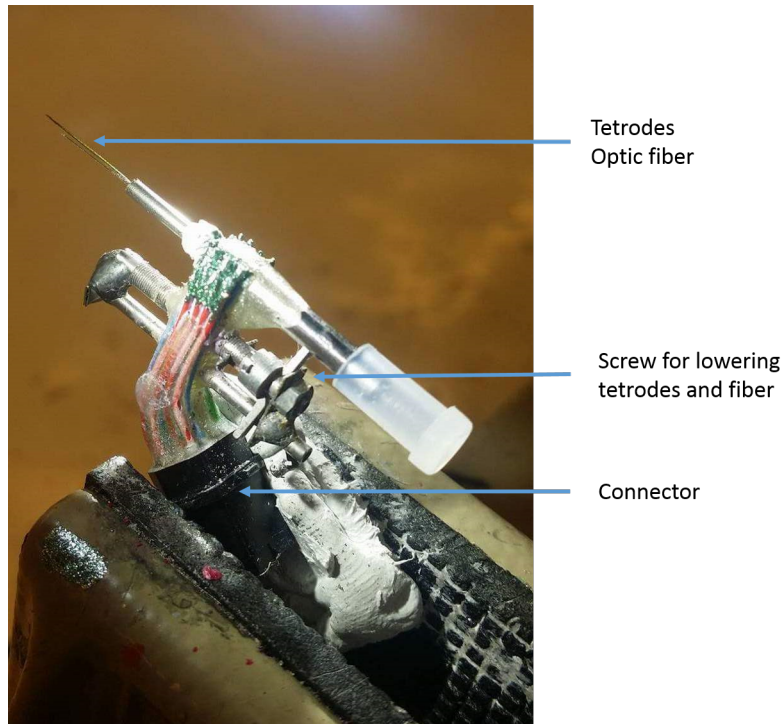
Figure 2.2: Optetrode assembled with 4 tetrodes inserted through cannulas attached on a microdrive (Axona Ltd, Herts, UK), during recordings the microdrive was connected to AC-coupled unity-gain operational amplifiers.

2.3.3   Surgical procedures

Anaesthesia and preparations

Surgical preparations were performed as described in section 2.2.2 with some modifications. For optetrode and optic fibre implantations rats were anaesthetised with a constant flow of a mix of Isoflurane and air (2 L/min; 1-2.5 %) during surgery. The shift in protocol was to allow for a longer surgery, faster recovery and to avoid ketamine's negative effect on heart muscle during long procedures.

Virus injections

Virus injections were conducted as described in section 2.2.2, additionally to virus injections in the MEC for optogenetic inhibition (see table 3).

Table 3: Coordinates for injections in accordance with Paxinos and Watson. (2007); anterio-posterior (AP) relative to bregma (B) or sinus (S), mediolateral (ML) relative to the midline, and dorsoventral (DV) relative to bregma.

Virus	Injection coordinates			
	AP	ML	DV	Dose (µl)
rAAV5-hSyn-hChR2(H134R)-EYFP	B0.6	0	7.3/6.8	0.4/0.4
rAAV8-EF1a-DIO SwiChR++-eYFP	B0.6	0	7.3/6.8	0.6/0.6
CAV-2 Cre	S0.5	4.5	3.3/2.5	0.736/0.736
rAAV8-hsyn-eChR2(H134R)-EYFP	B0.6	0	7.3/6.8	0.4/0.4

Optetrode and optic fiber implantation

Microdrives with optetrodes were implanted bilaterally in both hemispheres of the dorsocaudal MEC, and an optic fibre was implanted in the MS (fig. 2.3). Four jewellers' screws were attached anterior of bregma, two as grounding electrodes, two for anchoring. Two screws were attached lateral to the midline and three posterior of lambda for further stabilization and anchoring of the implant to the skull. Holes for the screws were drilled with an OmniDrill 35 (World Precision Instruments Ltd, UK) attached to the stereotaxic apparatus.

Craniectomies were performed bilaterally for implants in the MEC and one for implant in the MS using a hand-held Perfecta-300 dental drill (W & H Nordic, Täby, Sweden). Implants were attached to the stereotaxic frame, dura mater removed from the exposed areas of the brain, and implants lowered into position according to coordinates in table A.1. The coordinates were slightly varied to avoid blood vessels and to accommodate for the varying size of the animals. The outer cannula surrounding the inner cannula on the microdrive was lowered to rest on top of dura mater. One screw per microdrive was joined with a wire and soldered to the grounding wire of the microdrive.

Following implantations holes exposing cortex were filled with Spongostan (Ethicon, Norderstedt, Germany) and saline solution. To anchor the implants and cover up the exposed skull a thick layer (0.5-1 cm) of dental cement was applied to the entire open area of the skull, and ensured covering of anchoring screws. The first layer of cement was mixed to low viscosity, ensuring even spread and strongly attached implants.

2.3.4   Post-operative care

Post-operative care was performed as described in section 2.2.3. To allow the animals to recover from the implant surgery, experimental procedures were not conducted before a resting period of minimum three days.
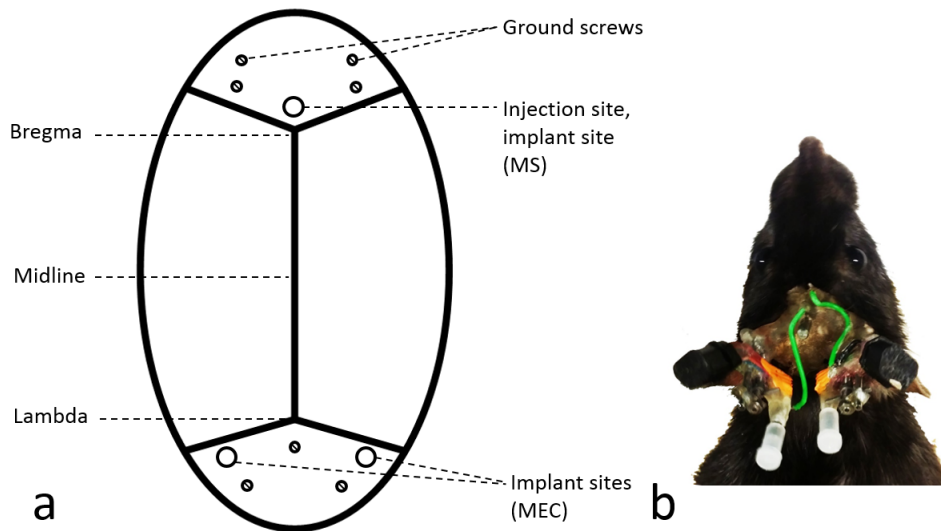
Figure 2.3: (a) Overview of the exposed scull and craniectomies. The figure shows injection and implant sites for the medial septum (MS) and the medial entorhinal cortex (MEC). Three screws were attached anterior of bregma, two ground screws, and one anchoring screw. Four screws were attached posterior of lambda for further anchoring. (b)Rat #1685 with optetrode microdrives implanted in both MEC hemispheres and one optic fibre implanted in the MS. Ground wires (green) were coupled to the ground screws attached to the skull anterior of the MS fibre implant.

2.3.5   Electrophysiology and optogenetics

Recording conditions

All electrophysiological recordings and optogenetic stimulations were performed in awake, freely moving rats (fig.2.4). Rats were trained to run continuously in the recording area motivated by small pieces of chocolate cereal scattered individually into the area (1 x 1 x 0.5 m) of black metal walls and laminate floor. Training was performed pre-surgically and between virus and implant surgery. To polarize the box, a white que card (20 x 30 cm) was placed in the centre of one of the walls. The surroundings were dark during experiments. The box was kept in a constant location, and the rat rested in its home cage between trials. In order to extinguish odours and excrements the floor was cleaned with soap and water between trial series.

Electrophysiological recording setup

Single unit activity and animal's position were sampled with the recording system dacq USB (Axona Ltd, Herts, UK). The rat was connected to the equipment through AC-coupled unity-gain operational amplifiers attached to the microdrives (fig. 2.2) and coupled via a counterbalanced cable, giving the animals ability to move freely within the recording area. The optetrodes were advanced in 50 µm steps hourly with a maximum of 200 µm per day until
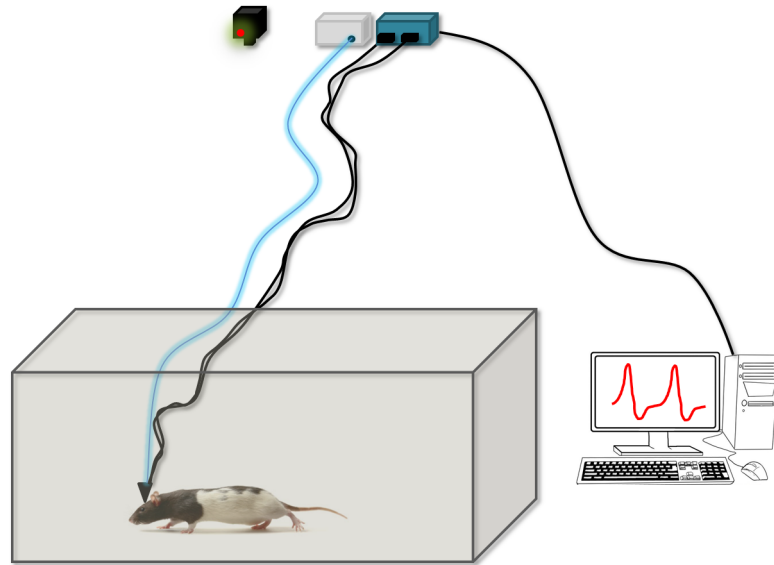
Figure 2.4: Electrophysiological recordings and optogenetic stimulations were performed in awake, freely moving rats. The rats explored a square space while searching for chocolate crumbles. Microdrives were attached to cables connected to the recording system. A fibre optic cable was attached to the optic fibre implant, delivering light from a laser box. A video camera attached to the ceiling recorded the animal path through tracking the movement of a LED diode attached to the head stage of the rat.

low-frequency, large amplitude local field potential (LFP) oscillations in the theta range (4-12 Hz) were observed. Theta activity is a characteristic feature recorded in several brain regions, including the entorhinal area during active exploration. Single unit activity was recorded from 4 tetrodes and LFP from 2-3 tetrodes, form both MEC hemispheres. One recording session lasted for 5-25 minutes depending on the optogenetic stimulation protocol and behaviour of the animal.

Single unit recording signals were amplified 6 000 to 15 000 times. They were low- and high-pass filtered between 0.8 and 6.7 kHz. For noise reduction, each channel was recorded relative to a reference – a channel with low-amplitude activity. Spikes were stored to disk at 48 kHz (50 samples/waveform, 8 bits/sample), and with a 32 bit time stamp (clock rate at 96 kHz). The LFP signals were amplified 1500 to 3000 times, band-pass filtered at 500 Hz and stored to disk at 4.8 kHz (16 bits/sample). Real-time position, running path and head direction were monitored using two light emitting diodes (LEDs) on the head stage of the animal by an overhead video camera. Signals were digitized by the data acquisition system DacqUSB (Axona Ltd).

Optogenetic activation

Neural activation was manipulated by activating Channelrhodopsin (ChR), by blue light stimulation. Light pulses were delivered by an optic patch cable (200 μm core diameter, 220 μm cladding, 900 μm jacket, N/A: 0.37, SMA connector with 2.5 mm metal ferrule, Doric lenses, Canada) coupled to a laser emitting light of 473 nm wavelegth (Shanghai Lasers & Optics co. Ltd., China). The output connector on the fibre port was attached to a connector on the implanted optic fibre. To account for variable light output, light intensity was calibrated at the tip of the fibre for every third trial and set to an average of 8-30 mW using an optical power meter (Thorlabs, USA). Stimulations were controlled by the pulse train generator Pulse Pal (open ephys).

During one experimental session (fig. 2.5) light pulses were delivered to one of the optic fibre implants. Neural activity was recorded from both MEC hemispheres before, during and after light stimulation. The optical stimulation varied systematically to determine optimal stimulation parameters. 5 ms light pulses were delivered at 11 Hz for 60 seconds. A session would include an initial baseline (1-15 min), a stimulation sequence (1-6 x) and a final baseline (0-5 min). Chance of after-discharge and tissue damage was taken into consideration, giving 1-2-minutes minimum intervals between trials in the stimulation sequence.

An additional programmed pulse train generator software (Open Ephys) was developed by M. Lepperød and Alessio Buccino. The program enabled the experimenter activate the laser inside and outside grid fields, by drawing circular fields in the recording arena. During a recording the rats position was tracked and the laser was activated when the rat moved inside the drawn fields. One session included a baseline recording (5-15 min). From this recording, laser fields were drawn according to the grid fields of one cell. In the following recording the optical stimulations were conducted inside these fields. In a third recording, the laser fields drawn outside the grid fields.

Optogenetic inhibition

Neural inhibition was controlled by a switchable Step-Waveform Inhibitory Channelrhodopsin (SwiChR), which is activated by a pulse of blue light stimulation, remains open in the dark and gets deactivated by red light stimulation. The protocol (fig. 2.5c) for optogenetic inhibition varied from activation by means of an extra yellow-red laser of wavelength 593 nm (Shanghai Dream Lasers Technology Co., Ltd., China) coupled with a rotary joint combining the two laser sources into one optic fibre. One 1 s blue light pulse was delivered followed by a dark phase of 60 s and a final 1 s red light pulse.

2.3.6   Histology

Perfusion and brain sectioning

Perfusion and brain sectioning was conducted as described in section 2.2.4.
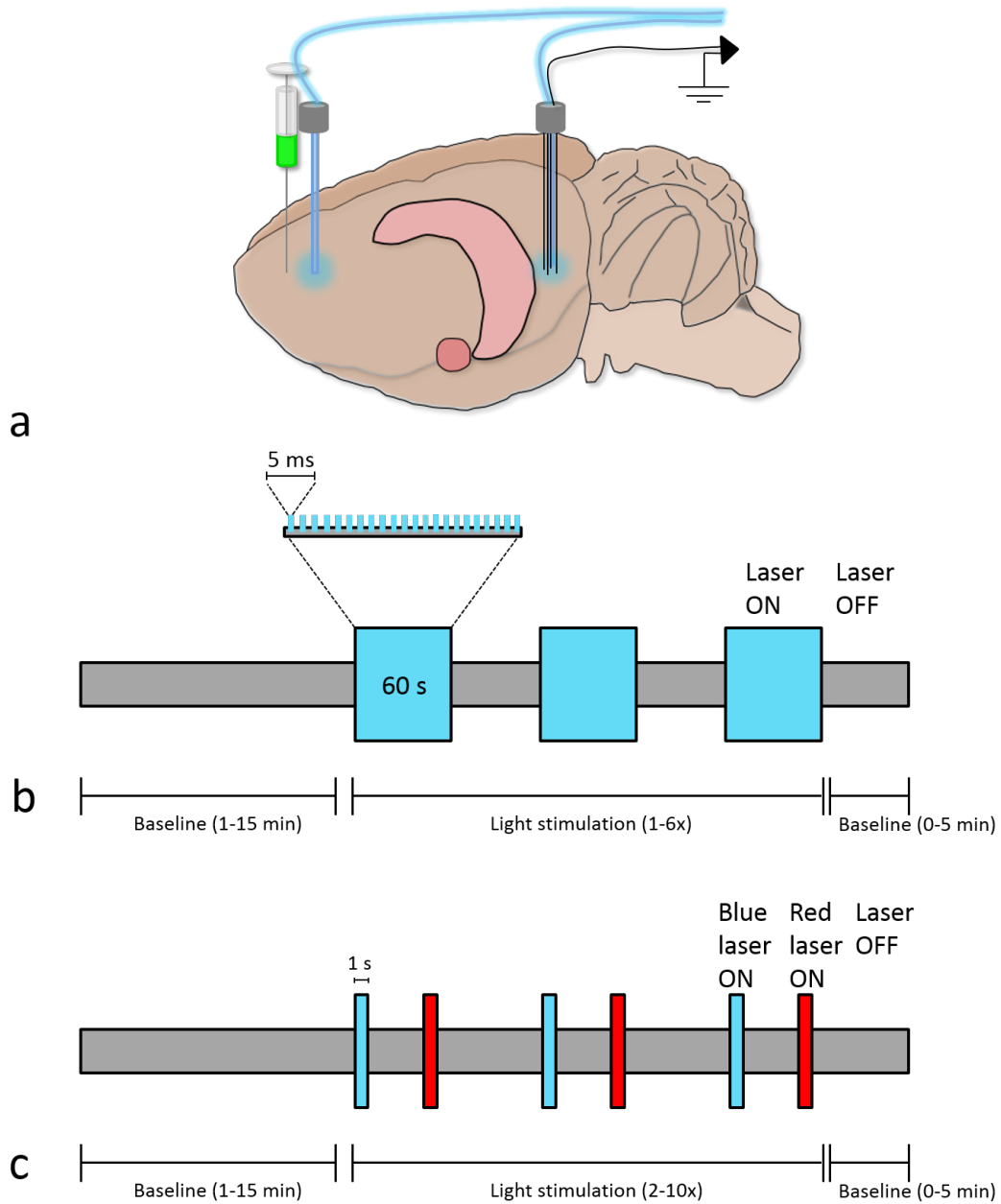
Figure 2.5: (a) Schematic drawing of viral administration of ChR-EYFP in the medial septum (MS), followed by MS fibre optic implant, and medial entorhinal cortical optetrode implants in both hemispheres. (b, c) Experimental setups for optogenetics. A session included an initial baseline, a stimulation sequence, and a final baseline. (b) Optogenetic activation. 5 ms light pulses were delivered at 11 Hz for 60 seconds. (c) Optogenetic inhibition. 1 s blue light pulse was followed by a 60 s dark phase and a final 1 s red light stimulation.

Nissl staining with Cresyl violet

In order to locate position of the implanted tetrodes and optic fibre and examine potential tissue damage, brain sections (40 μm) containing traces from the implants were stained with Cresyl violet, for Nissl bodies – that are granules of rough endoplasmic reticulum with rosettes of free ribosomes. Sections were mounted onto SuperfrostPlus glass slides (Thermo Fisher Scientific, Norway), dried, and treated with 100% ethanol-chloroform (1:1) overnight in order to fixate sections to the slide. The sections were then gradually hydrated in ethanol and finally water, followed by immersion in Cresyl violet staining solution, and gradually dehydrated in ethanol followed by xylene. Glass slides were cover slipped using Entellan (Merck, Germany) and left to dry under fume hood overnight. When measuring implant position tissue shrinkage (∼20%) was accounted for.

Staining for GFP

To visualize spread of virus in animals used for optogenetics, sections were stained with GFP antibodies. Sections were washed (3x5 min) in 0.1 M PBS and left for 1 h in blocking solution (1% BSA and 0.02% Triton 100-X in 0.1 M PBS) before incubation in primary antibody solution (1:2000 chicken anti-GFP in blocking solution) over night. Sections were washed (3x5 min) in 0.1 M PBS and incubated in secondary antibody (1:400 Alexa Fluor® 488 goat anti-chicken in blocking solution) for 1 h. Sections were washed (3x5 min) in 0.01 M PBS, mounted on glass slides and left to dry for 30 min. Slides were dipped (3 x) in dH$_2$O to remove excess salts cover slipped using FluorSave™ Reagent (345789, Merck, Germany). The staining protocol was performed on top of a shaker at low speed intensity and at room temperature.

Double staining for GFP and Nissl

To increase anatomical visualization of viral spreading sections were stained for GFP bodies and Nissl bodies. The protocol described for GFP staining was extended to include incubation in red fluorescent Nissl stain (1:100 NeuroTrace® 530/615 in 0.1 M PBS) for 30 min followed by 0.1% Triton X-100 in 0.1 M PBS for 10 min, after secondary antibody staining.

2.3.7   Data analysis

Microscopy and imaging

Section images for overview of viral expression, immunohistochemistry and Nissl staining for tetrode- and optic fibre implants were acquired through an Axioplan 2 microscope (Carl Zeiss, Germany) with a 5x or 10x objective. Images were stitched together with the AxioVision software extension MosaiX (Carl Zeiss, Germany). Excitation wavelengths 546 nm and 488 nm were used. Images were processed using the Zen lite Blue software (Carl Zeiss, Germany) and Adobe Photoshop CS6.

Spike sorting

All analyses of electrophysiology data were processed by my supervisor Mikkel Lepperød. Previous work has established that spike waveform can be used to distinguish putative interneurons from excitatory neurons (Barthó et al., 2004). In the following text I refer to the narrow spiking units as inhibitory neurons and broad spiking as excitatory units. In short, semi-automated spike sorting was conducted as a method for separating single unit action potentials from the electrophysiological recordings. This method extracts the spike waveforms and groups similar shapes into different putative neurons, with the goal of determining which spike corresponds to which neuron. While a manual system is common, a semi-automated method was chosen, which is less time consuming and gives equally good results. The semi-automated spike sorting was performed using the program Open Ephys (open-source electrophysiology) or KlustaKwik (Rossant et al., 2016). Post-manual definition of neurons is required, to adjust for algorithm errors. Cells were classified as inhibitory or excitatory neurons based on waveform, amplitude and wave width.

3   Results

In order to identify the contribution of medial septum (MS) inhibitory and excitatory projections to the medial entorhinal cortex (MEC) and to map out the postsynaptic targets of the MS projection in the MEC, we first did neurochemical mapping of the MS-MEC projection and their postsynaptic targets.

Thereafter, in order to functionally investigate the role of the MS projection for cell types in the MEC, optogenetic perturbations were conducted while responses in the local field potential (LFP) and single unit activity were recorded.

3.1   Part I: Anatomical and neurochemical analyses

The neurochemical analysis was based on data from 201 542 stained terminal-like structures (n) and 559 cells (n) from three animals (N), and 3 coronal sections from the MS and 31 sagittal sections from both hemispheres of the MEC were analysed. Presynaptic cells were quantified as positive for the vesicular GABA transporter (VGAT) or the vesicular glutamate transporters (VGLUT)1 or 2. Postsynaptic cells were identified as parvalbumin (PV) or calbindin (CB) positive. Due to insufficient staining, data from one animal was excluded for analysis of VGAT, and sections from one hemisphere from two animals for PV. The reelin staining was not successful and was not included in the analysis.

The neurochemical analyses were limited to layers II (LII) and III (LIII) of MEC in order to be complementary to the electrophysiological recordings. Layers II/III are the main output layers of the MEC and have strong projections to the hippocampus. Further, spatially modulated cells such as grid cells are abundant in these cell layers. Staining for CB positive cells was restricted to pyramidal cells in LII (Ray and Brecht, 2016). When staining for CB, we observed negligible expression in LIII, hence, this layer was excluded from the analysis.

The analysis comprised qualitative analysis of viral expression, distribution of vesicular transporters and cellular markers, as well as quantitative analysis of presynaptic terminals and postsynaptic targets. Statistical tests were performed for the postsynaptic targeting. Due to the lack of data from one animal for VGAT, descriptive statistical analysis was conducted when analysing for presynaptic markers.

3.1.1   Viral expression of synaptophysin-mCherry conjugate

To identify the viral injection site of the synaptophysin-mCherry conjugate in presynaptic MS cells, coronal sections containing the MS were stained. Because the expression of the mCherry-synaptophysin fusion protein is limited to axonal terminals, sections were stained for Cre recombinase to visualise the injection area (fig. 3.1). The expression of Cre was located in the MS for all rats, confirming that the target area was successfully hit. For rat number 1686, a dense expression was observed in the MS 0.72 mm anterior of bregma. For animal number 1698, a less dense expression was observed in the MS 1.08 mm anterior of bregma, however,

some cell bodies in the dorsolateral (DL) MS were infected. For rat number 1699, a dense expression was observed in the MS 0.60 mm anterior of bregma.

Synaptophysin is a synaptic protein, which is transported from the cell body along the axon to the axon terminals. Using this as a promoter enables assessment of expression of mCherry in MS neuron terminals in the MEC. For amplification of mCherry signal, we used an antibody against mCherry and stained sagittal sections. The mCherry staining (fig. 3.2 f) showed dense expression in LII/III of MEC, compared to a low expression was observed in layer I (LI). The labelling of terminals in the MEC indicate that synaptophysin-mCherry was transported from MS cell bodies along the axons to the axon terminals. Despite the slightly off-target MS injection in rat 1698 (fig. 3.1), the mCherry expression in MEC was similar to the other rats. This might be explained by tracing studies reporting that the more lateral parts of the MS predominantly project to the more medial proportion of the entorhinal cortex (Gaykema et al., 1990).

3.1.2   Distribution of vesicular transporters

In order to determine inhibitory and excitatory contributions from the MS in the injected rats to the different MEC layers, the expression of vesicular transporters was analysed prior to quantitative analysis (fig. 3.2 a-c). This was conducted by staining sagittal MEC sections for vesicular transporters VGAT and VGLUT1/2, specific for inhibitory and excitatory neurons, respectively.

The VGAT staining showed a dense expression in MEC LII, and a less prominent expression in LIII. The VGLUT1 expression was distributed across layers, and appeared slightly weaker in LII compared to LIII. The expression levels of VGLUT2 was dense in LII and LIII, in between dark patches traversing LII horizontally. The expression level of VGLUT2 was lower in the MEC compared to the dense expression observed in the part of cortex dorsal to the MEC.

3.1.3   Neurochemical quantification of the MS projection to the MEC

The MS terminals in the MEC were characterised by staining sagittal brain sections for mCherry and VGAT, VGLUT1 or VGLUT2, and conducting high resolution confocal stack imaging obtaining 3D stack images (fig. 3.3) from MEC LII and LIII. The punctum-to-punctum analysis was conducted using the software Imaris (Bitplane), reconstructing terminals into 3D sphere models (fig. 3.4). Overlap between the red mCherry signal and the green vesicular transporter signal was observed as a yellow merged signal. Results from the co-localisation analysis are presented in figure 3.5.

In sections stained for VGAT, the punctum-to-punctum analysis of 30 257 terminals in LII and 22 643 terminals in LIII labelled with mCherry showed that most puncta co-localised with VGAT puncta (LII: median = 80.18%; LIII: median = 81.41%), suggesting that a majority of the terminals projecting to MEC from MS originate from GABAergic neurons.

In contrast, in sections stained for VGLUT1, the punctum-to-punctum analysis of 41 085 terminals in LII and 33 016 terminals in LIII labelled with mCherry showed that only a few puncta co-localised with VGLUT1 puncta (LII: median = 0.7642%; LIII: median = 2.805%).

Similarly to VGLUT1, in sections stained for VGLUT2, punctum-to-punctum analysis of 27 520 terminals in LII and 33 180 terminals in LIII labelled with mCherry showed that only a few puncta co-localised with VGLUT2 puncta (LII: median = 1.667%; LIII: median = 0.8294%).

There was no apparent layer specific difference in co-localisation for the three markers.

The results is in accordance with previous findings that the main proportion of the MS projection to the MEC is GABAergic, and that glutamatergic projections are relatively rare (Gonzalez-Sulser et al., 2014).

Co-localisation data from all the 3D images are presented in figure 3.6, from left and right hemispheres, different dorsoventral depths and animals. The figure shows a relatively large variation between animals and imaged sections for VGLUT1. This variation seems to be derived from one section from the left hemisphere of rat 1699, and explains the variation observed for VGLUT1 in figure 3.5. The variations in sections stained for VGAT and VGLUT2 were less apparent.
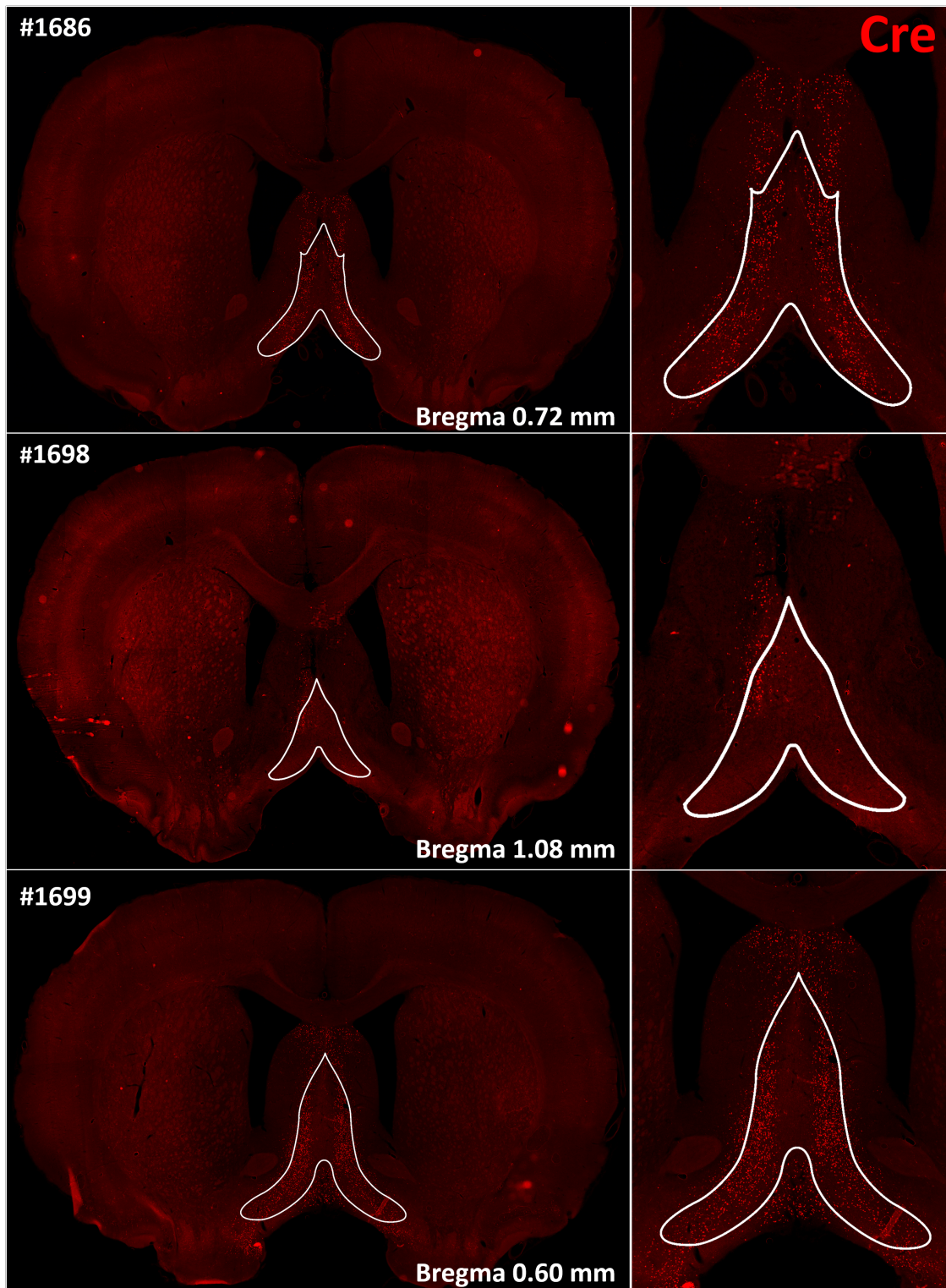
Figure 3.1: Widefield images of coronal sections following viral transduction with synaptophysin-mCherry and Cre recombinase (Cre) of medial septum (MS)-projecting neurons (outlined (Paxinos and Watson., 2007)). (left panels) Cre expression (red). (right panels) The MS at high magnification. Cre expression was observed in the MS in rat 1686, 1689 and 1699.
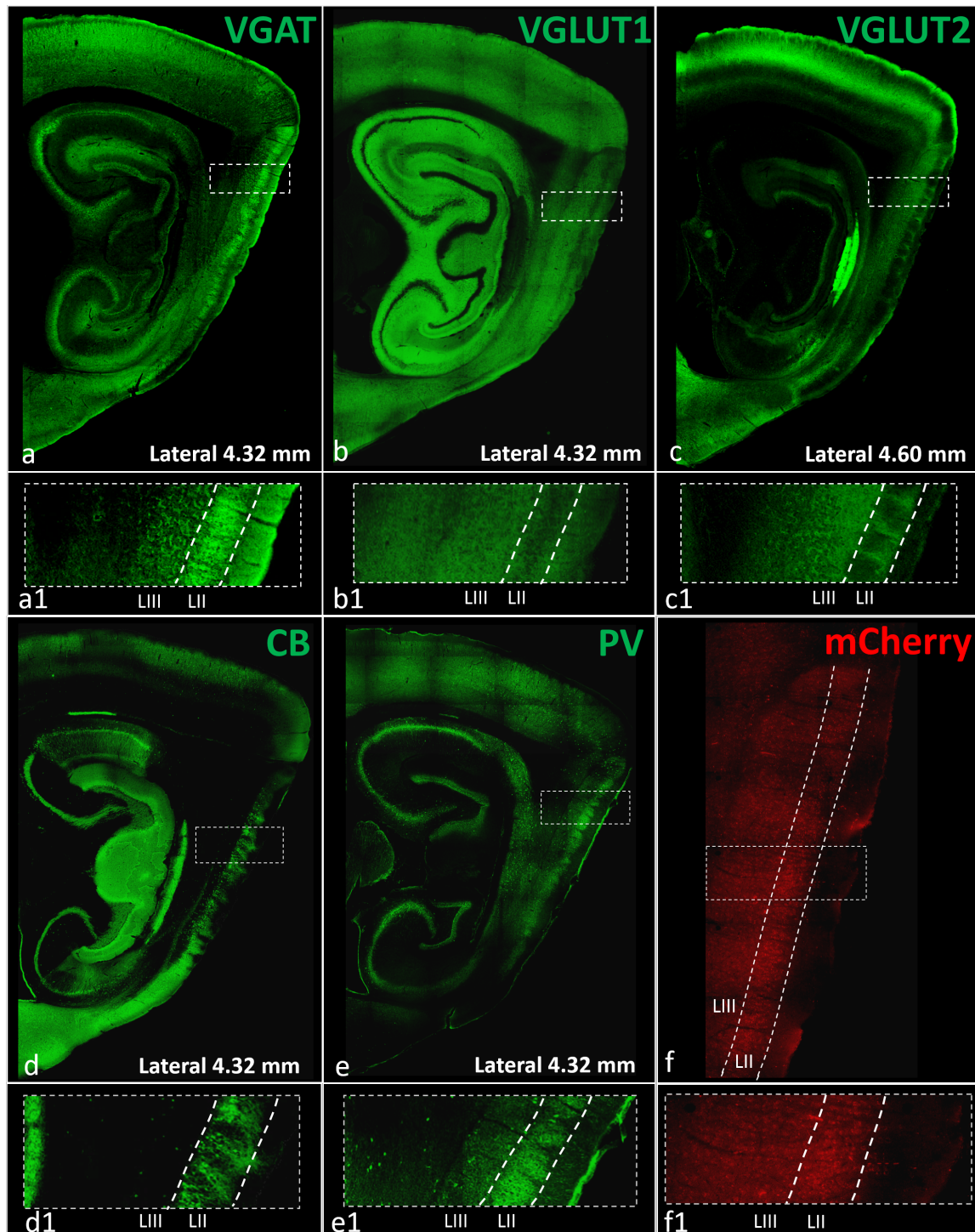
Figure 3.2: Widefield images of sagittal sections showing vesicular transporters (a-c), cell types (d-e) and medial septum-projecting terminals in medial entorhinal cortex (MEC) (f), in accordance with Paxinos and Watson. (2007). The outlined regions show laminar distribution in the MEC (a1-f1). (a, a1) The vesicular GABA transporter (VGAT) was densely expressed in layer (L) II and III. (b, b1) The vesicular glutamate transporter (VGLUT) 1 was less densely expressed in LII compared to LIII. (c, c1) The expression of VGLUT2 was dense in LII and LIII. (d, d1) Calbindin positive cells were densely expressed in LII, with low expression in LIII. (e, e1) Parvalbumin positive cells were strongly expressed in LII compared to LIII. (f, f1) Synaptophysin-mCherry was expressed in LII and LIII, with a slightly denser expression in LII.
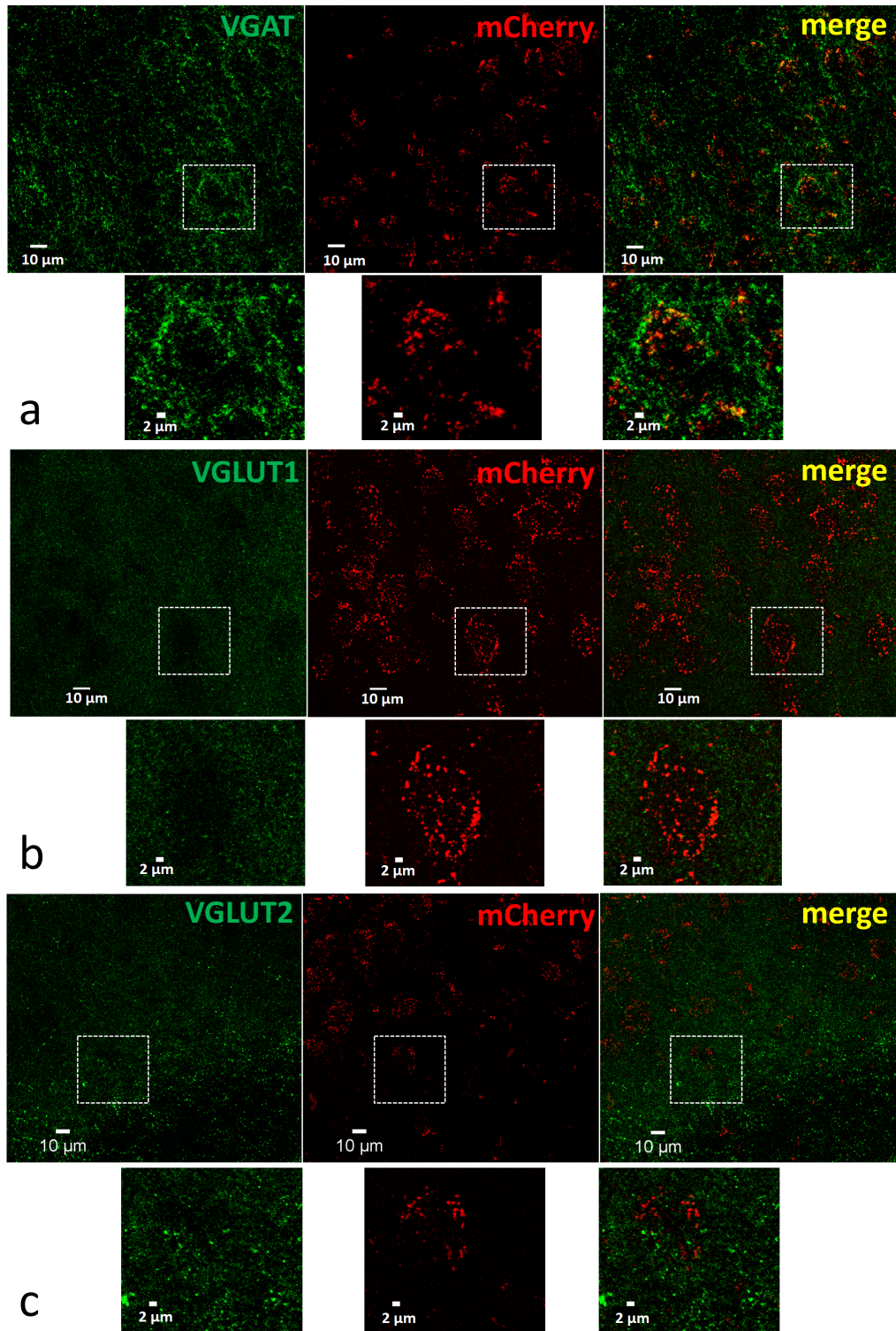
Figure 3.3: Confocal stack images of medial septal terminals (red) in the medial entorhinal cortex, characterised by vesicular transporters (green). The right panels show the merged signal (yellow). Examples from (a) vesicular GABA transporters (VGAT) in layer (L) II, (b) vesicular glutamate transporters 1 (VGLUT1) in LIII, and (c) vesicular glutamate transporters 2 (VGLUT2) in LII.
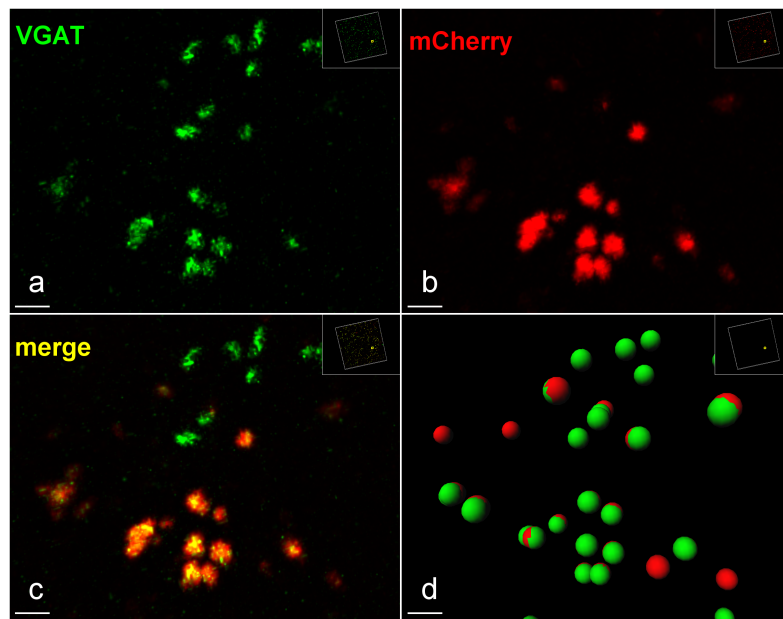
Figure 3.4: Confocal images at high magnification showing (a) medial septal (MS) presyn-aptic terminals (red) in the dorsal medial entorhinal cortex LIII, (b) co-stained for vesicular GABA transporter (VGAT; green). (c) Co-expression of MS terminals and VGAT (yellow). (d) Punctum-to-punctum analysis by reconstructing spheres (1 μm^3) using a spot algorithm. Scale bars: 2 μm.
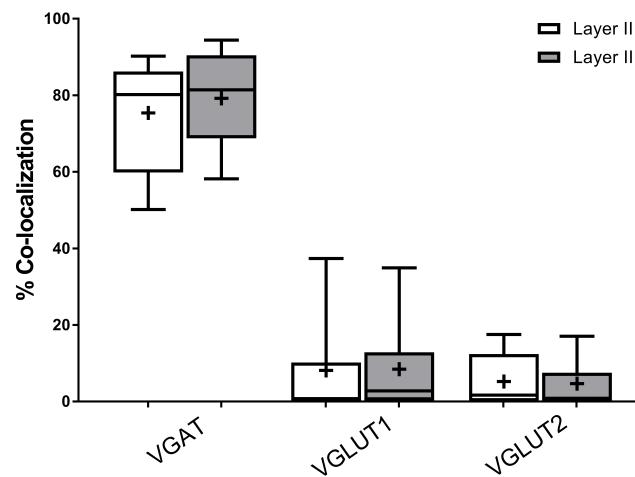
Figure 3.5: Percent co-localisation between medial septal terminal puncta and vesicular trans-porter puncta in medial entorhinal cortex layer (L) II and III. Plots show median values (hori-zontal lines inside boxes), mean values (+), interquartile distances (boxes) and 10-90% of upper and lower values (bars). VGAT (N = 2; LII: $n = 30\,643$, $M = 80.18\%$; LIII: $n = 22\,643$, $M = 81.41\%$). VGLUT1 (N = 3; LII: $n = 41\,085$, $M = 0.7642\%$; LIII: $n = 33\,016$, $M = 2.805\%$). VGLUT2 puncta (N = 3; LII: $n = 27\,520$, $M = 1.667\%$; LIII: $n = 33\,180$, $M = 0.8294\%$)
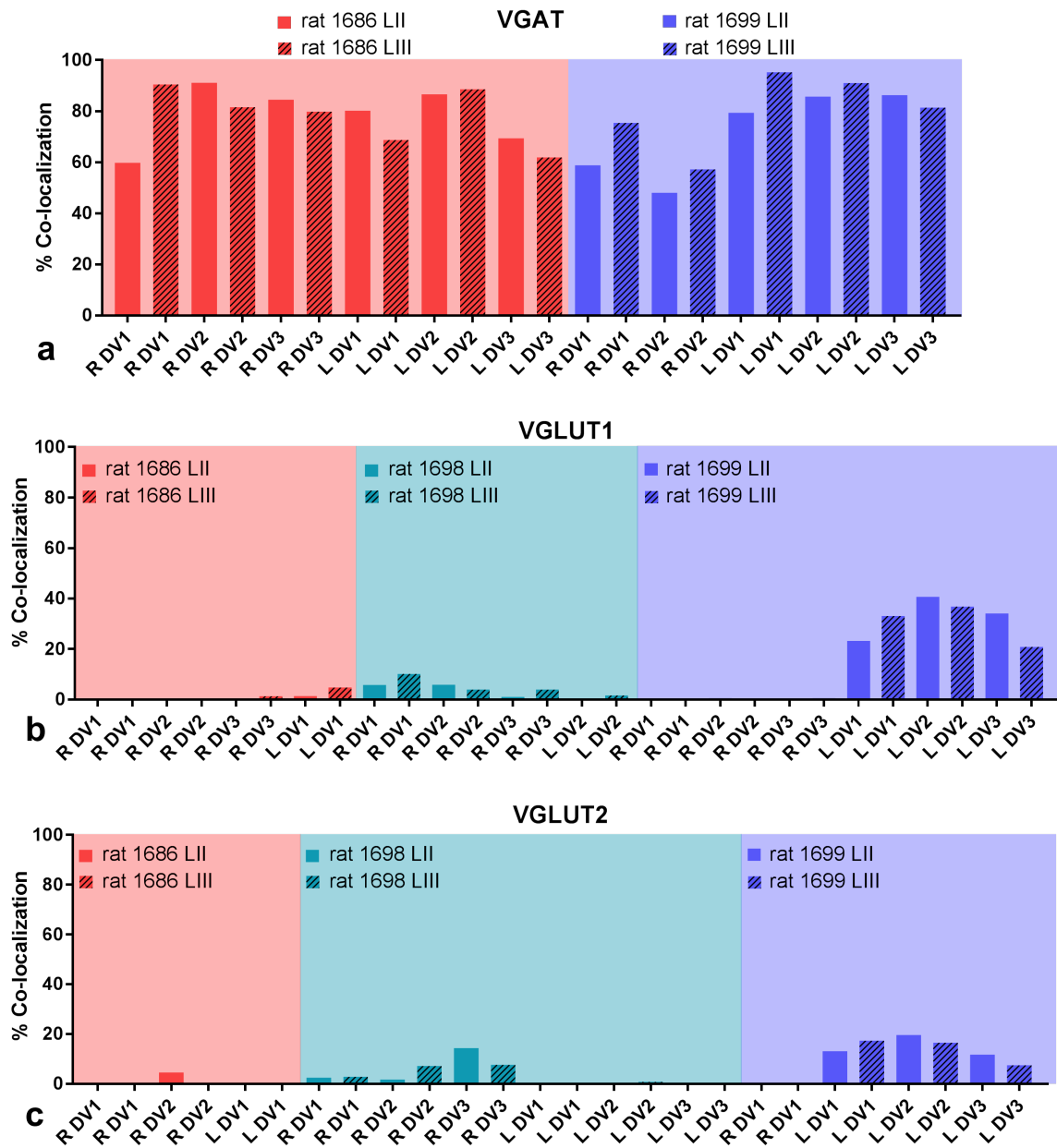
Figure 3.6: Data from all images show the variation between animals and sections. Percent co-localisation in stack images obtained from medial septal terminals characterised by staining for vesicular transporters in the medial entorhinal cortex, for right (R) and left (L) hemispheres, dorsoventral depth (DV1-3), rats and layers (LII/LIII). (a) For the vesicular GABA transporter (VGAT) the variation was smaller compared to vesicular glutamate transporters (VGLUT) 1/2. (b) For VGLUT1 the variation derived particularly from L hemisphere of rat 1699. (c) For VGLUT2 the variation was smaller compared to VGLUT1.

3.1.4   Distribution of cellular markers

In order to investigate post-synaptic targets of the MS projection in the MEC, sections were stained for pyramidal cells expressing CB and inhibitory interneurons expressing PV, two abundant cell-types in the MEC with very different distributions (overview images shown in fig. 3.2 d-e). CB positive cells were found in patch-like assemblies in MEC LII, with very low expression in LIII, particularly in the dorsal MEC, however slightly more expressed in the ventral parts. Some processes reached out to LI. This is in accordance with CB staining of MEC in other studies (Tang et al., 2015; Ray and Brecht, 2016). Due to the low expression in LIII, this layer was excluded from the quantitative analysis.

The PV positive cells were detected in both LII and LIII, with a denser expression in LII. By closer examination, the expression of PV in LII appeared to be caused by more neuronal processes (axons and dendrites) rather than increased number of cell bodies. Similar results from PV staining was observed in the study of Boccara et al. (2015), in which LII was more densely stained compared to more moderate staining in LIII. The bright band along the section border in LI was likely a staining artefact.

3.1.5   Neurochemical quantification of the MS projection to cell types in the MEC

To determine postsynaptic targets of MS projection neurons in the MEC, co-localisation analyses (fig. 3.7, 3.8 and 3.9) were conducted on stack images obtained from sagittal sections stained for mCherry and CB or PV. Overlap between the red mCherry signal and green signal from markers for CB or PV was observed as a yellow merged signal. The punctum-to-cell analysis was conducted using the software Imaris (Bitplane), and provides co-localisation data from number of synapses per cell. It also provides cell volume measurements for defined cell regions of interest (RIO), here limited to the cell soma. This allows for quantification of synapses per unit cell volume.

To determine whether cell volume was a significant factor for the quantification, firstly, the distribution of cell volumes for each single cell in the MEC, included in the analysis, was investigated (fig. 3.10 a-c). The results revealed a great variation in the volume of PV- and CB positive cells in the MEC. From analysis of 418 CB positive cells, 86 PV positive LII cells and 55 PV positive LIII cells, the major proportion of cells were in the range of 100-1700 μm^3 for all three populations. PV positive cells in LII appeared smaller in size, mainly 500-900 μm^3, compared to CB positive cells and PV positive LIII cells. Secondly, the MS synaptic puncta were quantified relative to cell volume for each cell (fig. 3.10 d). From the analysis of 8784 MS terminals to CB positive cells, 3480 MS terminals to PV positive LII cells, and 1577 MS terminals to PV positive LIII cells, the number of synaptic puncta increased relative to cell volume for all three markers (CB: R^2= 0.5616; PV LII: R^2= 0.4522; PV LIII: R^2= 0.5309). Due to the variations in cell volume for all markers, and the increase in co-localising synapses as volume increased, the volume appeared to be a significant factor for the quantitative analysis.

Results from the punctum-to-cell analysis is presented for puncta per unit cell volume (fig.

3.11 a) and for puncta per individual cell (fig. 3.11 b). The two analytical methods provide different results. From the puncta per cell volume analysis, a Kruskal-Wallis and *post hoc* Dunn's test revealed that MS input to CB positive cells was lower relative to PV positive LII cells ($p < 0.0001$), but not different from input to PV positive LIII cells ($p > 0.9999$). MS input to PV positive LII cells was higher relative to PV positive LIII cells ($p > 0.0001$). From the puncta per cell analysis, a Kruskal-Wallis and *post hoc* Dunn's test revealed that MS input to CB positive cells was lower relative to PV positive LII cells ($p < 0.0001$), but not different from input to PV positive LIII cells ($p > 0.3136$). MS input to PV positive LII cells was not different from input to PV positive LIII cells ($p > 0.0763$).

From the above analysis and difference in the presentation of data from the plots (fig. 3.11), the puncta per cell volume analysis seems to more accurately describe the MS synaptic connectivity with cells in the MEC. This is in line with simulation data studying 3D structures, in which unit volume values provided data suitable for statistical analysis of marker-defined cells, and especially for irregular structures, such as cells (Caster and Kahn, 2012). The results indicate that MS more frequently innervate PV positive cells in LII compared to CB positive cells and PV positive cells in LIII.

Co-localisation data from all the 3D images are presented in figure 3.7 for puncta per cell volume, from left and right hemispheres, different dorsoventral depths and animals. A small variation was observed for CB positive cells. For PV LII cells, the most dorsal image from the right hemisphere of rat 1698 seemed to be considerably elevated from the other image stacks. Similarly, the most dorsal image stack from the right hemisphere of rat 1686 seemed to be slightly elevated compared to the other images for PV LIII.
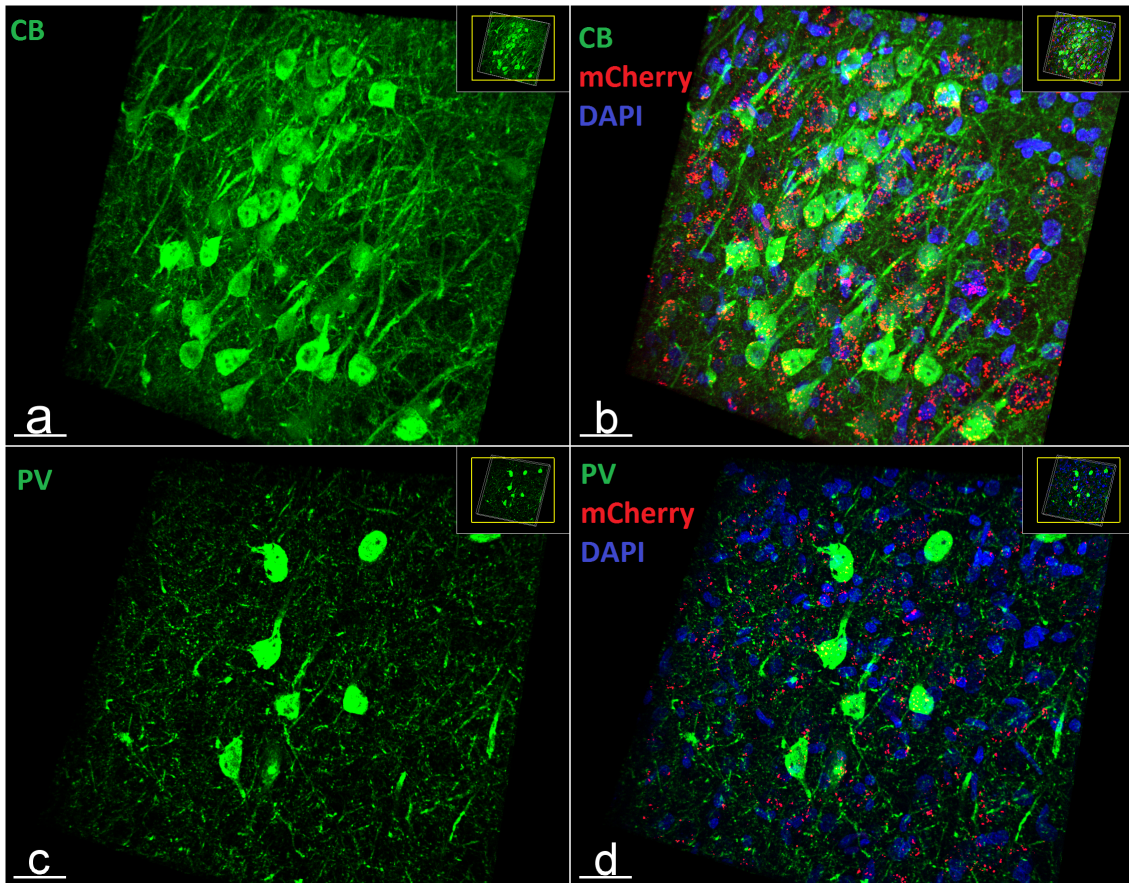
Figure 3.7: Confocal stack images of medial septal (MS) terminals stained for mCherry (red) and cell types (green) in the medial entorhinal cortex. (a) Cells stained for calbindin in MEC layer II, (b) image a with MS terminals and nuclei (blue), (c) cells stained for parvalbumin in MEC LII, (d) image c with MS terminals and nuclei. Scale bars: 30 μm.
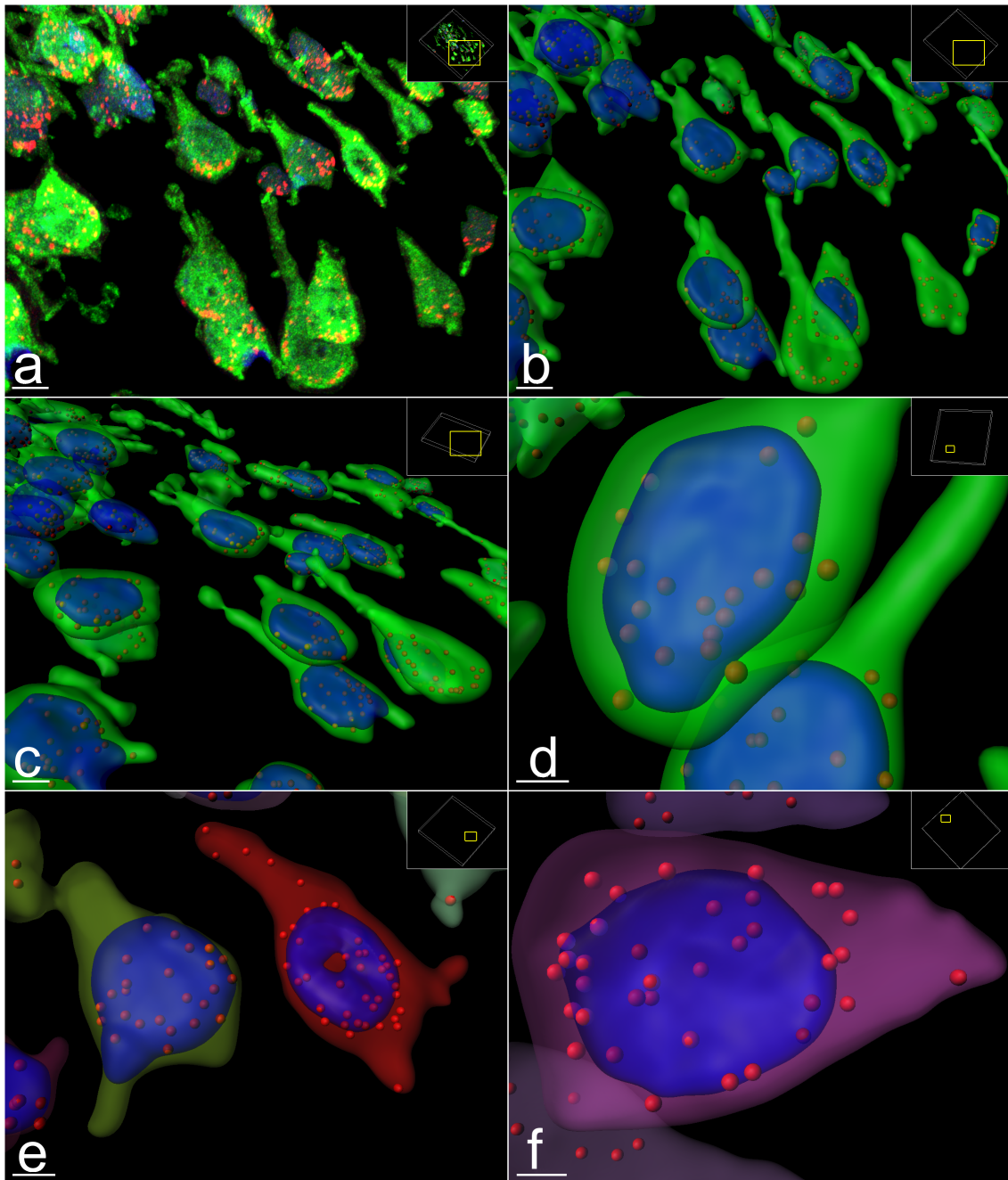
Figure 3.8: Confocal stack images and cellular reconstruction of isolated medial septal (MS) presynaptic terminals to postsynaptic pyramidal cells in MEC LII. (a) MS terminals stained for mCherry (red) on cells stained for calbindin (green), and nuclei stained with DAPI (blue). (b-f) Reconstructed 3D models based image a. MS terminals are spheres of 1 μm³. (e-f) Colour coding distinguish individual cells. Scale bars: (a-c) = 10 μm, (d-e) = 5 μm, (f) = 4 μm.
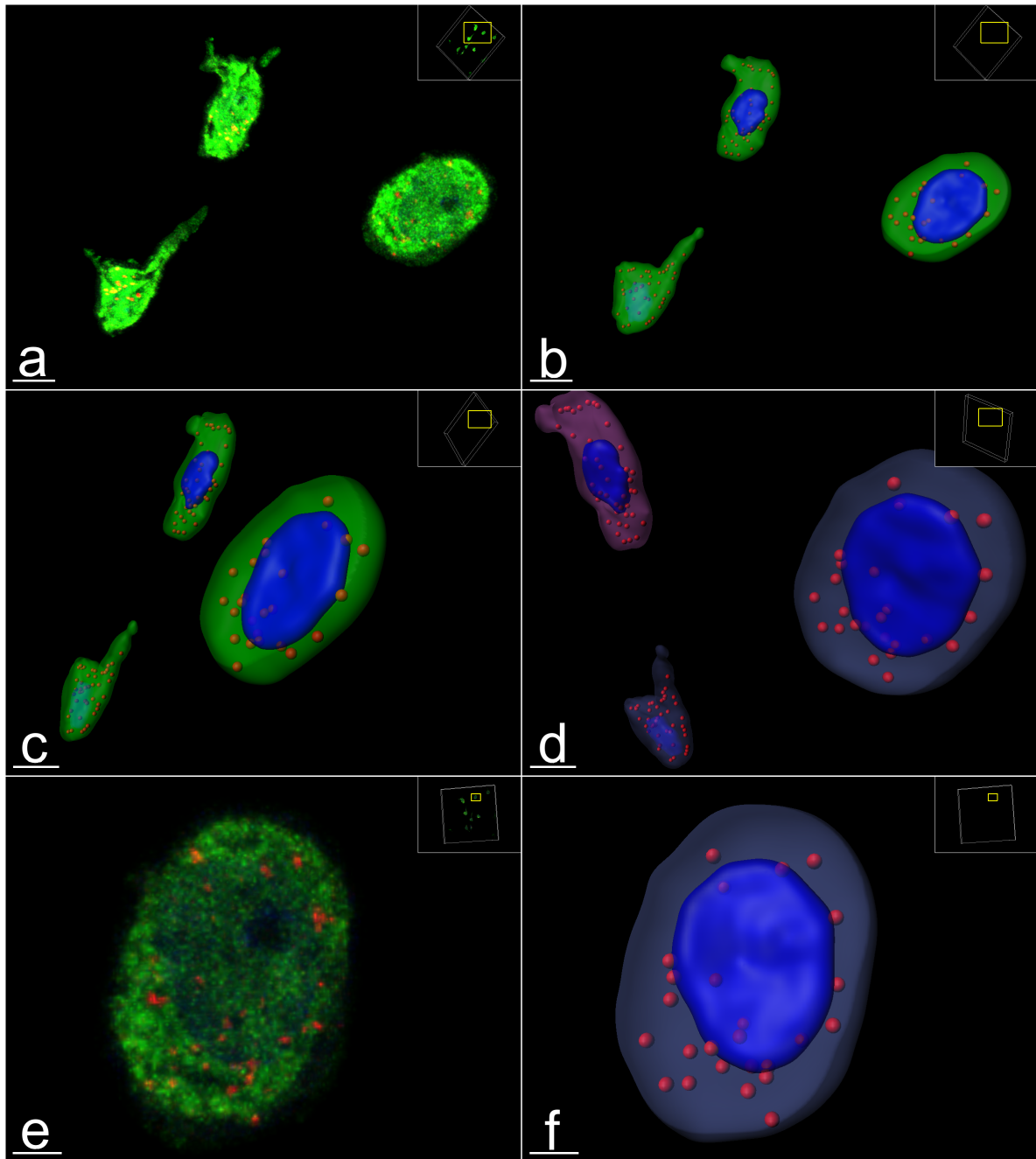
Figure 3.9: Confocal stack images and cellular reconstruction of isolated medial septal (MS) presynaptic terminals to postsynaptic parvalbumin cells in MEC LII. (a) MS terminals stained for mCherry (red) on parvalbumin positive cells (green) in MEC LII and nuclei stained with DAPI (blue). (b-d) Reconstructed 3D model based on image a. MS terminals are spheres of 1 μm^3. (e-f) One cell shown at high magnification. (d, f) Colour coding distinguish individual cells. Scale bars: (a-d) = 10 μm, (e-f) = 4 μm.
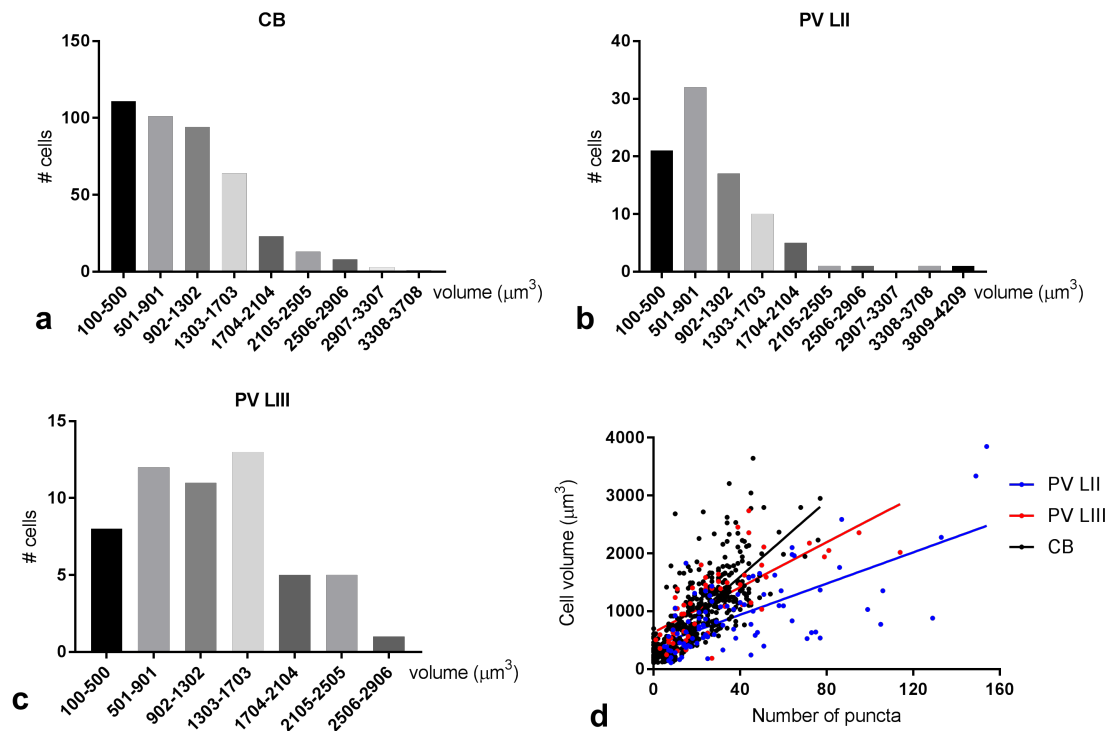
Figure 3.10: (a-c) Distribution of cell volumes of postsynaptic cells in the medial entorhinal cortex stained for calbindin (CB), and parvalbumin (PV) in layer II (LII) and III (LIII). CB (N = 3, n = 418), PV LII (N = 3, n = 86) and PV LIII (N = 3, n = 55) mainly ranged in size from 100 to 1700 μm^3. PV cells in LIII appeared to be larger compared to PV cells in LII. (d) Scatterplots with linear regression (lines) showing the relationship between presynaptic medial septal puncta and postsynaptic cell volume (μm^3) for medial entorhinal cortical cells stained for CB ($n = 8784$, $R^2 = 0.5616$), and PV in layer II ($n = 3480$, $R^2 = 0.4522$) and layer III ($n = 1577$, $R^2 = 0.5309$). The number of synaptic puncta increased relative to cell volume for all three markers.
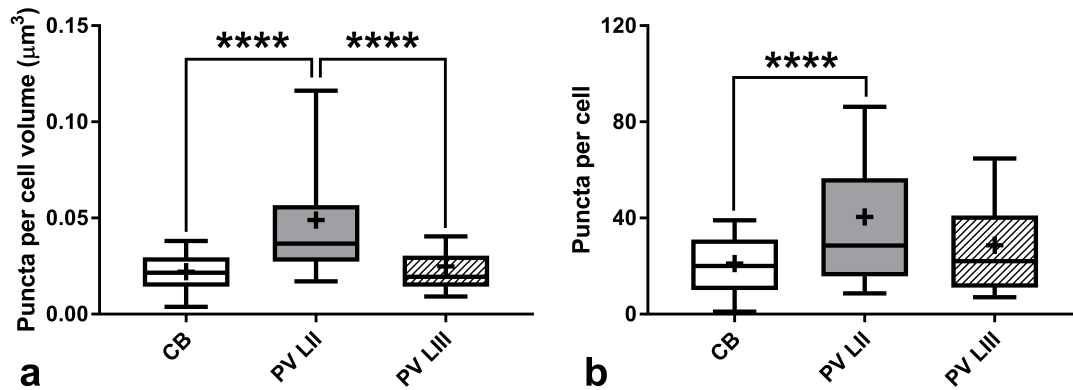
Figure 3.11: Quantification of medial septal presynaptic terminals to postsynaptic calbindin+ (CB) cells in layer (L) II (N = 3, n = 418, n = 8784), parvalbumin+ (PV) cells in LII (N = 3, n = 86, n = 3480) and LIII (N = 3, n = 55, n = 1577) of the medial entorhinal cortex. Plots show median values (horizontal lines inside boxes), mean values (+), interquartile distances (boxes) and 10-90% of upper and lower values (bars). Statistical significance is indicated (*) for the Kruskal-Wallis and *post hoc* Dunn's tests. (a) Puncta per cell volume (μm^3) for CB (M = 0.0215), PV LII (M = 0.0367), and PV LIII (M = 0.0195) cells. CB was different from PV LII (****p < 0.0001), but not from PV LIII (p > 0.9999). PV LII and PV LIII were not different from each other (****p < 0.0001). (b) Puncta per cell for CB (M = 20), PV LII (M = 28.5), and PV LIII (M = 22) cells. CB was different from PV LII (****p < 0.0001), but not from PV LIII (p > 0.3136). PV LII and PV LIII were not different from each other (p > 0.0763).
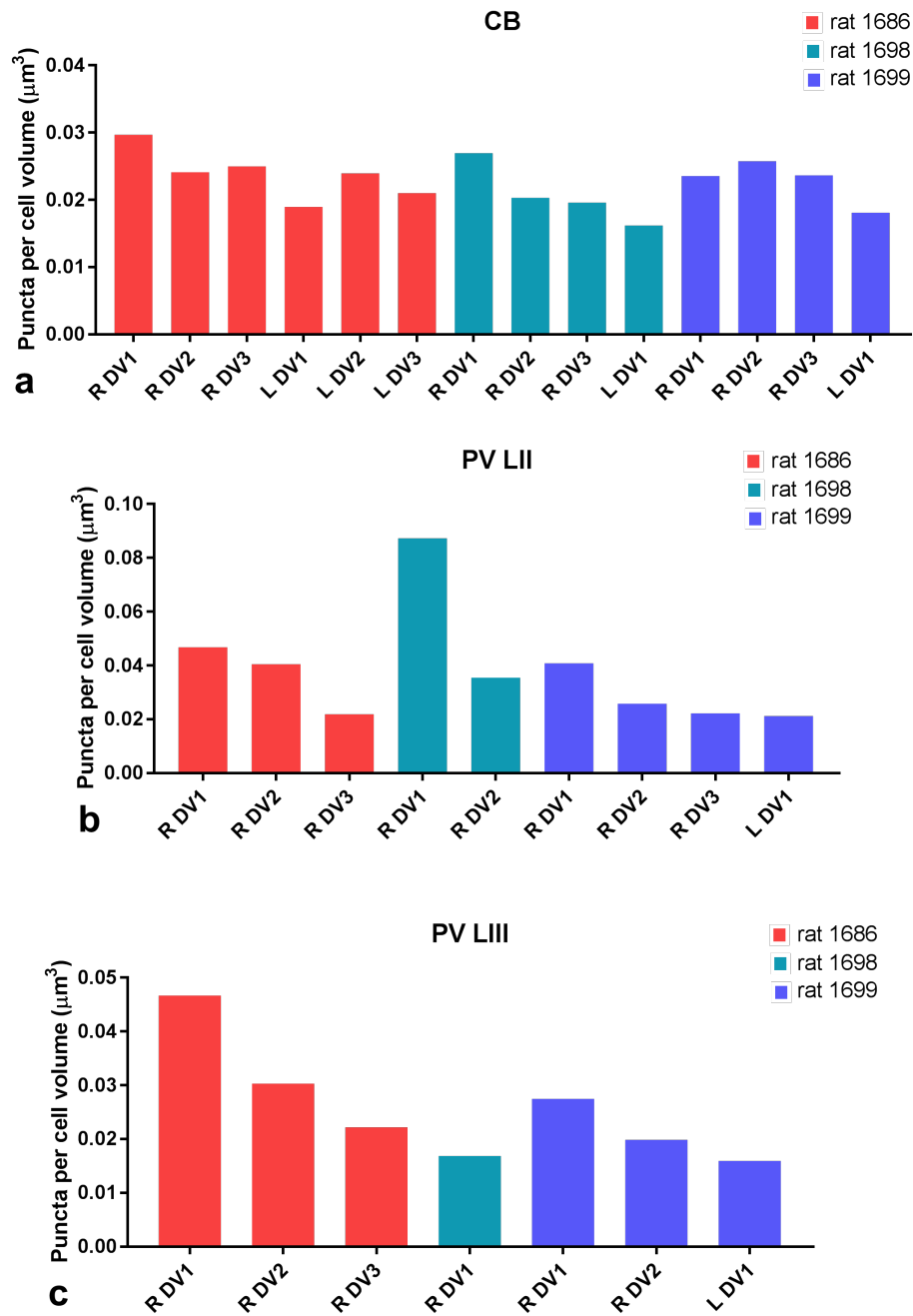
Figure 3.12: Data from all images show variation between animals and sections. Puncta per cell volume (μm^3) for stack images obtained from medial septal terminals to cell types in the medial entorhinal cortex show the variation between right (R) and left (L) hemispheres, dorsoventral depth (DV1-3) and rats. (a) For calbindin (CB) cells the variation was small. (b) For parvalbumin (PV) LII cells R DV1 is higher compared to the other images. (c) For PV LIII R DV1 differs from the other images.

3.2   Part II: Optogenetic perturbations and electrophysiological recordings

Results are based on electrophysiological recordings from nine animals (N) of which single unit data with observed response to optogenetic stimulation were obtained from four of these animals. Data from the other animals were excluded from the analyses as they did not show response to the optogenetic stimulation. Complete analyses of electrophysiological data were beyond the scope of the current master thesis. My contributions were training of animals, electrophysiological recordings, optogenetic stimulation and histology. Surgeries were conducted by M. Lepperød and M. Fyhn. Analyses and many of the recordings were conducted by M. Lepperød. In the current thesis, data was used for functional verification of the identity of the MS projections and their postsynaptic targets in MEC. The findings reported are preliminary and comprehensive analyses of the data set will be conducted for conclusive results.

The neurochemical analyses indicated that the primary proportion of the MS projection is inhibitory GABAergic, and that PV positive interneurons in MEC LII receives more MS input compared to PV LIII and CB LII cells. Based on the layer specific most likely inhibitory input to PV LII cells and previous studies stating that the MS GABAergic projection primarily targets inhibitory MEC interneurons (Gonzalez-Sulser et al., 2014; Fuchs et al., 2016), and that principal MEC neurons are interconnected via inhibitory interneurons (Couey et al., 2013; Pastoll et al., 2013; Fuchs et al., 2016), one would expect the distal MS GABAergic projection to disinhibit principal MEC neurons especially in LII, and also to some extent in LIII. Due to time restraints, layer specificity could not be addressed from the limited data, however, general remarks across LII/III could be drawn. If the theta oscillations from direct connections between the MS and the MEC are required for grid cell spatial coding, one would expect grid cell spatial periodicity to be disrupted from perturbations of this projection, which has been found during inactivation of the MS (Brandon et al., 2011; Koenig et al., 2011). To test these predictions, MEC single units and LFP was electrophysiologically recorded during optogenetic activation either of cells in the MS from an optic fibre placed in the MS, or of the MS-MEC projection from an optic fibre placed in the MEC. Single units were classified as either excitatory or inhibitory based on waveform parameters. Grid cells and non-grid cells were classified based on rate maps of the recording arena showing spatial periodicity. The LFP and single units were recorded before, during and after optogenetic stimulation.

3.2.1   Optogenetic activation of the MS-MEC projection

We first sought to investigate single unit responses to optogenetic stimulations of the MS-MEC projection. By turning on the blue light in MEC, only the presynaptic processes from MS that expressed channelrhodopsin would be activated. In response to stimulations in the MEC, we observed that putative inhibitory neurons showed a decreased firing rate almost immediately to stimulation, followed by an increase in firing rate (N = 3; fig. 3.13). In contrast, we

observed that the grid cells' firing rate showed an increase in activity, followed by a period of silence. The reduction in firing rate 10-20 ms after onset of the laser stimulation in both grid cells and inhibitory neurons could be due to the activation (disinhibition) of the interneurons shown in figure b. The response occurred within the grid cells firing fields, indicating that grid cells' spatial coding is robust to perturbations of the LFP theta oscillations. In non-spatial excitatory cells the response appeared to be somewhat similar to inhibitory cells (fig. 3.14), with a short decrease in firing rate, followed by increased firing rate. Furthermore, from a very limited number of cells (n = 4; fig. 3.13 a, 3.15), grid cells showed variations in waveforms.
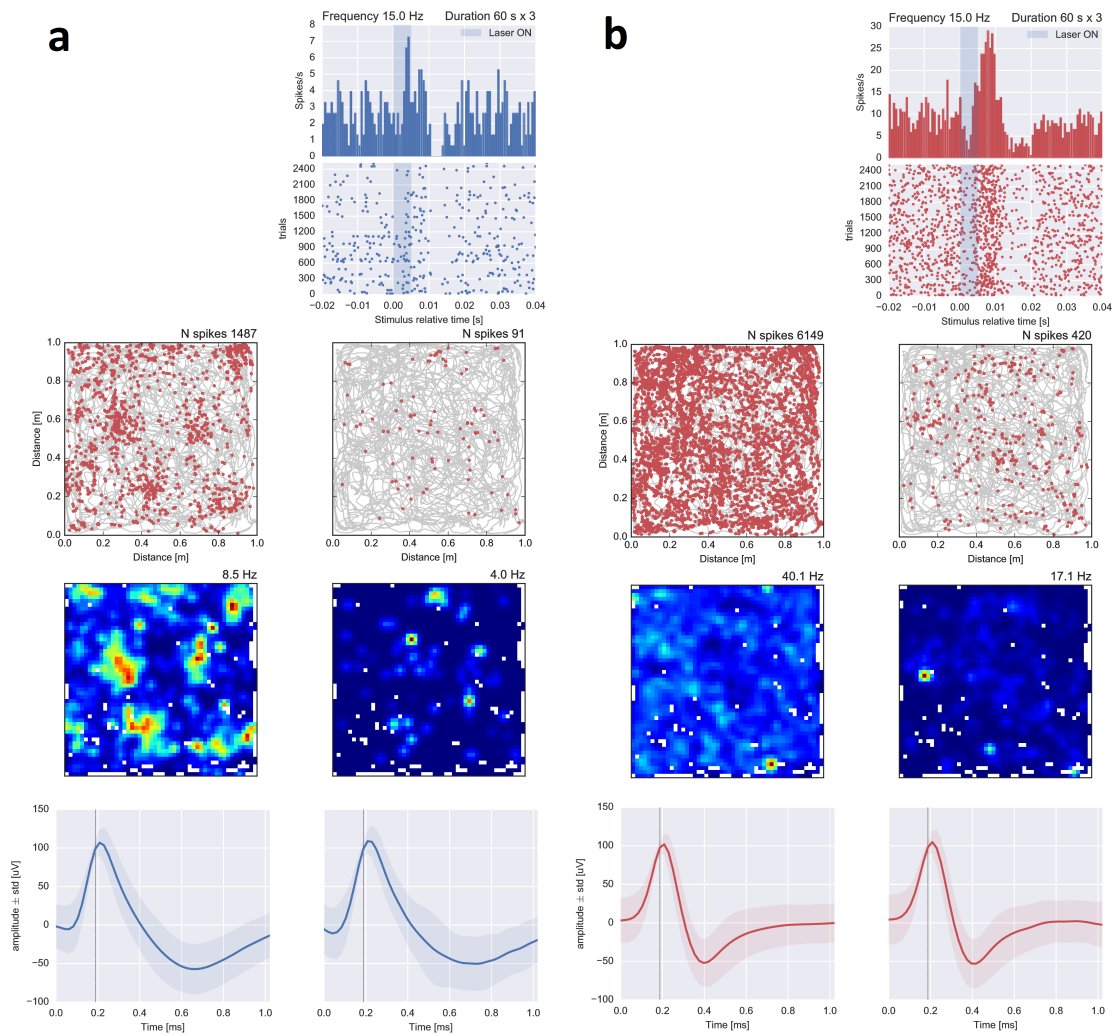
Figure 3.13: Single unit responses to optogenetic activation of the medial septum projection to the medial entorhinal cortex. Example of two simultaneously recorded neurons (a) grid cell, (b) interneuron, both from layer II in rat 1602 (Light pulses were delivered at 11 Hz for 60 seconds and each light pulse lasted 5 ms). Top panels: spike time histogram showing spikes per trial relative to stimulus onset. Below in rasterplot showing every spike. Middle panels: rat running path in grey with red dots showing spike activity. Colour coded rate map, in which increased firing rate is indicated in warmer colours. Bottom panels: single unit waveform before (left panels) and during (right panels) stimulation. (a) Grid cells showed an increase in firing rate. (b) Putative inhibitory cells showed a short decrease in firing rate, followed by increased firing rate.
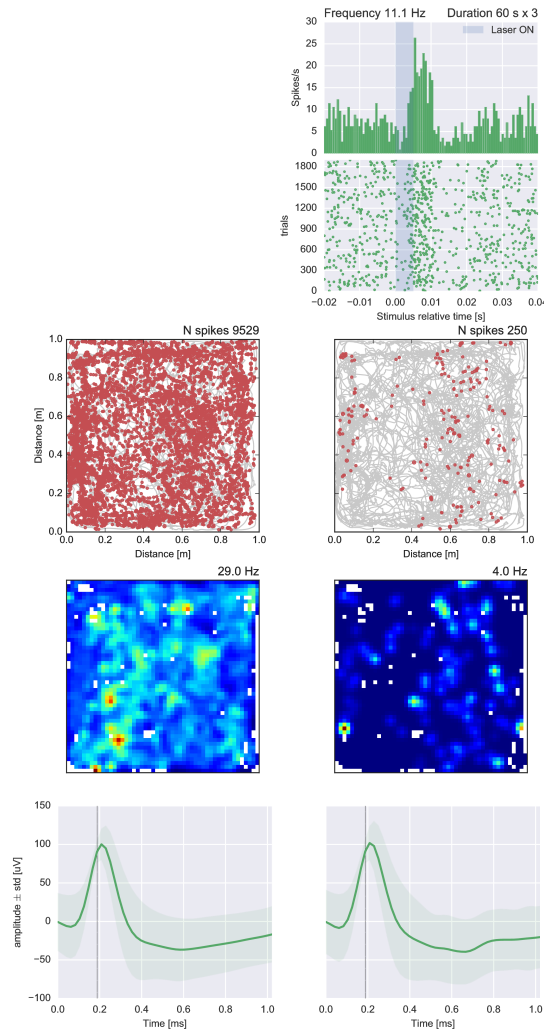
Figure 3.14: Single unit responses to optogenetic activation of the medial septum projection to the medial entorhinal cortex. Example of one recorded non-spatial excitatory neuron from layer II in rat 1602 (Light pulses were delivered at 11 Hz for 60 seconds and each light pulse lasted 5 ms). Top panels: spike time histogram showing spikes per trial relative to stimulus onset. Below in rasterplot showing every spike. Middle panels: rat running path in grey with red dots showing spike activity. Colour coded rate map, in which increased firing rate is indicated in warmer colours. Bottom panels: single unit waveform before (left panels) and during (right panels) stimulation. Non-spatial excitatory cell showed a short decrease in firing rate, followed by increased firing rate.
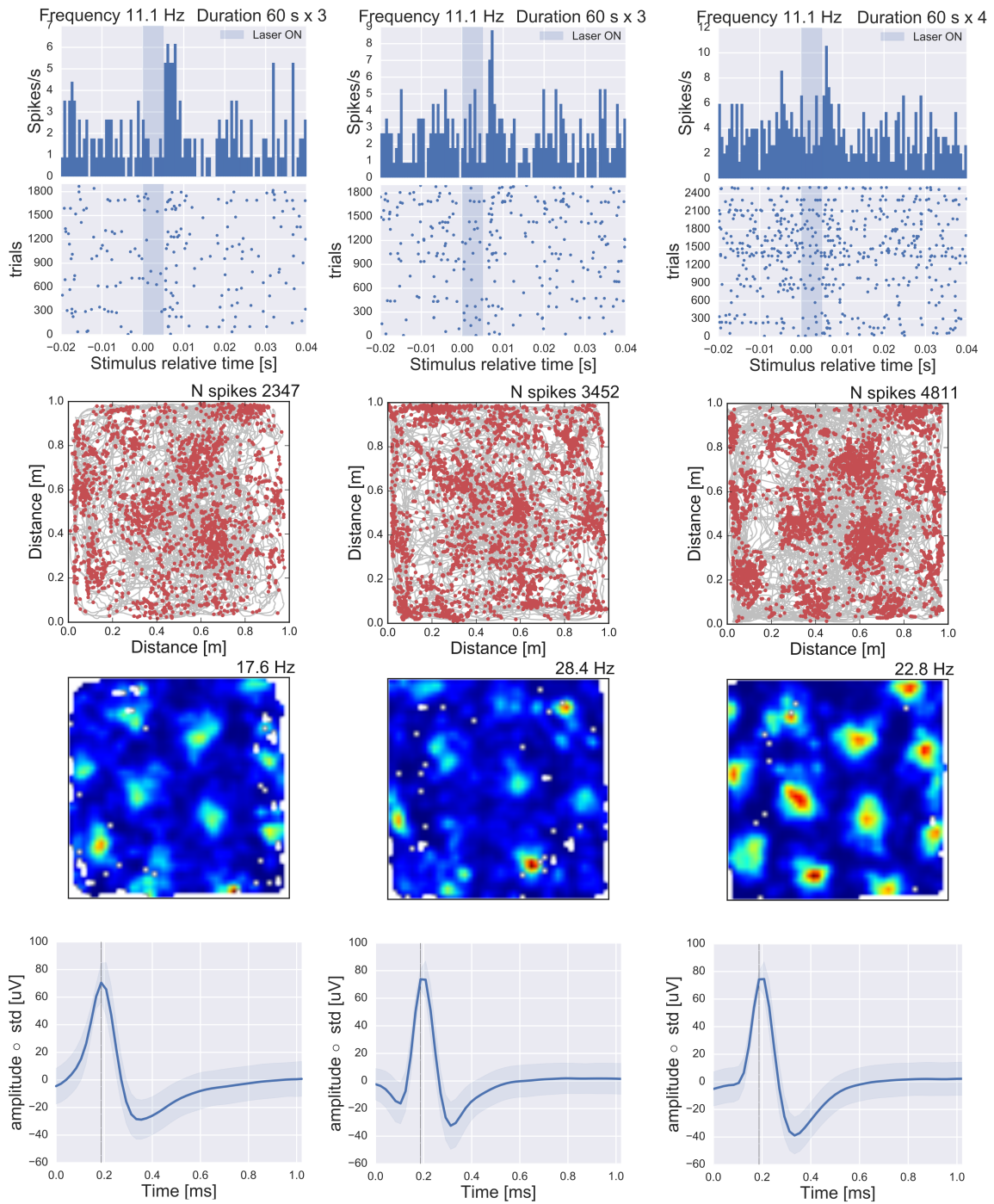
Figure 3.15: Grid cell responses to optogenetic activation of the medial septum projection to the medial entorhinal cortex. Examples of three recorded grid cells from layer III in rat 1596 (Light pulses were delivered at 11 Hz for 60 seconds and each light pulse lasted 5 ms). Top panels: spike time histogram showing spikes per trial relative to stimulus onset. Below in rasterplot showing every spike. Middle panels: rat running path in grey with red dots showing spike activity. Colour coded rate map, in which increased firing rate is indicated in warmer colours. Bottom panels: single unit waveform before (left panels) and during (right panels) stimulation. Grid cells showed an increase in firing rate following the stimulation.

3.2.2   Optogenetic activation of neurons in the MS

In two animals, we observed altered LFP following stimulations of MS neurons. From optogenetic activation of the MS projection at 11 Hz, the dominating theta oscillations were shifted from the endogenous oscillations of about 8 Hz to 11 Hz (N = 2; fig. 3.16). Grid cell responses were recorded in one of these animals. We observed a coherent, meaning correlating phase and frequency, spiking of grid cells and LFP both before stimulation, at 8 Hz, and during stimulation, at 11 Hz. No evident effect was observed from stimulations of the MS projection to the MEC.
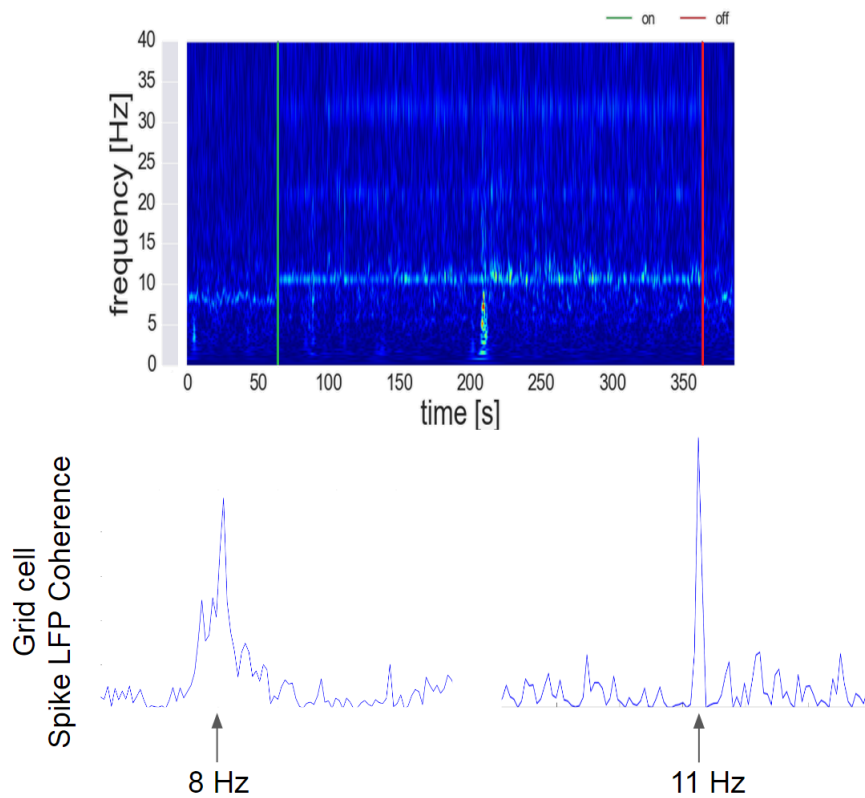
Figure 3.16: Optogenetic activation of the cells in the MS at 11 Hz and electrophysiological LFP and grid cell recordings of MEC in rat 1685. Top panel: showing the dominating frequencies in the LFP signal in warmer colours (wavelet analysis). The LFP theta oscillations were altered from about 8 Hz to 11 Hz during laser stimulation (between green and red lines,). Bottom panel: grid cell spiking and LFP oscillations were coherent both before stimulation at 8 Hz, and during stimulation at 11 Hz.

From the one animal with altered LFP and recorded grid cells, we wanted to investigate whether the observed response in grid cells solely occurred when the rat moved inside the grid fields, or if there was a difference when the rat moved outside the grid fields. From stimulations

in the MS (N = 1; fig. 3.17) inside the grid fields, we observed a strong increase in firing rate. From the same stimulations outside the grid fields, we observed reduced response – a three times weaker increase in firing rate. From the trajectory- and rate maps, the observed responses form both stimulating inside and outside the grid fields occurred within the grid fields. In this animal, less evident effect was observed from stimulating the MS projection to the MEC.
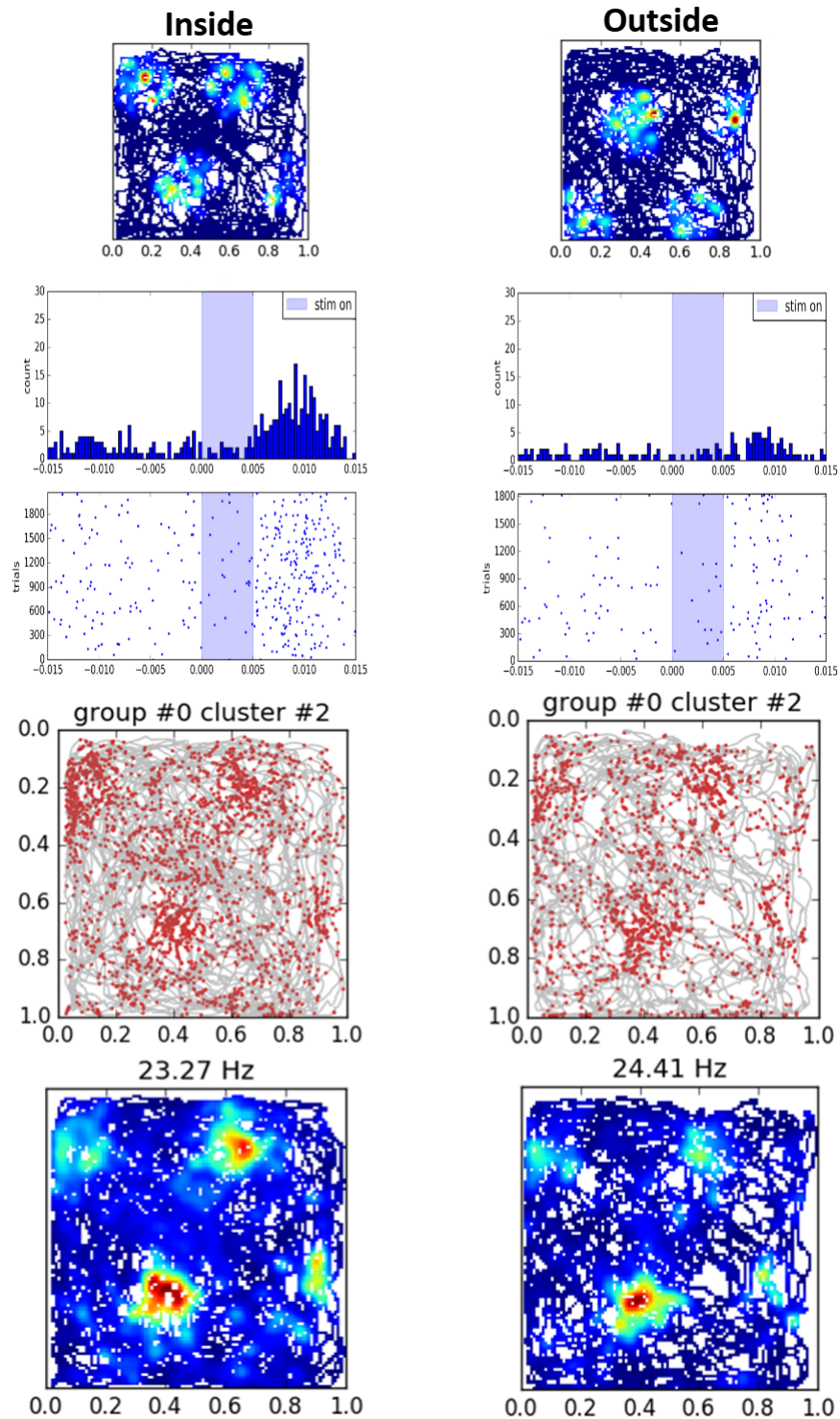
Figure 3.17: Grid cell responses to optogenetic activation of the medial septum projection at 11 Hz frequency inside and outside the grid fields. Recordings from one grid cell in rat 1685, left hemisphere, layer II. (Top panels) Laser light activation pattern in the recording arena. (Middle panels) Spikes per second (count) and spikes per trial relative to stimulus time. (Bottom panels) Spatial distribution of spiking activity (red) from the rats trajectory (grey) and colour coded rate map, in which increased firing rate is indicated in warmer colours. Stimulation inside grid fields showed a strong increase in firing rate within the grid fields, whereas stimulations outside showed a three fold reduction in response within the grid fields.

3.2.3   Histology

The expression pattern of ChR (fig. 3.18) following viral injections in the MS was investigated from histology sections of MS and MEC hemispheres stained for GFP, which was expressed in conjugation with ChR. Dense expression was observed in LII and LIII of the MEC, along with clear expression around the injection site in the MS. To reveal the depths of tetrode and optic fibre positions in the MEC, sections were stained for Nissl bodies (fig. 3.18). In rat number 1596, the tetrodes and optic fibre tracks were measured to 3070 μm and 3441 μm in LIII for right and left MEC hemispheres, respectively. In rat number 1602, the tetrodes and optic fibre tracks were measured to 2001 μm and 3245 μm in LII/III for right and left MEC hemispheres, respectively. In rat number 1684, the tetrodes and optic fibre track was measured to 2402 μm in LIII for the right MEC hemisphere. In the left hemisphere, implantation tracks were missed from the histological examinations but the signature of the LFP theta oscillations from electrophysiological recordings suggested that the electrodes were positioned in the entorhinal area. In rat number 1685, the tetrodes and optic fibre tracks were measured to 4657 μm and 3490 μm in LII/III for right and left MEC hemispheres, respectively.
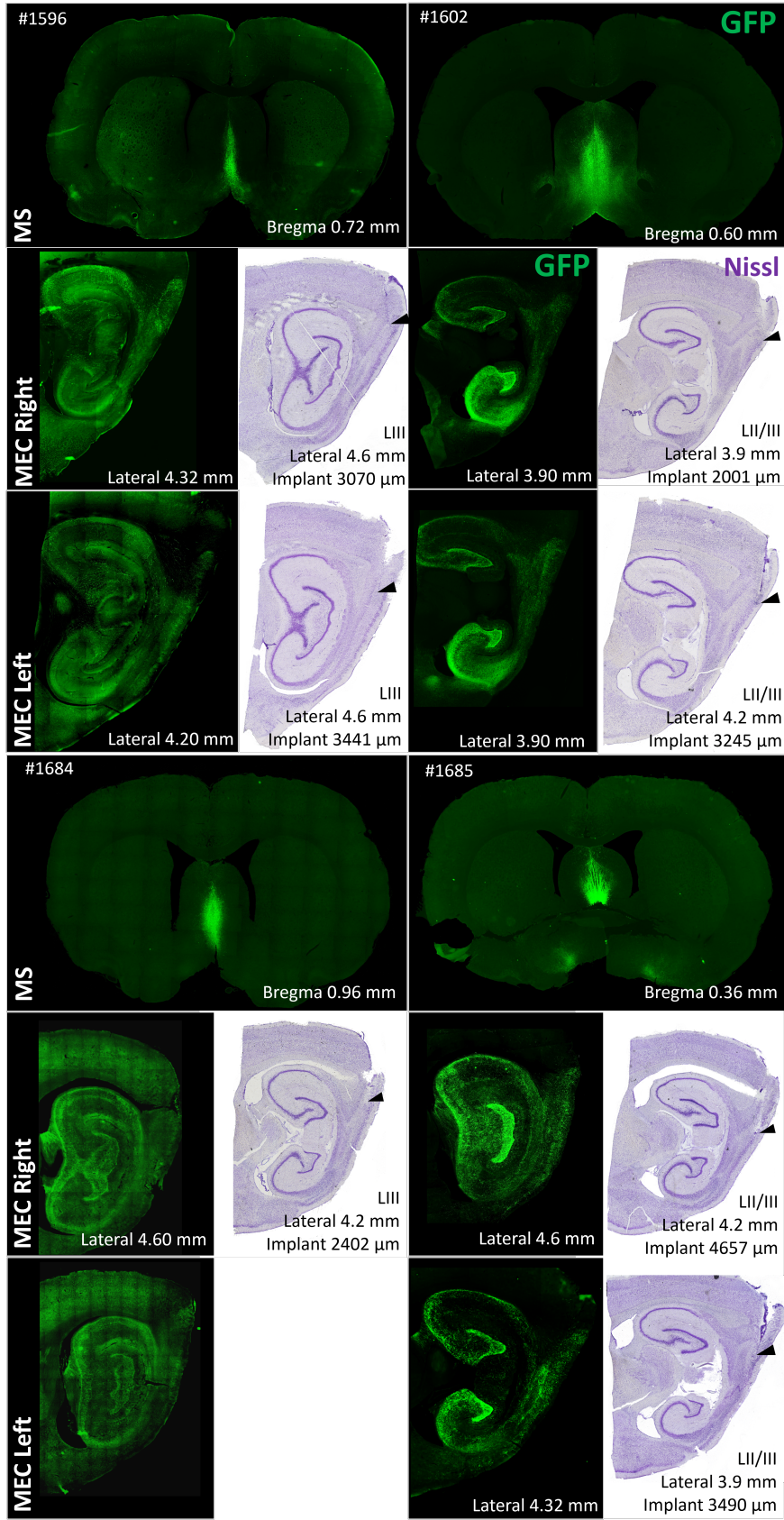
Figure 3.18: Widefield images of: coronal sections (top) show ChR-GFP transduction of medial septal (MS) neurons for each rat (#); sagittal sections (left for each rat) show projecting neurons from the MS in the medial entorhinal cortex (MEC) and; sagittal sections (right for each rat) show Nissl bodies, tetrode- and optic fibre tracks (arrows) in the MEC. Coordinated in accordance with Paxinos and Watson. (2007).

4   Discussion

The main findings of the current study were first that the projection from the medial septum (MS) to the medial entorhinal cortex (MEC) was identified as mainly inhibitory. Secondly, the projection targets cell types differently in the MEC, in which PV positive interneurons in layer II receive an almost twofold more MS input compared to PV layer III and CB layer II cells. My thesis provides the first quantitative description of this projection in the rat brain. Thirdly, following optogenetic activation of the MS projection, our preliminary results indicate that grid cells remain spatially stable during activation of the MS-MEC projection at theta frequency. The inhibitory neurons showed an almost instantaneous reduction in firing rate in response to light onset, which is in line with the notion that MS projections target inhibitory neurons. A prominent effect seen in all cell types was a robust increase in firing rate from the stimulation. In correspondence to the anatomical findings, the data in this thesis indicate that the main effect of MS neurons projecting to the MEC is disinhibition of excitatory neurons, including grid cells. From stimulating the MS projection, we observed a response within the grid fields both from stimulating inside and outside grid fields, and the response was stronger for stimulations inside the fields, indicating that grid cell spatial firing is robust to perturbations of the theta frequency.

4.1   Part I: Anatomical and neurochemical analyses

4.1.1   Methodological considerations

Mapping of neural circuit connectivity using viral vectors provides several advantages over conventional tracers. The rAAV-mediated gene expression is long lasting and robust. Additionally, infected cell bodies are labelled, enabling verification of injection sites and distribution of virus infection. The viral serotype show some degree of cell specific infection efficiency and careful selection of serotype is therefore important to ensure expression in cell type of interest. We chose to use the rAAV8 and rAAV5 for synaptophysin-mCherry and Cre recombinase, respectively. Both serotypes have been found to lead to robust expression of the construct in the viral vector in hippocampal and cortical neurons, with a slightly higher risk of toxicity at high doses for rAAV5 (Royo et al., 2008). A period of six weeks between injection and start of experimental testing was chosen to allow for sufficient expression of the viral vector.

Viral vectors were delivered using a Hamilton syringe. This method might damage the tissue at the injection site. A slow injection rate at two dorsoventral (DV) sites in the MS reduced the risk of damage. In order to reveal the extent of infection and if it hit the target area, post-mortem immunohistochemical staining of brain sections around the injection sites were examined. Secondly, the terminal region of processes from the target area might not be fully expressed with the protein conjugate. To investigate this, the marker protein can be visualised in the terminal region. The fluorescent protein mCherry was used as a marker, but immunohistochemically labelling it with antibodies was necessary to enhance the fluorescent

signal. This method was optimised by L. Bjerke (2016), perfecting the dilution for minimal background signal while still observing a strong signal.

The combination of viral tracing and immunohistochemical labelling allowed for characterisation of terminals and respective target cells. With quantitative co-localisation analysis based on 3D modelling, this method revealed the fraction of glutamatergic and GABAergic neurons projecting from the MS to the MEC, and indicated the proportion of excitatory and inhibitory projections. Using a similar method, Wouterlood et al. (2007) found the sizes of immunostained puncta with vesicular glutamate transporter (VGLUT) 2 3D objects to be considerably larger than that of VGLUT1. The difference in size of synaptic puncta might have affected the quantification of presynaptic terminals in the current study, as the puncta were assumed to be of similar size, with a spherical reconstruction of 1 μm^3, for all synaptic puncta. A solution could have been to reconstruct the synapses using a surface algorithm instead of spots. This was initially tested, but the terminals were found to be too densely packed to actually quantify each individual terminal. Another solution could have been to specifically adjust the spherical size to each individual marker.

The original idea was to compare examination of the synaptic puncta at different MEC DV depths as well as between medial and lateral parts of MEC, in addition to the division between LII and LIII. Time constraints and a small data set did not make this feasible. The data reported are pooled from different DV depths and mediolateral (ML) coordinates. This might have caused bias in the reported results, as the distribution of both MS projections and cell types might vary significantly throughout the MEC.

4.1.2   Viral expression of synaptophysin-mCherry conjugate

Following injection of synaptophysin-mCherry with Cre recombinase (Cre), and by staining for Cre, we detected expression in MS cell bodies (fig. 3.1). This confirmed that the MS was injected with the viral construct. By staining MEC sections for mCherry, the expression of synaptophysin in terminals was confirmed, and consistent with previously found dense septal innervation of the MEC (Alonso and Köhler, 1984; Gaykema et al., 1990). The more dense expression in LII and LIII compared to layer I (LI), and the slightly denser expression in LII compared to LIII, is consistent with the minor stratification of MS projections to the MEC reported in Gaykema et al. (1990), with a preference for LII, layer IV (LIV) and upper part of layer V (LV) . Gonzalez-Sulser et al. (2014) found axonal MS projections to be most densely expressed in LII and LV, compared to LI and layer VI (LVI). The infection was less apparent in the MS of rat number 1698. Despite expression in the dorsolateral part of MS, terminals in the MEC were labelled. This may be in line with previous studies where more lateral parts of MS to project to more medial parts of the entorhinal cortex (EC) and vice versa with very small variations seen when comparing the more dorsal and ventral injections (Gaykema et al., 1990).

4.1.3 Distribution of vesicular transporters

Labelling vesicular transporters in the MEC revealed that both inhibitory and excitatory terminals were distributed throughout the MEC (fig. 3.2). The presence of vesicular transporters for GABA (VGAT) and glutamate (VGLUT1/2) defines excitatory or inhibitory neurons, respectively, in the central nervous system (CNS) (Zander et al., 2010). The VGLUT3, which is found to occur in nonglutamatergic neurons, possibly function in cotransmitter release (Gras et al., 2008), hence was not considered in this study.

The dense expression of VGAT LII with less prominent expression in LIII indicate a strong GABAergic innervation of cells in the superficial layers of MEC. This is in accordance with previous findings, where VGAT is found to be densely distributed throughout the cortex and most pronounced in LII, LIII, LIV and LV and no expression in LI Frahm et al. (2006). The fluorescence observed in LI in the current work was most likely a staining artefact. It is important to note that not all GABAergic terminals are stained with VGAT. Frahm et al. (2006) found 70% of neurons containing glutamate decarboxylase (GAD), which catalyses the decarboxylation of glutamate to GABA, mRNA to also contain VGAT mRNA. Furthermore, VGAT is localised in nerve terminals releasing glycine either in addition to or separately from GABA (Chaudhry et al., 1998)– in which both have been found to strongly inhibit other neurons in the EC (Breustedt et al., 2004). There is thus a possibility that not all VGAT terminals were labelled in this study.

We observed that the distribution of VGLUT1 was less restricted to layers, but slightly less expressed in MEC LII compared to LIII. The VGLUT2 was found in between dark patches traversing LII. Other studies report that VGLUT1 and 2 are complementary distributed throughout the CNS, and are considered to account for the glutamate transport in glutamatergic neurons – VGLUT1 express mainly in the neocortex and hippocampus, whereas VGLUT2 localise largely in the thalamus (Herzog et al., 2006). In the neocortex VGLUT1 has been found abundantly expressed in all regions, whereas VGLUT2 has been found more restricted to the superficial layers, including LII and LIII (Ziegler et al., 2002). A study by Wouterlood et al. (2007), which more specifically investigated the distribution of VGLUT1 and VGLUT2 in the MEC, found VGLUT1 expression to be strong and even in the MEC, with the densest distribution in LIII. They found VGLUT2 to be distributed across layers, however, less densely distributed compared to VGLUT1. Similarly to what is reported here, they found VGLUT2 staining unevenly distributed in clusters, but in contrast, both in LII and LIII. By quantitative comparison of VGLUT1 and VGLUT2, they found VGLUT2 to be 50% less dense.

The functional properties of excitatory and inhibitory neurons has for years been segregated into VGLUT1/2 and VGAT. Recent evidence suggests, however, that these transporters are present in the same nerve terminals in subsets of neurons. VGLUT1 and VGLUT2 (Herzog et al., 2006), VGLUT1 and VGAT (Kao et al., 2004), and VGLUT2 and VGAT (Ottem et al., 2004) are found to co-localise in neuron terminals. This indicates that solely staining for the vesicular transporters can not account for the true function of these neurons. However, the

results give an indication of functional properties and can be further supported by staining for other molecular markers and performing functional assessments.

4.1.4   Characterisation of MS input to the MEC

The MS input to the MEC is found to constitute long-range GABAergic neurons (Köhler et al., 1984; Fuchs et al., 2016), cholinergic (Alonso and Köhler, 1984) and glutamatergic neurons (Manns et al., 2001). Tracing and labelling MS projections in MEC LII and LIII indicated a difference in the contribution of inhibitory and excitatory projections (fig. 3.3, 3.4, 3.5), with the majority being characterised as inhibitory GABAergic terminals ($M = 80$ - 81%). In comparison, only a few of terminals were characterised as glutamatergic (M = 1-3 %). The results were not tested for statistical significance due to exclusion of data from one rat for VGAT, hence they are preliminary. Quantifying the relative GABAergic and glutamatergic input has been attempted in other studies, and is to some degree related to findings reported in the present study.

One retrograde tracer study in mice (Gonzalez-Sulser et al., 2014) has found that a large fraction of projecting cells from the MS to the MEC are GABAergic – by co-labelling MS projections with GAD67, which is the most common GAD isoform in the MS, and parvalbumin (PV). About half were positive for GAD67 and/or PV. The exclusion of other GAD isoforms might explain the lower fraction of GABAergic cells observed here compared to the present study. It is also found that retrogradely labelled septal cells appear in the PV-dense region of MS in mice (Unal et al., 2015), suggesting that they are inhibitory. Co-release of VGAT and VGLUT from the same terminals (see section 4.1.3) might explain the higher VGAT fractions observed in the present study. Gonzalez-Sulser et al. (2014) found 13% of the MS projection to be co-labelled with choline acetyltransferase (ChAT), an enzyme responsible for synthesis of acetylcholine, hence stain cholinergic neurons. This might explain the remaining fraction of the projection which was not labelled here.

Unal et al. (2015) distinguished between thick and smooth axons with large boutons, that were VGAT positive septal GABAergic neurons, and thinner axons with smaller boutons, that were VGAT negative, possibly glutamatergic or cholinergic. This, in addition to size difference in VGAT and VGLUT terminals observed by Wouterlood et al. (2007), might have led to bias in the spherical reconstruction of synaptic terminals.

The large variation in data obtained from VGLUT1 (fig. 3.5), seems to be derived from one brain section from the left hemisphere of one rat (number 1699; fig. 3.6). The large co-localisation percentage observed here compared to the other sections might have been caused by staining errors, however unlikely, as all sections were stained with the same staining solution. Another cause could be microscopy adjustments, as laser intensities and offset levels were slightly adjusted for all the image stacks obtained.

4.1.5 Distribution of cellular markers

Staining for pyramidal cells expressing calbindin (CB) and inhibitory interneurons expressing parvalbumin (PV), revealed that both cell types were expressed in the superficial layers of MEC, with CB particularly expressing in patch-like assemblies in LII, and PV expressing both in LII and LIII, with more densely stained processes in LII (fig. 3.2). Staining pyramidal neurons for CB is reported to solely stain pyramidal neurons in MEC LII, which similarly to the present study appear in cell patches (Tang et al., 2015). The pyramidal cells present in LIII (Boccara et al., 2015) are negligibly labelled with CB in adult rats (Ray and Brecht, 2016), hence seems to not express CB. The negative fluorescence in between the patches in LII are reported to express LIII pyramidal dendrites "avoiding" the CB pyramidal cell patches (Tang et al., 2015). To include LIII pyramidal cells in this study, we could have stained the sections for Purkinje cell protein 4 (PCP4), which labels excitatory cells. Since stellate cells are mainly present in MEC LII, this technique could have represented pyramidal cells in MEC LIII.

The PV staining appeared denser in MEC LII compared to MEC LIII, which is similarly reported in Boccara et al. (2015). The denser expression observed in LII appeared to be caused by cellular processes more densely packed in this layer, however, the distribution of cell bodies seemed similar between both layers. The bright fluorescent band along the PV section borders is most likely a staining artefact.

In comparison reelin expression clearly differentiate layers of the entorhinal cortex with its dense labelling of stellate cells in MEC LII (Unal et al., 2015). This was also the case in the present study, but due to insufficient co-labelling with mCherry, the sections were left out of the analysis.

4.1.6 Septal input to cell types in the MEC

We observed that mapping the MS projection to CB and PV positive cells (fig. 3.11) revealed that PV positive cells in LII received almost twice the input of CB positive cells in LII. Furthermore, there was a laminar difference in the input to PV positive cells in LII compared to LIII, in which LII cells received approximately twice the input.

Quantification of postsynaptic cells of the GABAergic MS-MEC projection has previously been attempted in the mouse brain (Gonzalez-Sulser et al., 2014; Fuchs et al., 2016). On the basis of optogenetic activation of the projection and *in vitro* recordings of postsynaptic potentials in the MEC; inhibitory postsynaptic potentials (IPSPs) were detected in a majority fast spiking (FS) interneurons and a large fraction of low threshold spiking (LTS) interneurons. In contrast, the principal cells negligibly responded – of these only pyramidal cells. All FS interneurons in MEC LII and two thirds in LIII responded. For LTS interneurons the majority of responding cells were located in MEC LIII (Gonzalez-Sulser et al., 2014; Fuchs et al., 2016). Gonzalez-Sulser et al. (2014) tested the glutamatergic projection in a similar fashion and measured excitatory postsynaptic potentials (EPSPs) in the MEC. They found negligible responses in interneurons, no responses in stellate cells, but in some pyramidal cells. Viral

tracing and immunohistochemistry of the MS GABAergic projection to the MEC has found no innervation of LII principal cells (pyramidal and stellate cells) (Unal et al., 2015). The authors found almost all input to be received by different types of GABAergic interneurons, including PV positive basket cells. Together the studies above indicate that the GABAergic MS projection mainly targets MEC interneurons, in which a majority of these are PV LII interneurons which comparably are the FS interneurons. The different fraction of responding FS and LTS interneurons in LII and LIII, might explain the laminar difference in input to PV cells observed in this thesis. More of the input might be received by other interneuron types in LIII, such as the LTS interneurons. In the present study, we found a quite significant innervation of pyramidal cells. This connectivity might be from MS glutamatergic neurons projecting onto the MEC pyramidal cells Gonzalez-Sulser et al. (2014).

The studies mentioned above were performed in mice, and might be different from what is found in the rat brain. The present study does encounter the possibility that cholinergic MS cells might contribute to the innervation of both pyramidal cells and PV cells (Gonzalez-Sulser and Nolan, 2017).

In the present study, we primarily examined inputs to the cell soma. Unal et al. (2015) reported that VGAT labelled MS boutons in mice mainly innervate dendrites of postsynaptic cells. This might have led to an underestimation of the synaptic contacts observed. Additionally, the PV cells were a lot less numerous than CB cells. Less data collected from PV cells might have contributed to quantification bias. The PV LII and LIII cells were obtained from the same sections and thus more comparable than the data obtained from CB cells.

The reported results this part indicate that the postsynaptic targets of this projection constitute both CB positive pyramidal layer II cells, and PV positive layer II and LIII interneurons, in which PV layer II interneurons receives a majority of the input compared to the other two populations.

4.2 Part II: Optogenetic perturbations and electrophysiological recordings

In part I the anatomical mapping of connections and was an indirect measurement of the functional connectivity exploited through neurochemical properties. In order to directly assess the physiological properties of the MS-MEC projection, a combination of optogenetic perturbations and electrophysiological measurements was applied.

4.2.1 Methodological considerations

The results addressed the functional assessments are preliminary and only qualitatively reported. One of the ambitions of this project was to develop procedures for microdrive construction, surgeries, viral vectors and electrophysiological recordings and stimulation protocols. Construction of the microdrive with an optetrode is technically demanding. The optogenetic experiments are dependent on light delivery and electrophysiological recordings from the same neuron population. On one hand the tetrodes could detect stimulation artefacts, on the other hand the light could be shadowed by the tetrodes. This was tried solved by using an optic fibre with a large diameter to limit shadowing by electrodes and tetrodes were cut beyond the end of the fibre, to enable recording of neurons targeted by laser light with diminished light artefacts (Han, 2012).

For viral infection, two different AAV serotypes (5 and 8) were tested as viral vectors for expression of channelrhodopsin (ChR). The difference seemed negligible as we obtained optogenetic response in two animals with different serotypes. Tetrode implantations in brain tissue may cause an inflammatory reaction of the glial cells (Polikov et al., 2005), which may reduce the electrophysiological signal as well as the light range. To detect any sign of damage, the brain sections were stained for Nissl bodies in the areas of implantation. A typical example of damage from the implantation is seen in the right hemisphere of animal 1682 (fig. A.6). The coordinates of implant surgeries (table A.1) varied especially in terms of the angular position of the optetrodes. This did not, however, seem to impact the success rate of the experiments.

During electrophysiological recordings, over amplifying or under amplifying the signal was avoided by adjusting the signal for each channel, both for single units and local field potential (LFP). In the filtering process the LFP signal was high-pass filtered to remove spike data, and only include slow component data. The single units were low-pass filtered for slow component data, and further detected with amplitude thresholding. An important compromise in this process is the missing of spikes due to a high threshold, or including false positives at lower thresholds. For optimal recordings, the threshold was set manually for each channel. To further diminish signal noise, one channel from each hemispheres with no spiking activity was chosen as a reference signal.

The spike sorting is done either manually or though the far less time consuming process of automatic clustering – with manual corrections. To eliminate possible biases with the

automatic clustering, output from manual and semi-automatic spike sorting of the same data were compared, and the semi-automatic spike sorting was found to be equally good, hence this method was chosen. The use of tetrodes allows for visualisation of a single neuron from different sites, in which spike amplitude and shape depends on the position of the electrode in relation to the cell. Spike sorting is thus highly improved with tetrodes. One tetrode can identify up to 20 cells, and is a well established method for studying connectivity patterns in clusters of cells (Harris et al., 2000).

The use of optogenetics has given great advances in neuroscience, especially in manipulation of neural populations. However, the technique requires the right prerequisites in order to work properly. The first step was to investigate the opsin expression in the neuronal tissue of interest. The opsin was tagged with a fluorescent marker and investigated by immunohistochemistry and fluorescence microscopy. Another consideration is the scattering of light in neuronal tissue by cellular structures. In addition, chromophores might absorb light (Al-Juboori et al., 2013). These two factors might lead to significant light attenuation. To deliver light with minor light deficiency into deep structures of the brain, laser light was delivered through optic fibres implanted in the brain areas of interest. The use of laser light in optogenetics might significantly damage exposed cells. The cells might be affected by the laser light or the depolarization activity empowered by the light (Mohanty and Lakshminarayananan, 2015). To minimise the damage, light output was calibrated to below 30 mW and delivered in 5 ms pulses. The 5 ms pulses enabled cells to return to resting state. The position of the tetrodes and optic fibre implants was an important factor for successful experiments, and was controlled for by staining sections for Nissl bodies to find implant tracks in the tissue.

Comments on the histology. Histology results from ChR injections and optetrode implants showed that animals with response to optogenetic manipulations had a dense ChR (GFP; 3.18) expression in the MEC region upon injections in the MS. Furthermore, optetrode tracks were observed in the MEC LII and/or LIII.

From the histology of animals with no observed response to optogenetic manipulations (fig. A.6 and A.7), the optetrodes were either displaced in other brain areas, or the ChR expression was weak. The Step-Waveform inhibition, attempted in animal 1645, was clearly unsuccessful due to low viral expression. Other causes could be faults in the construction of the microdrive with optetrodes or the implantation.

4.2.2 Electrophysiological responses to perturbations of the MS projection

Although the effect of optogenetic stimulations is only qualitatively addressed in this thesis the interpretation of the provided examples suggest important features of the network.

Increasing the frequency of the MS projection to 11 Hz, increased the dominating theta oscillations accordingly (fig. 3.16). This effect was observed in two animals, in which one grid cell activity was also recorded. The grid cells' spiking activity was modulated by the LFP both

before stimulation (8 Hz) and following the increased frequency during stimulation (11 Hz). This is similar to the increased ISI of grid cells and place cells with increased theta frequency observed during running indicating that the spiking activity is modulated by external inputs (O'keefe and Burgess, 2005). In this study, the firing rate of grid cells increased with increased theta frequency, thus the firing rate appeared to be modulated by the theta frequency. The effect of stimulation on LFP was not observed the two other animals, which may be due to misplacement of the optic fibre in the MEC, tissue damage or poor expression in the target area. From the one animal in which we also recorded grid cells, we found a strong increase in firing rate during stimulations when the rat was within the grid fields of that particular unit (fig. 3.17). In contrast, the response was much weaker when outside the grid fields. Thus, the spatial periodicity of the grid cells was not altered during MS stimulations. In other experiments, not reported here, where stimulations exceeded (15 Hz up and above) the normal theta frequency range and stimulation responses and endogenous theta activity separated, did not distort the spatial firing pattern of the grid cells. This indicates that although the grid cells follow the theta frequency, the spatial coding seems robust to perturbations of the LFP, and that the spatial coding might be dissociated from theta oscillations. In contrast to these findings, other studies (Brandon et al., 2011; Koenig et al., 2011) have found grid cell spatial periodicity to be disrupted due to abolished LFP theta frequency in the MEC during pharmacologic inactivation of the MS. Thus, there is a clear difference in grid cell responses following optogenetic perturbations and pharmacological inactivation of the MS in which the former perturbs the theta frequency, whereas the latter inactivates the MS. Another study (Bonnevie et al., 2013) found grid cell spatial periodicity to be altered during pharmacological inactivation of the hippocampus – both power and theta frequency were reduced during muscimol infusion (however this could be due to reduced running speed). As there is reciprocal connectivity between the MS, MEC and the hippocampus the input from the hippocampus might be important for the spatial periodicity of grid cells, and inactivation of the MS (Brandon et al., 2011; Koenig et al., 2011) might have affected the grid cell spatial periodicity indirectly though the hippocampus.

From stimulating in the MEC, specifically activating the MS-MEC projection, and recording single units in the MEC, inhibitory neurons showed an immediate decrease in firing rate after stimulation followed by an increase in firing rate. Similar to these findings, *in vitro* recordings of neurons in the MEC during optogenetic activation of the MS-MEC projection at theta frequency showed pausing in spiking of inhibitory interneurons (Gonzalez-Sulser et al., 2014; Fuchs et al., 2016), indicating that the MS projection inhibits inhibitory interneurons. At 10 Hz stimulation the pausing was followed by activation of the inhibitory interneurons, suggesting that the MS entrains rebound firing of entorhinal interneurons (Gonzalez-Sulser et al., 2014). In contrast, grid cells showed increased activity in response to stimulation with a short latency (fig. 3.13). A decrease in activity was observed for both grid cells and inhibitory neurons 10-20 ms after stimulation. Principal cells in the MEC are found to be interconnected via inhibitory interneurons (Couey et al., 2013; Pastoll et al., 2013), similar to what is found in

the hippocampus (Hangya et al., 2009). The MS GABAergic projection innervate inhibitory interneurons in the hippocampus (Köhler et al., 1984; Freund and Antal, 1988), suggesting that the MS controls disinhibition of principal neurons here. Thus, our analysis together with previous findings in the MEC and the hippocampus suggest that the MS projection might control grid cell activity through disinhibition (fig. 4.1).
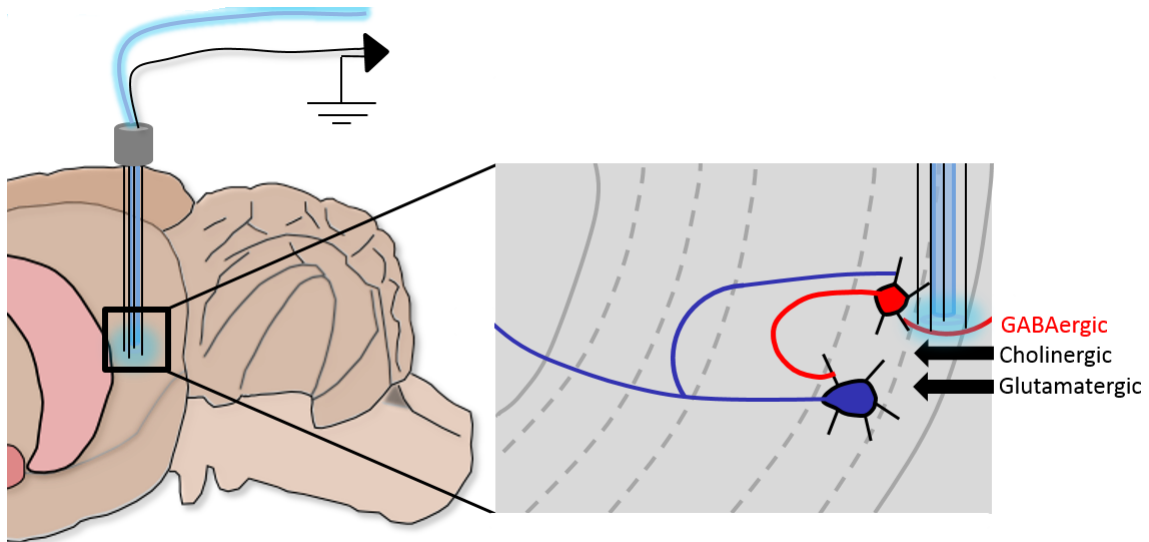
Figure 4.1: Our findings indicate that grid cells (blue) are innervated by inhibitory interneurons (red) and receives disinhibition from medial septal GABAergic neurons. In courtesy of M. Lepperød.

Furthermore, we found grid cells of varying waveforms. These preliminary results might suggest that the grid cells are of different cell types, supported by previous reports (Domnisoru et al., 2013).

In contrast to the disinhibition observed in grid cells, other non-spatial principal cells were found to respond more similar to inhibitory cells (fig. 3.14), with an immediate inhibition followed by an increase in firing rate. This might be due to the direct connections observed between the MS and pyramidal LII cells from the neurochemical analysis (fig. 3.11), suggesting direct inhibition. However, the connectivity suggested from the present study is in contrast to previous reports finding very little or no direct connectivity with principal cells (Gonzalez-Sulser et al., 2014; Fuchs et al., 2016).

Our findings that grid cells spatial firing were not altered during stimulations of the MS (fig. 3.17) or selective of the MS-MEC projection (fig. 3.13 and 3.15), indicate that grid cells spatial coding may be dissociated from theta oscillations. Studies in bats show that grid cells spatial firing is not theta frequency modulated (Yartsev et al., 2011). Notably, the authors did not find continuous theta oscillations from LFP recordings in the MEC but comparatively theta occurred in short bouts in crawling bats, and was later confirmed in flying bats (Yartsev

and Ulanovsky, 2013). The MEC neurons did weakly phase lock to the theta bouts, but grid fields existed between theta bouts and when theta bouts were removed (Yartsev et al., 2011). Studies of the subthreshold membrane potential resonance of layer II stellate cells, shown to be grid cells, found that while rat stellate cells showed theta frequency resonance activity, bat stellate cells did not Heys et al. (2013). This might suggest that theta contribution to grid cell firing is different across mammalian species and perhaps not associated with the spatial coding.

4.3 Future perspectives

The results from the present study remain preliminary and inconclusive due to sample size. Future studies with increased population sizes is necessary to confirm the reported results from both the neurochemical mapping and electrophysiological investigation.

A more extensive characterisation of the MS-MEC projection is needed. This could be conducted by, first mapping out the cholinergic part of the projection, by staining for vesicular acetylcholinetransferase (VChAT), second by revealing the potential co-release of neurotransmitters using multiple staining to include different vesicular transporters. The mapping of MEC postsynaptic targets of the MS projection should include reelin positive cells, pyramidal cells in MEC LIII and other interneurons, such as somatostatin and 5-HT$_3$A positive interneurons. Multi-coloured staining of the MS projection, vesicular transporters and cellular markers could reveal specific presynaptic input to different types of postsynaptic cells in the MEC. For specific targeting, this can be performed in transgenic rats expressing Cre recombinase in specific cell types, and by injecting a Cre-lox dependent viral tracer.

From the electrophysiology it would be interesting to silence the MS-MEC projection and record the postsynaptic responses in MEC. This approach could reveal whether inhibition of the projection could potentially activate MEC inhibitory interneurons and cause indirect inhibition of principal cells. Developments in pharmacological methods such as designer receptors exclusively activated by designer drugs (e.g. the DREADD system) and advances in optogenetic and genetic tools permit selective silencing of specific interneurons. Furthermore, optogenetic manipulation could be performed by *in vitro* patch-clamp recordings of postsynaptic responses in slice preparations. This has been studied in mice (Fuchs et al., 2016; Gonzalez-Sulser et al., 2014), but experiments in rats are lacking.

Studies on the contribution of the septal cholinergic projections to the MEC remains elusive. The techniques for studying the cholinergic neurons has until recently lacked specificity. Recent studies (Desikan et al., unpublished, abstract) investigated the MS cholinergic projection by optogenetics and *in vitro* patch-clamp recordings, and observed EPSPs in the MEC.

The electrophysiological recordings in this thesis were conducted in freely moving rats, enabling unique insight into the network activity during behaviour. To study the role of the MS-MEC projection for navigation and memory, an elongation of this study would be to include different types of behavioural experiments. These would include tasks such as the Morris'

water maze, the radial-arm maze and the T-maze (Vorhees and Williams, 2014). Moreover, the development of silicon probes for chronic recordings enabling recordings of >100 cells simultaneously will be important in studying the correlation between the septal input and modules of grid cells along the MEC DV axis. It will be important to thoroughly map out the local connectivity of the MEC network – especially targeting the interneurons surrounding the principal cells. For example by selective inactivation of PV- and SOM-positive interneurons, and recording the effect on spatially modulated cells in freely moving animals. Preliminary results (Miao et al., unpublished, abstract) indicate that inactivation of PV-positive interneurons affects grid cell periodic firing, whereas inactivating SOM-positive interneurons does not.

From the results of Bonnevie et al. (2013), in which grid cell spatial periodicity was disrupted by hippocampal inactivation and both power and theta frequency were reduced during muscimol infusion, future studies should investigate the network of the MS, MEC and the hippocampus in combination. As preliminary results from the present thesis indicate that grid cell spatial firing is resilient to perturbations of the MS projection, indirect connectivity with the hippocampus might be important for grid cell spatial coding.

4.4 Conclusions

The results from this thesis indicate that:

- a majority of the terminals projecting to MEC from MS originate from long-range inhibitory GABAergic neurons.

- the postsynaptic targets of the MS projection constitute both CB positive pyramidal layer II cells, and PV positive layer II and LIII interneurons, however, PV layer II interneurons receives a majority of the input compared to the other two populations.

- from optogenetic activation of the MS projection and recordings in the MEC, the spatial coding of grid cells might be dissociated from LFP theta oscillations.

- from activating the MS-MEC projection, inhibitory interneurons were instantaneously inhibited whereas grid cells show delayed increase in firing rate, suggesting MS disinhibition of grid cells, supported by the anatomical findings.

References

Abbott, A. (2014). How the 2014 Nobel Prize Winners Found the Brain's Own GPS. https://www.scientificamerican.com/article/how-the-2014-nobel-prize-winners-found-the-brain-s-own-gps/. [Online; accessed 28-July-2017].

Abilez, O. J., Wong, J., Prakash, R., Deisseroth, K., Zarins, C. K., and Kuhl, E. (2011). Multiscale computational models for optogenetic control of cardiac function. *Biophysical journal*, 101(6):1326–1334.

Al-Juboori, S. I., Dondzillo, A., Stubblefield, E. A., Felsen, G., Lei, T. C., and Klug, A. (2013). Light scattering properties vary across different regions of the adult mouse brain. *PloS one*, 8(7):e67626.

Alonso, A. and Köhler, C. (1984). A study of the reciprocal connections between the septum and the entorhinal area using anterograde and retrograde axonal transport methods in the rat brain. *Journal of Comparative Neurology*, 225(3):327–343.

Anikeeva, P., Andalman, A. S., Witten, I., Warden, M., Goshen, I., Grosenick, L., Gunaydin, L. A., Frank, L. M., and Deisseroth, K. (2012). Optetrode: a multichannel readout for optogenetic control in freely moving mice. *Nature neuroscience*, 15(1):163–70.

Annese, J., Schenker-Ahmed, N. M., Bartsch, H., Maechler, P., Sheh, C., Thomas, N., Kayano, J., Ghatan, A., Bresler, N., Frosch, M. P., et al. (2014). Postmortem examination of patient hm's brain based on histological sectioning and digital 3d reconstruction. *Nature communications*, 5:3122.

Aschauer, D. F., Kreuz, S., and Rumpel, S. (2013). Analysis of transduction efficiency, tropism and axonal transport of aav serotypes 1, 2, 5, 6, 8 and 9 in the mouse brain. *PloS one*, 8(9):e76310.

Barthó, P., Hirase, H., Monconduit, L., Zugaro, M., Harris, K. D., and Buzsáki, G. (2004). Characterization of neocortical principal cells and interneurons by network interactions and extracellular features. *Journal of neurophysiology*, 92(1):600–608.

Berndt, A., Lee, S. Y., Ramakrishnan, C., and Deisseroth, K. (2014). Structure-guided transformation of channelrhodopsin into a light-activated chloride channel. *Science*, 344(6182):420–424.

Bjerke, L. E. (2016). Hypothalamic circuits involved in innate defensive behavior are both gabaergic and glutamatergic. *Master thesis*.

Boccara, C. N., Kjonigsen, L. J., Hammer, I. M., Bjaalie, J. G., Leergaard, T. B., and Witter, M. P. (2015). A three-plane architectonic atlas of the rat hippocampal region. *Hippocampus*, 25(7):838–857.

Boccara, C. N., Sargolini, F., Thoresen, V. H., Solstad, T., Witter, M. P., Moser, E. I., and Moser, M.-B. (2010). Grid cells in pre- and parasubiculum. *Nature Neuroscience*, 13(8):987–994.

Bonnevie, T., Dunn, B., Fyhn, M., Hafting, T., Derdikman, D., Kubie, J. L., Roudi, Y., Moser, E. I., and Moser, M.-B. (2013). Grid cells require excitatory drive from the hippocampus. *Nature neuroscience*, 16(3):309–17.

Boulland, J.-L., Qureshi, T., Seal, R. P., Rafiki, A., Gundersen, V., Bergersen, L. H., Fremeau, R. T., Edwards, R. H., Storm-Mathisen, J., and Chaudhry, F. A. (2004). Expression of the vesicular glutamate transporters during development indicates the widespread corelease of multiple neurotransmitters. *Journal of Comparative Neurology*, 480(3):264–280.

Boyden, E. S., Zhang, F., Bamberg, E., Nagel, G., and Deisseroth, K. (2005). Millisecond-timescale, genetically targeted optical control of neural activity. *Nature neuroscience*, 8(9):1263–1268.

Brandon, M. P., Bogaard, A. R., Libby, C. P., Connerney, M. A., Gupta, K., and Hasselmo, M. E. (2011). Reduction of Theta Rhythm Dissociates Grid Cell Spatial Periodicity from Directional Tuning. *Science*, 332(6029):595–599.

Breustedt, J., Schmitz, D., Heinemann, U., and Schmieden, V. (2004). Characterization of the inhibitory glycine receptor on entorhinal cortex neurons. *European Journal of Neuroscience*, 19(7):1987–1991.

Brun, V. H. (2002). Place Cells and Place Recognition Maintained by Direct Entorhinal-Hippocampal Circuitry. *Science*, 296(5576):2243–2246.

Brun, V. H., Leutgeb, S., Wu, H. Q., Schwarcz, R., Witter, M. P., Moser, E. I., and Moser, M. B. (2008). Impaired Spatial Representation in CA1 after Lesion of Direct Input from Entorhinal Cortex. *Neuron*, 57(2):290–302.

Buzsáki, G. (2005). Theta rhythm of navigation: link between path integration and landmark navigation, episodic and semantic memory. *Hippocampus*, 15(7):827–840.

Buzsáki, G., Anastassiou, C. A., and Koch, C. (2012). The origin of extracellular fields and currents–EEG, ECoG, LFP and spikes. *Nature reviews. Neuroscience*, 13(6):407–20.

Calhoun, M. E., Jucker, M., Martin, L. J., Thinakaran, G., Price, D. L., and Mouton, P. R. (1996). Comparative evaluation of synaptophysin-based methods for quantification of synapses. *Journal of neurocytology*, 25(1):821–828.

Canto, C. B. and Witter, M. P. (2012). Cellular properties of principal neurons in the rat entorhinal cortex. ii. the medial entorhinal cortex. *Hippocampus*, 22(6):1277–1299.

Canto, C. B., Wouterlood, F. G., and Witter, M. P. (2008). What does the anatomical organization of the entorhinal cortex tell us? *Neural Plasticity*, 2008.

Caster, A. H. and Kahn, R. A. (2012). Computational method for calculating fluorescence intensities within three-dimensional structures in cells. *Cellular logistics*, 2(4):176–188.

Chaudhry, F. A., Reimer, R. J., Bellocchio, E. E., Danbolt, N. C., Osen, K. K., Edwards, R. H., and Storm-Mathisen, J. (1998). The vesicular gaba transporter, vgat, localizes to synaptic vesicles in sets of glycinergic as well as gabaergic neurons. *Journal of Neuroscience*, 18(23):9733–9750.

Chrobak, J. J., Stackman, R. W., and Walsh, T. J. (1989). Intraseptal administration of muscimol produces dose-dependent memory impairments in the rat. *Behavioral and neural biology*, 52(3):357–369.

Colgin, L. L. (2016). Rhythms of the hippocampal network. *Nature Publishing Group*, 17.

Corkin, S. (1979). Hidden-figures-test performance: lasting effects of unilateral penetrating head injury and transient effects of bilateral cingulotomy. *Neuropsychologia*, 17(6):585–605.

Couey, J. J., Witoelar, A., Zhang, S.-J., Zheng, K., Ye, J., Dunn, B., Czajkowski, R., Moser, M.-B., Moser, E. I., Roudi, Y., and Witter, M. P. (2013). Recurrent inhibitory circuitry as a mechanism for grid formation. *Nature neuroscience*, 16(3):318–24.

Desikan, S., Koser, D. E., Neitz, A., and Monyer, H. (unpublished). Cholinergic modulation of neuronal network activity in the entorhinal cortex. program no. 084.14.2016/ggg11. *Neuroscience Meeting Planner, San Diego, CA: Society for Neuroscience, 2016. Online.*

Dhillon, A. and Jones, R. S. (2000). Laminar differences in recurrent excitatory transmission in the rat entorhinal cortex in vitro. *Neuroscience*, 99(3):413–422.

Doeller, C. F., Barry, C., and Burgess, N. (2010). Evidence for grid cells in a human memory network. *Nature*, 463(7281):657–661.

Dolorfo, C. L. and Amaral, D. G. (1998). Entorhinal cortex of the rat: organization of intrinsic connections. *Journal of Comparative Neurology*, 398(1):49–82.

Domnisoru, C., Kinkhabwala, A. A., and Tank, D. W. (2013). Membrane potential dynamics of grid cells. *Nature*, 495(7440):199.

Dunnett, S. B., Everitt, B. J., and Robbins, T. W. (1991). The basal forebrain-cortical cholinergic system: interpreting the functional consequences of excitotoxic lesions. *Trends in neurosciences*, 14(11):494–501.

Ekstrom, A. D., Caplan, J. B., Ho, E., Shattuck, K., Fried, I., and Kahana, M. J. (2005). Human hippocampal theta activity during virtual navigation. *Hippocampus*, 15(7):881–889.

Etienne, A. S. and Jeffery, K. J. (2004). Path integration in mammals. *Hippocampus*, 14(2):180–192.

Ferguson, J. E., Boldt, C., and Redish, A. D. (2009). Creating low-impedance tetrodes by electroplating with additives. *Sensors and Actuators A: Physical*, 156(2):388–393.

Frahm, C., Siegel, G., Grass, S., and Witte, O. (2006). Stable expression of the vesicular gaba transporter following photothrombotic infarct in rat brain. *Neuroscience*, 140(3):865–877.

Freund, T. F. and Antal, M. (1988). Gaba-containing neurons in the septum control inhibitory interneurons in the hippocampus. *Nature*, 336(6195):170–173.

Freund, T. F. and Katona, I. (2007). Perisomatic inhibition. *Neuron*, 56(1):33–42.

Fuchs, E. C., Neitz, A., Pinna, R., Melzer, S., Caputi, A., and Monyer, H. (2016). Local and distant input controlling excitation in layer ii of the medial entorhinal cortex. *Neuron*, 89(1):194–208.

Fyhn, M., Hafting, T., Treves, A., Moser, M.-B., and Moser, E. I. (2007). Hippocampal remapping and grid realignment in entorhinal cortex. *Nature*, 446(7132):190–4.

Fyhn, M., Hafting, T., Witter, M. P., Moser, E. I., and Moser, M.-B. (2008). Grid cells in mice. *Hippocampus*, 18(12):1230–1238.

Fyhn, M., Molden, S., Witter, M. P., Moser, E. I., and Moser, M.-B. (2004). Spatial representation in the entorhinal cortex. *Science (New York, N.Y.)*, 305(5688):1258–64.

Gaykema, R., Luiten, P. G., Nyakas, C., and Traber, J. (1990). Cortical projection patterns of the medial septum-diagonal band complex. *Journal of Comparative Neurology*, 293(1):103–124.

Givens, B. and Olton, D. S. (1994). Local modulation of basal forebrain: effects on working and reference memory. *Journal of Neuroscience*, 14(6):3578–3587.

Gonzalez-Sulser, A. and Nolan, M. F. (2017). Grid cells' need for speed. *Nature neuroscience*, 20(1):1–2.

Gonzalez-Sulser, A., Parthier, D., Candela, A., McClure, C., Pastoll, H., Garden, D., Sürmeli, G., and Nolan, M. F. (2014). GABAergic projections from the medial septum selectively inhibit interneurons in the medial entorhinal cortex. *The Journal of neuroscience : the official journal of the Society for Neuroscience*, 34(50):16739–43.

Gras, C., Amilhon, B., Lepicard, E. M., Poirel, O., Vinatier, J., Herbin, M., Dumas, S., Tzavara, E. T., Wade, M. R., Nomikos, G. G., et al. (2008). The vesicular glutamate transporter vglut3 synergizes striatal acetylcholine tone. *Nature neuroscience*, 11(3):292.

Green, J. and Arduini, A. (1954). Hippocampal Electrical Activity in Arousal. *Journal of Neuro*, 17(6):533–57.

Gritti, I., Mainville, L., Mancia, M., and Jones, B. E. (1997). Gabaergic and other noncholinergic basal forebrain neurons, together with cholinergic neurons, project to the mesocortex and isocortex in the rat. *The Journal of comparative neurology*, 383(2):163–177.

Hafting, T., Fyhn, M., Bonnevie, T., Moser, M.-B., and Moser, E. I. (2008). Hippocampus-independent phase precession in entorhinal grid cells. *Nature*, 453(7199):1248–52.

Hafting, T., Fyhn, M., Molden, S., Moser, M.-B., and Moser, E. I. (2005). Microstructure of a spatial map in the entorhinal cortex. *Nature*, 436(7052):801–6.

Han, X. (2012). In vivo application of optogenetics for neural circuit analysis. *ACS chemical neuroscience*, 3(8):577–584.

Hangya, B., Borhegyi, Z., Szilágyi, N., Freund, T. F., and Varga, V. (2009). Gabaergic neurons of the medial septum lead the hippocampal network during theta activity. *Journal of Neuroscience*, 29(25):8094–8102.

Harris, K. D., Henze, D. A., Csicsvari, J., Hirase, H., and Buzsáki, G. (2000). Accuracy of tetrode spike separation as determined by simultaneous intracellular and extracellular measurements. *Journal of neurophysiology*, 84(1):401–414.

Herzog, E., Takamori, S., Jahn, R., Brose, N., and Wojcik, S. M. (2006). Synaptic and vesicular co-localization of the glutamate transporters vglut1 and vglut2 in the mouse hippocampus. *Journal of neurochemistry*, 99(3):1011–1018.

Heys, J. G., MacLeod, K. M., Moss, C. F., and Hasselmo, M. E. (2013). Bat and rat neurons differ in theta-frequency resonance despite similar coding of space. *Science*, 340(6130):363–367.

Hoon, M., Sinha, R., and Okawa, H. (2017). Using fluorescent markers to estimate synaptic connectivity in situ. *Synapse Development: Methods and Protocols*, pages 293–320.

Hu, H., Gan, J., and Jonas, P. (2014). Fast-spiking, parvalbumin+ gabaergic interneurons: From cellular design to microcircuit function. *Science*, 345(6196):1255263.

Jacobs, J., Weidemann, C. T., Miller, J. F., Solway, A., Burke, J. F., Wei, X.-X., Suthana, N., Sperling, M. R., Sharan, A. D., Fried, I., and Kahana, M. J. (2013). Direct recordings of grid-like neuronal activity in human spatial navigation. *Nature Neuroscience*, 16(9):1188–1190.

Jeffery, K. J., Donnett, J. G., and O'keefe, J. (1995). Medial septal control of theta-correlated unit firing in the entorhinal cortex of awake rats. *Neuroreport*, 6(16):2166–2170.

Jung, R. and Kornmüller, A. E. (1938). Eine methodik der ableitung iokalisierter potentialschwankungen aus subcorticalen hirngebieten. *European Archives of Psychiatry and Clinical Neuroscience*, 109(1):1–30.

Kao, Y.-H., Lassová, L., Bar-Yehuda, T., Edwards, R. H., Sterling, P., and Vardi, N. (2004). Evidence that certain retinal bipolar cells use both glutamate and gaba. *Journal of Comparative Neurology*, 478(3):207–218.

Killian, N. J., Jutras, M. J., and Buffalo, E. A. (2012). A map of visual space in the primate entorhinal cortex. *Nature*, 491(7426):761–4.

Koenig, J., Linder, A. N., Leutgeb, J. K., and Leutgeb, S. (2011). The spatial periodicity of grid cells is not sustained during reduced theta oscillations. *Science (New York, N.Y.)*, 332(6029):592–5.

Köhler, C., Chan-Palay, V., and Wu, J.-Y. (1984). Septal neurons containing glutamic acid decarboxylase immunoreactivity project to the hippocampal region in the rat brain. *Anatomy and embryology*, 169(1):41–44.

Kropff, E., Carmichael, J. E., Moser, M.-B., and Moser, E. I. (2015). Speed cells in the medial entorhinal cortex. *Nature*, 523(7561):419–24.

Kunz, L., Schröder, T. N., Lee, H., Montag, C., Lachmann, B., Sariyska, R., Reuter, M., Stirnberg, R., Stöcker, T., Messing-Floeter, P. C., Fell, J., Doeller, C. F., and Axmacher, N. (2015). Reduced grid-cell-like representations in adults at genetic risk for Alzheimer's disease. *Science (New York, N.Y.)*, 350(6259):430–3.

Maguire, E. A., Frackowiak, R. S., and Frith, C. D. (1997). Recalling routes around london: activation of the right hippocampus in taxi drivers. *Journal of neuroscience*, 17(18):7103–7110.

Maguire, E. A., Nannery, R., and Spiers, H. J. (2006). Navigation around london by a taxi driver with bilateral hippocampal lesions. *Brain*, 129(11):2894–2907.

Manns, I., Mainville, L., and Jones, B. (2001). Evidence for glutamate, in addition to acetylcholine and GABA, neurotransmitter synthesis in basal forebrain neurons projecting to the entorhinal cortex. *Neuroscience*, 107(2):249–263.

McNaughton, B. L., Battaglia, F. P., Jensen, O., Moser, E. I., and Moser, M.-B. (2006). Path integration and the neural basis of the 'cognitive map'. *Nature Reviews Neuroscience*, 7(8):663–678.

Miao, C., Cao, Q., Moser, E. I., and Moser, M. (unpublished). Parvalbumin and somatostatin expressing interneurons contribute differentially to spatial coding in the medial entorhinal cortex. program no. 084.18.2016/ss17. *Neuroscience Meeting Planner, San Diego, CA: Society for Neuroscience, 2016. Online.*

71

Mitchell, S. J. and Ranck, J. B. (1980). Generation of theta rhythm in medial entorhinal cortex of freely moving rats. *Brain research*, 189(1):49–66.

Mitchell, S. J., Rawlins, J. N., Steward, O., and Olton, D. S. (1982). Medial septal area lesions disrupt theta rhythm and cholinergic staining in medial entorhinal cortex and produce impaired radial arm maze behavior in rats. *The Journal of neuroscience : the official journal of the Society for Neuroscience*, 2(3):292–302.

Mizumori, S., Perez, G., Alvarado, M., Barnes, C., and McNaughton, B. (1990). Reversible inactivation of the medial septum differentially affects two forms of learning in rats.

Mohanty, S. K. and Lakshminarayananan, V. (2015). Optical techniques in optogenetics. *Journal of modern optics*, 62(12):949–970.

Monyer, H. (2017). Identified neuronal ensembles subdividing spatial coding in the medial entorhinal cortex. `http://sfb1134.uni-heidelberg.de/science/projects/area-a/a05/`. [Online; accessed 28-July-2017].

Morris, R. G. M., Garrud, P., Rawlins, J. N. P., and O'Keefe, J. (1982). Place navigation impaired in rats with hippocampal lesions. *Nature*, 297(5868):681–683.

Moser, E. I., Roudi, Y., Witter, M. P., Kentros, C., Bonhoeffer, T., and Moser, M.-B. (2014). Grid cells and cortical representation. *Nature Reviews Neuroscience*, 15(7):466–481.

O'keefe, J. and Burgess, N. (2005). Dual phase and rate coding in hippocampal place cells: theoretical significance and relationship to entorhinal grid cells. *Hippocampus*, 15(7):853–866.

O'Keefe, J. and Dostrovsky, J. (1971). *The hippocampus as a spatial map. Preliminary evidence from unit activity in the freely-moving rat*, volume 34.

O'Keefe, J. and Nadel, L. (1978). *The hippocampus as a cognitive map.* Clarendon Press, Oxford.

Ottem, E. N., Godwin, J. G., Krishnan, S., and Petersen, S. L. (2004). Dual-phenotype gaba/glutamate neurons in adult preoptic area: sexual dimorphism and function. *Journal of Neuroscience*, 24(37):8097–8105.

Pastoll, H., Solanka, L., van Rossum, M. C., and Nolan, M. F. (2013). Feedback inhibition enables theta-nested gamma oscillations and grid firing fields. *Neuron*, 77(1):141–154.

Paxinos, G. and Watson., C. (2007). *The rat brain in stereotaxic coordinates: hard cover edition.* Academic Press, 6th edition.

Petsche, H., Stumpf, C., and Gogolak, G. (1962). The significance of the rabbit's septum as a relay station between the midbrain and the hippocampus I. The control of hippocampus arousal activity by the septum cells. *Electroencephalography and Clinical Neurophysiology*, 14(2):202–211.

Polikov, V. S., Tresco, P. A., and Reichert, W. M. (2005). Response of brain tissue to chronically implanted neural electrodes. *Journal of neuroscience methods*, 148(1):1–18.

Purves, D. E., Augustine, G. J., Fitzpatrick, D. E., Hall, W. C., LaManita, A.-S., and White, L. E. (2012). *Neuroscience.* Sunderland, MA, US: Sinauer Associates, 5th edition.

Ramsden, H. L., Sürmeli, G., McDonagh, S. G., and Nolan, M. F. (2015). Laminar and dorsoventral molecular organization of the medial entorhinal cortex revealed by large-scale anatomical analysis of gene expression. *PLoS computational biology*, 11(1):e1004032.

Ray, S. and Brecht, M. (2016). Structural development and dorsoventral maturation of the medial entorhinal cortex. *Elife*, 5:e13343.

Ray, S., Naumann, R., Burgalossi, A., Tang, Q., Schmidt, H., and Brecht, M. (2014). Grid-layout and theta-modulation of layer 2 pyramidal neurons in medial entorhinal cortex. *Science*, 343(6173):891–896.

Reiner, A., Veenman, C. L., Medina, L., Jiao, Y., Del Mar, N., and Honig, M. G. (2000). Pathway tracing using biotinylated dextran amines. *Journal of neuroscience methods*, 103(1):23–37.

Rossant, C., Kadir, S. N., Goodman, D. F., Schulman, J., Hunter, M. L., Saleem, A. B., Grosmark, A., Belluscio, M., Denfield, G. H., Ecker, A. S., et al. (2016). Spike sorting for large, dense electrode arrays. *Nature neuroscience*, 19(4):634–641.

Rowland, D. C., Roudi, Y., Moser, M.-B., and Moser, E. I. (2016). Ten Years of Grid Cells. *Annual review of neuroscience.*

Royo, N. C., Vandenberghe, L. H., Ma, J.-Y., Hauspurg, A., Yu, L., Maronski, M., Johnston, J., Dichter, M. A., Wilson, J. M., and Watson, D. J. (2008). Specific aav serotypes stably transduce primary hippocampal and cortical cultures with high efficiency and low toxicity. *Brain research*, 1190:15–22.

Sargolini, F., Fyhn, M., Hafting, T., McNaughton, B. L., Witter, M. P., Moser, M.-B., and Moser, E. I. (2006). Conjunctive representation of position, direction, and velocity in entorhinal cortex. *Science (New York, N.Y.)*, 312(5774):758–62.

Saunders, A., Johnson, C. A., and Sabatini, B. L. (2012). Novel recombinant adeno-associated viruses for cre activated and inactivated transgene expression in neurons. *Frontiers in neural circuits*, 6.

Scoville, W. B. and Milner, B. (1957). Loss of recent memory after bilateral hippocampal lesions. *J. Neurol. Neurosurg. Psychiat*, 20.

Siegel, G. J. et al. (1999). *Basic neurochemistry: molecular, cellular and medical aspects.* Number V360 SIEb.

Skaggs, W. E., McNaughton, B. L., Wilson, M. A., and Barnes, C. A. (1996). Theta phase precession in hippocampal neuronal populations and the compression of temporal sequences. *Hippocampus*, 6(2):149–72.

Solstad, T., Boccara, C. N., Kropff, E., Moser, M.-B., and Moser, E. I. (2008). Representation of geometric borders in the entorhinal cortex. *Science (New York, N.Y.)*, 322(5909):1865–8.

Soudais, C., Laplace-Builhe, C., Kissa, K., and Kremer, E. J. (2001). Preferential transduction of neurons by canine adenovirus vectors and their efficient retrograde transport in vivo. *The FASEB Journal*, 15(12):2283–2285.

Steffenach, H.-A., Witter, M., Moser, M.-B., and Moser, E. I. (2005). Spatial memory in the rat requires the dorsolateral band of the entorhinal cortex. *Neuron*, 45(2):301–313.

Stensola, H., Stensola, T., Solstad, T., Frøland, K., Moser, M.-B., and Moser, E. I. (2012). The entorhinal grid map is discretized. *Nature*, 492(7427):72–78.

Sun, C., Kitamura, T., Yamamoto, J., Martin, J., Pignatelli, M., Kitch, L. J., Schnitzer, M. J., and Tonegawa, S. (2015). Distinct speed dependence of entorhinal island and ocean cells, including respective grid cells. *Proceedings of the National Academy of Sciences*, 112(30):9466–9471.

Tang, Q., Ebbesen, C. L., Sanguinetti-Scheck, J. I., Preston-Ferrer, P., Gundlfinger, A., Winterer, J., Beed, P., Ray, S., Naumann, R., Schmitz, D., et al. (2015). Anatomical organization and spatiotemporal firing patterns of layer 3 neurons in the rat medial entorhinal cortex. *Journal of Neuroscience*, 35(36):12346–12354.

Tóth, K., Freund, T. F., and Miles, R. (1997). Disinhibition of rat hippocampal pyramidal cells by gabaergic afferents from the septum. *The Journal of physiology*, 500(2):463–474.

Tulving, E. et al. (1972). Episodic and semantic memory. *Organization of memory*, 1:381–403.

Ulanovsky, N. and Moss, C. F. (2007). Hippocampal cellular and network activity in freely moving echolocating bats. *Nature Neuroscience*, 10(2):224–233.

Unal, G., Joshi, A., Viney, T. J., Kis, V., and Somogyi, P. (2015). Synaptic Targets of Medial Septal Projections in the Hippocampus and Extrahippocampal Cortices of the Mouse. *Journal of Neuroscience*, 35(48):15812–15826.

Vanderwolf, C. (1969). Hippocampal electrical activity and voluntary movement in the rat. *Electroencephalography and Clinical Neurophysiology*, 26(4):407–418.

Varga, V., Hangya, B., Kránitz, K., Ludányi, A., Zemankovics, R., Katona, I., Shigemoto, R., Freund, T. F., and Borhegyi, Z. (2008). The presence of pacemaker hcn channels identifies theta rhythmic gabaergic neurons in the medial septum. *The Journal of physiology*, 586(16):3893–3915.

Vorhees, C. V. and Williams, M. T. (2014). Assessing spatial learning and memory in rodents. *ILAR journal*, 55(2):310–332.

Wilson, M. A. and McNaughton, B. L. (1993). Dynamics of the hippocampal ensemble code for space. *Science (New York, N.Y.)*, 261(5124):1055–8.

Winson, J. (1978). Loss of hippocampal theta rhythm results in spatial memory deficit in the rat. *Science*, 201(4351):160–163.

Witter, M. P. and Amaral, D. G. (2004). CHAPTER 21: Hippocampal Formation. In *The Rat Nervous System*, pages 635–704.

Wouterlood, F. G., Canto, C. B., Aliane, V., Boekel, A. J., Grosche, J., Härtig, W., Beliën, J. A., and Witter, M. P. (2007). Coexpression of vesicular glutamate transporters 1 and 2, glutamic acid decarboxylase and calretinin in rat entorhinal cortex. *Brain Structure and Function*, 212(3-4):303–319.

Yartsev, M. M. and Ulanovsky, N. (2013). Representation of three-dimensional space in the hippocampus of flying bats. *Science*, 340(6130):367–372.

Yartsev, M. M., Witter, M. P., and Ulanovsky, N. (2011). Grid cells without theta oscillations in the entorhinal cortex of bats. *Nature*, 479(7371):103–107.

Yizhar, O., Fenno, L. E., Davidson, T. J., Mogri, M., and Deisseroth, K. (2011). Optogenetics in neural systems. *Neuron*, 71(1):9–34.

Zander, J.-F., Münster-Wandowski, A., Brunk, I., Pahner, I., Gómez-Lira, G., Heinemann, U., Gutiérrez, R., Laube, G., and Ahnert-Hilger, G. (2010). Synaptic and vesicular coexistence of vglut and vgat in selected excitatory and inhibitory synapses. *Journal of Neuroscience*, 30(22):7634–7645.

Ziegler, D. R., Cullinan, W. E., and Herman, J. P. (2002). Distribution of vesicular glutamate transporter mrna in rat hypothalamus. *Journal of Comparative Neurology*, 448(3):217–229.

Zinchuk, V. and Grossenbacher-Zinchuk, O. (2009). Recent advances in quantitative colocalization analysis: focus on neuroscience. *Progress in histochemistry and cytochemistry*, 44(3):125–172.

List of abbreviations

5-HT3A 5-hydroxytryptamine 3A

AAV   adeno-associated virus

AP   anterioposterior

BSA   bovine serum albumin

CA   cornu ammonis

CB   calbindin

ChR   channelrhodopsin

CNS   central nervous system

Cre   Cre recombinase

DIO   double-floxed inverse open reading frame

DREADD designer receptors exclusively activated by designer drugs

DV   dorsoventral

EC   entorhinal cortex

EPSP   excitatory postsynaptic potential

GABA   Gamma-Aminobutyric acid

GFP   green fluorescent protein

i.p.   intraperitoneal

IPSP   inhibitory postsynaptic potential

LFP   local field potential

MEC   medial entorhinal cortex

ML   mediolateral

MS   medial septum

PBS   phosphate buffered saline

PCP4   Purkinje cell protein 4

PFA   parafomaldehyde

PV   parvalbumin

RE   reelin

s.c.   subcutaneous

SOM   somatostatin

SwiChR step-waveform inhibitory channelrhodopsin

VChaT vesicular acetylcholinetransferase

VGAT vesicular GABA transporter

VGLUT vesicular glutamate transporter

5   Appendix

5.1   Solutions for immunohistochemistry and histochemistry

5.1.1   10xPBS

80g	NaCl
2.0g	KCl
14.4g	Na_2HPO_4
2.4g	KH_2PO_4

- Dissolve in 800 ml ddH_2O, adjust to pH 7.4, and adjust volume to 1L

- Dilute 1:10 with ddH_2O

5.1.2   Cresyl violet staining

0.5g	cresyl violet acetate
1.25 mL	glacial acetic acid
500 mL	dH_2O

- Heat to 60^oC and filter before use

5.1.3   4% PFA

40g	PFA
1L	1X PBS

- Heat to $50\text{-}60^oC$, leave with stirring until everything is dissolved (3-4 hours)

- Filter before use

5.2   Immunohistochemistry and histochemistry protocols

5.2.1   Co-staining for mCherry and VGAT, VGLUT1 or VGLUT2

- Primary antibodies: chicken anti-mCherry (1:20 000) and rabbit anti-VGAT/VGLUT1/VGLUT2 (1:5000)

- Secondary antibody: goat anti-chicken Alexa 594 and goat anti-rabbit Alexa 488 (1:200)

- Blocking solution: 1% BSA, 0.02% Triton x-100 in 1xPBS

1. Rinse sections 3x5 min in 1xPBS

2. Block sections for 1 hour, room temp.

3. Incubate sections with primary antibodies in block overnight, room temp.

4. Rinse sections 3x5 min in 1xPBS

5. Incubate sections with secondary antibody in 1xPBS for 1 hour, room temp.

6. Rinse sections 3x5min in 1xPBS

7. Mount sections, leave to dry

8. Rinse in dH$_2$O, leave to dry

9. Mount with Fluorsave and coverglass

5.2.2 Co-staining for mCherry and CB, PV or RE

- Primary antibodies: chicken anti-mCherry (1:20 000) and rabbit anti-CB, goat anti-PV or mouse anti-RE (1:1000)

- Secondary antibody: goat anti-chicken Alexa 594 (1:5000) and goat anti-rabbit Alexa 488 (1:5000), donkey anti-goat or donkey anti-mouse (1:1000)

- Blocking solution: 1% BSA, 0.02% Triton x-100 in 1xPBS

- The protocol described in section 5.2.1 was changed to 2 hours incubation in secondary antibody

5.2.3 Staining for GFP

- Primary antibody: chicken anti-GFP

- Secondary antibody: goat anti-chicken Alexa 488

- Blocking solution: 1% BSA, 0.02% Triton x-100 in 1xPBS

- The protocol followed as described in section 5.2.2

Additional steps for fluorescent Nissl staining following secondary antibody staining

- Incubate sections with Neurotrance 530/615 (1:100) for 30 min

- Incubate sections with 0.1% Triton X-100 in 1xPBS

- Rinse in 2x5 min in 1xPBS

5.2.4   Nissl staining with Cresyl violet

1. Immerse dry sections in a 1:1 chloroform: 100% ethanol solution overnight in the fume hood, in order to fixate sections to the slide

2. Hydrate the sections by immersing in

    (a) 100 % ethanol for 2 min

    (b) 90 % ethanol for 2 min

    (c) 80 % ethanol for 2 min

    (d) 70 % ethanol for 2 min

    (e) dH_2O for 2 min

3. Immerse the sections in cresyl violet solution for 6-10 min

4. Dehydrate the sections by immersing in

    (a) dH_2O for 2 min

    (b) 70 % ethanol for 2 min

    (c) 80 % ethanol for 2 min

    (d) 90 % ethanol for 2 min

    (e) 96 % ethanol with acetic acid for 1-5 min depending on the colour fading

    (f) 100 % ethanol for 2 min

    (g) Xylene for 5-15 min

5. Cover with Entellan and a coverglass.

6. Leave in fume hood overnight to dry

5.3 Supplementary tables and figures

5.3.1 Coordinates for implant surgeries

Table A.1: Coordinates for stereotaxic surgery (Paxinos and Watson., 2007) of optetrode and optic fibre implants in MEC and MS. From anterioposterior (AP) relative to the sinus (S) or bregma (B), mediolateral (ML) relative to the midline, and dorsoventral (DV) relative to bregma (mm), and angles (º).

Animal #	Left MEC optetrode				Right MEC optetrode				MS optic fibre			
	AP	ML	DV	Angle	AP	ML	DV	Angel	AP	ML	DV	Angle
1601	S0.5	4.5	1.8	12	S0.5	4.5	1.95	12	N/A	N/A	N/A	N/A
1602	S0.5	4.5	1.8	12	S0.5	4.5	1.8	12	N/A	N/A	N/A	N/A
1596	S0.5	4.6	1.8	12	S0.5	4.6	1.7	12	B0.6	1	6.3	10
1597	S0.5	4.6	1.8	13	S0.5	4.6	1.8	13	B0.6	1	6.3	10
1645	S0.4	4.5	1.8	N/A	S0.5	4.5	1.8	N/A	B0.6	0	5.6	0
1681	S0.4	4.5	2	15	S0.4	4.5	2.3	15	B0.6	0	6.7	0
1682	S0.4	4.5	1.8	15	S0.4	4.5	1.7	15	B0.6	0	6.7	0
1684	S0.4	4.5	2	15	S0.4	4.5	1.8	15	B0.6	0	6.5	0
1685	S0.4	4.5	1.8	15	S0.4	4.5	1.8	15	B0.6	0	6.5	0

5.3.2 List of antibodies and stains

Table A.2: List of antibodies and stains used for immunohistochemistry

Antibody/stain	Product number	Reference
Chicken anti-GFP	A10262	Thermo Fisher Scientific, Norway
Chicken anti-mCherry	ab205402	abcam, Norway
Rabbit anti-VGLUT1	135rb	Gifts from the lab of
Rabbit anti-VGLUT2	136rb	Prof. F. A. Chaudhry,
Rabbit anti-VGAT	138rb	Domus Medica, Oslo
Rabbit anti-calbindin D-28k	CB38	Swant, Switzerland
Goat anti-PV	DGV214	Swant, Switzerland
Mouse anti-reelin	ab78540	abcam, Norway
Mouse anti-Cre	MAB3120	Merck, Germany
DAPI Fluoromount-G®	0100-20	SouthernBiotech, USA
NeuroTrace® 530/615	N21482	
Alexa Fluor® 488 goat anti-chicken	A11039	
Alexa Fluor® 594 goat anti-chicken	A11042	Thermo Fisher Scientific, Norway
Alexa Fluor® 488 goat anti-rabbit	A11034	
Alexa Fluor® 488 donkey anti-goat	A11055	
Alexa Fluor® 594 donkey anti-mouse	A21203	

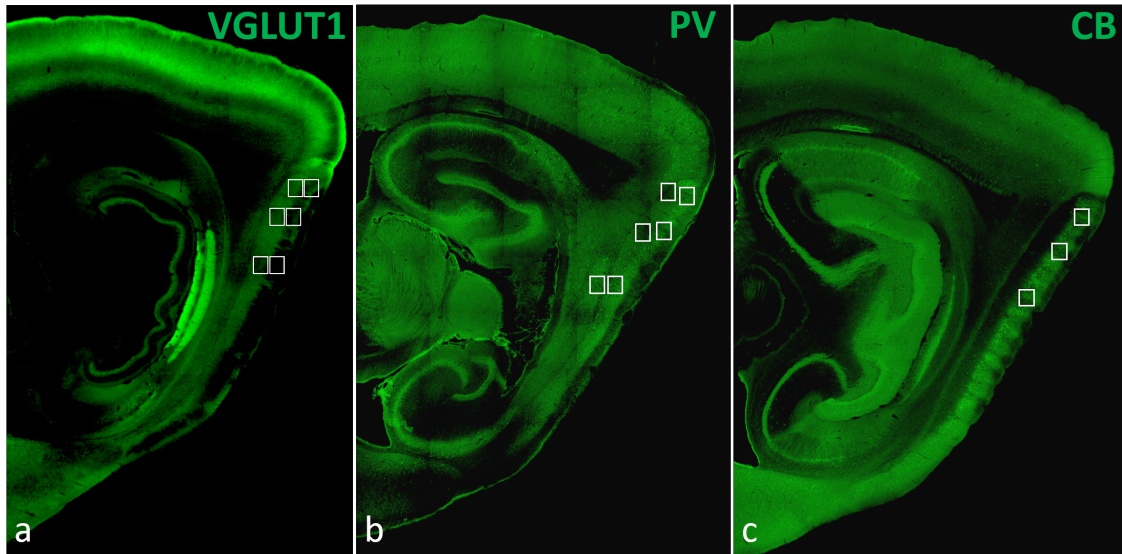### 5.3.3   Confocal microscopy imaging areas

Figure A.1: Examples of widefield images obtained following confocal imaging for (a) VGLUT1, (b) PV and (c) CB. The respective areas were bleached intentionally through the confocal microscope to enable specific localisation of imaging areas.
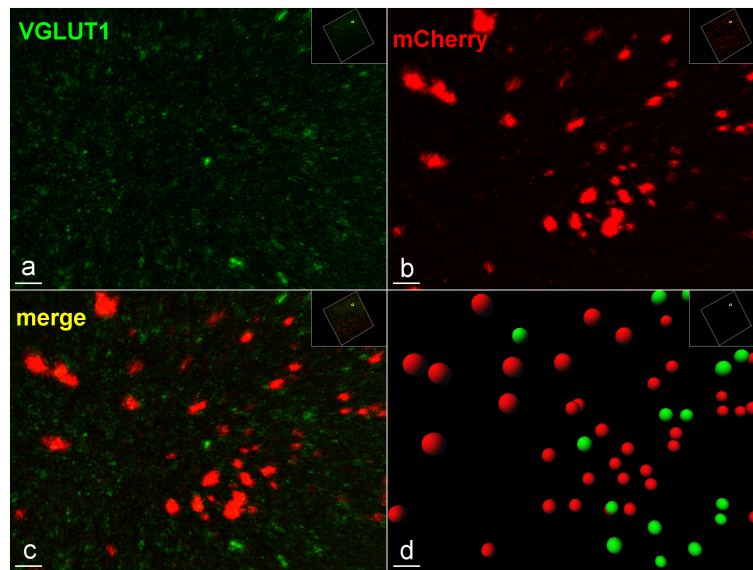
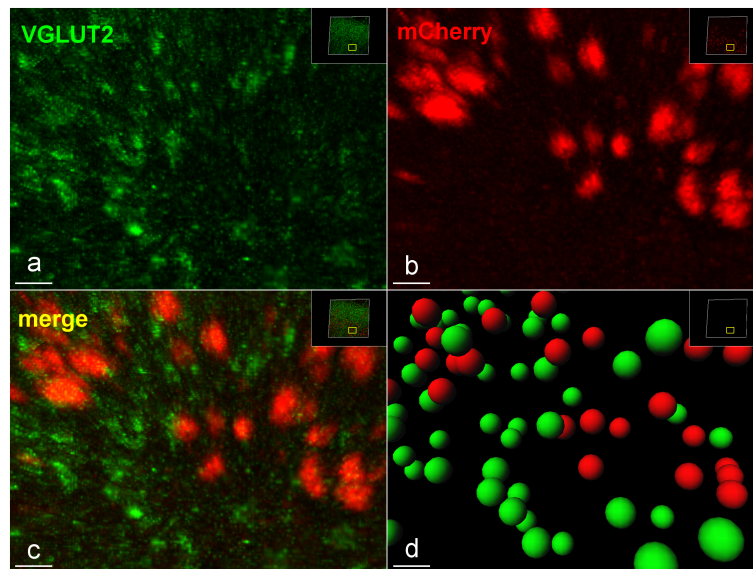### 5.3.4 Punctum-to-punctum analysis of VGLUT1/2

Figure A.2: Confocal images at high magnification showing (a) medial septal (MS) presynaptic terminals (red) in the medial entorhinal cortex, (b) co-stained for vesicular glutamate transporter 1 (VGLUT1) (green). (c) Co-expression of MS terminals and VGLUT1 (yellow). (d) Punctum-to-punctum analysis by reconstructing spheres (1 mm^3) using a spot algorithm. Scale bars: 2 mm.

Figure A.3: Confocal images at high magnification showing (a) medial septal (MS) presynaptic terminals (red) in the medial entorhinal cortex, (b) co-stained for vesicular glutamate transporter 2 (VGLUT2) (green). (c) Co-expression of MS terminals and VGLUT2 (yellow). (d) Punctum-to-punctum analysis by reconstructing spheres (1 mm^3) using a spot algorithm. Scale bars: 2 mm.

5.3.5   Single unit responses to optogenetic perturbations of the MS-MEC projection
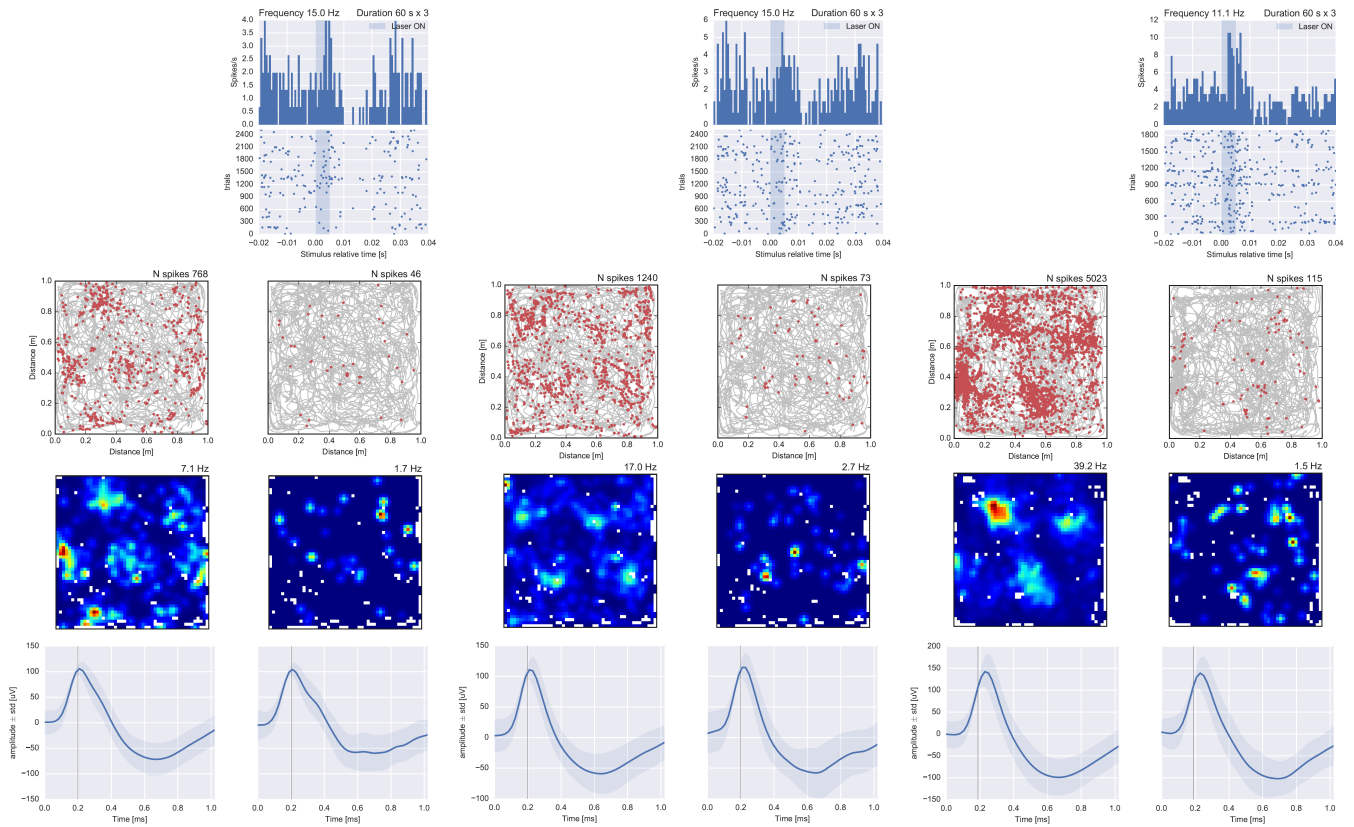

Figure A.4: Grid cell responses to optogenetic activation of the medial septum projection to the medial entorhinal cortex. Examples of three recorded grid cells in rat 1602 (Light pulses were delivered at 11 Hz for 60 seconds and each light pulse lasted 5 ms). Top panels: spike time histogram showing spikes per trial relative to stimulus onset. Below in rasterplot showing every spike. Middle panels: rat running path in grey with red dots showing spike activity. Colour coded rate map, in which increased firing rate is indicated in warmer colours. Bottom panels: single unit waveform before (left panels) and during (right panels) stimulation.
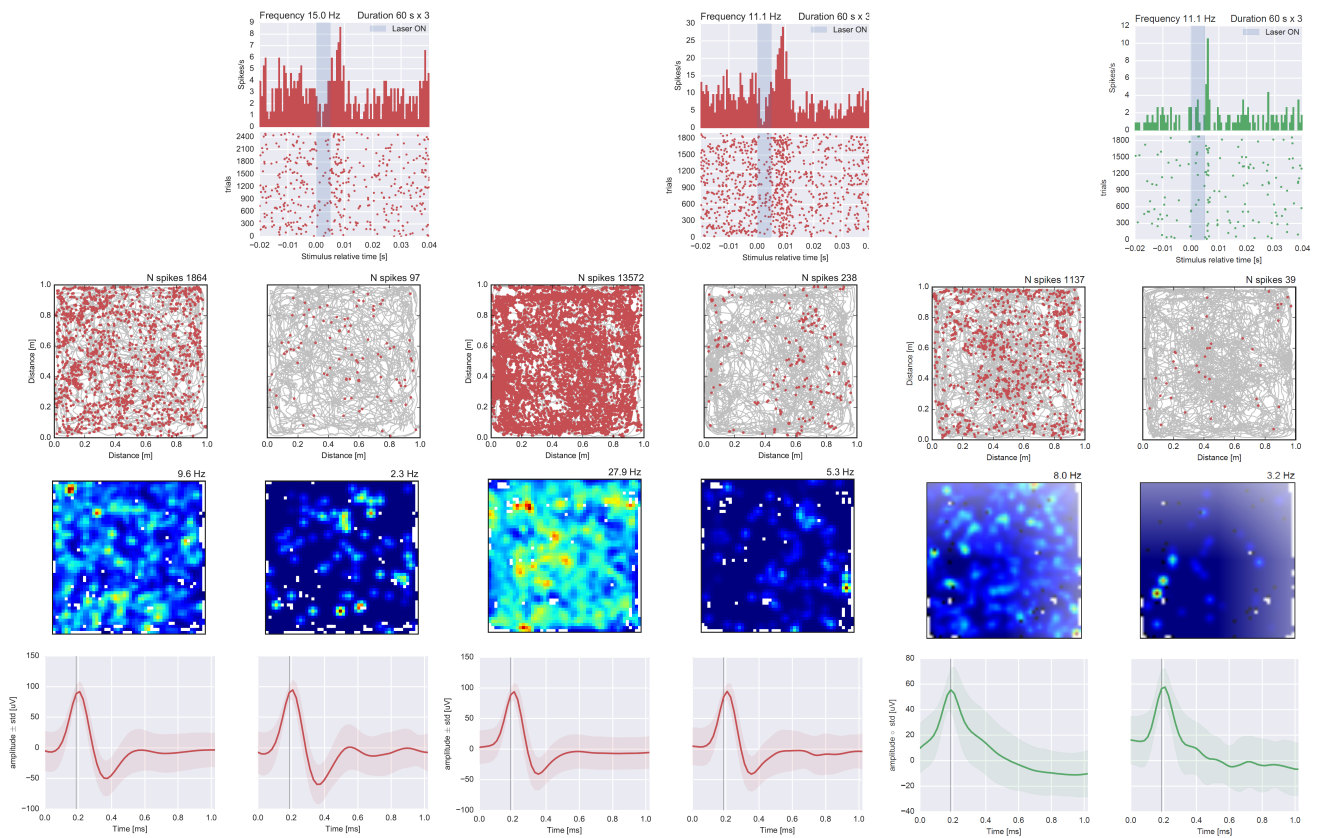
Figure A.5: Single unit responses to optogenetic activation of the medial septum projection to the medial entorhinal cortex. Examples of two inhibitory neurons in red and one non-spatial excitatory neuron in green, in rat 1602 (Light pulses were delivered at 11 Hz for 60 seconds and each light pulse lasted 5 ms). Top panels: spike time histogram showing spikes per trial relative to stimulus onset. Below in rasterplot showing every spike. Middle panels: rat running path in grey with red dots showing spike activity. Colour coded rate map, in which increased firing rate is indicated in warmer colours. Bottom panels: single unit waveform before (left panels) and during (right panels) stimulation.

5.3.6 MEC optetrode tracks

Animals without respons to optogenetics

#1681 Right

Lateral 4.32 mm
Implant 1356 µm

#1681 Left

MEC LII/III
Lateral 4.6 mm
Implant 4592 µm

 # 1682 Right **Nissl**

MEC LII/III
Lateral 4.2 mm
Implant 4205 µm

#1682 Left

Lateral 4.32 mm

#1645 Right

MEC LIII
Lateral 4.2 mm
Implant 3286 µm

 # 1645 Left

Lateral 3.9 mm
Implant 3286 µm

#1697 Right

MEC LIII
Lateral 4.2 mm
Implant 2992 µm

#1697 Left

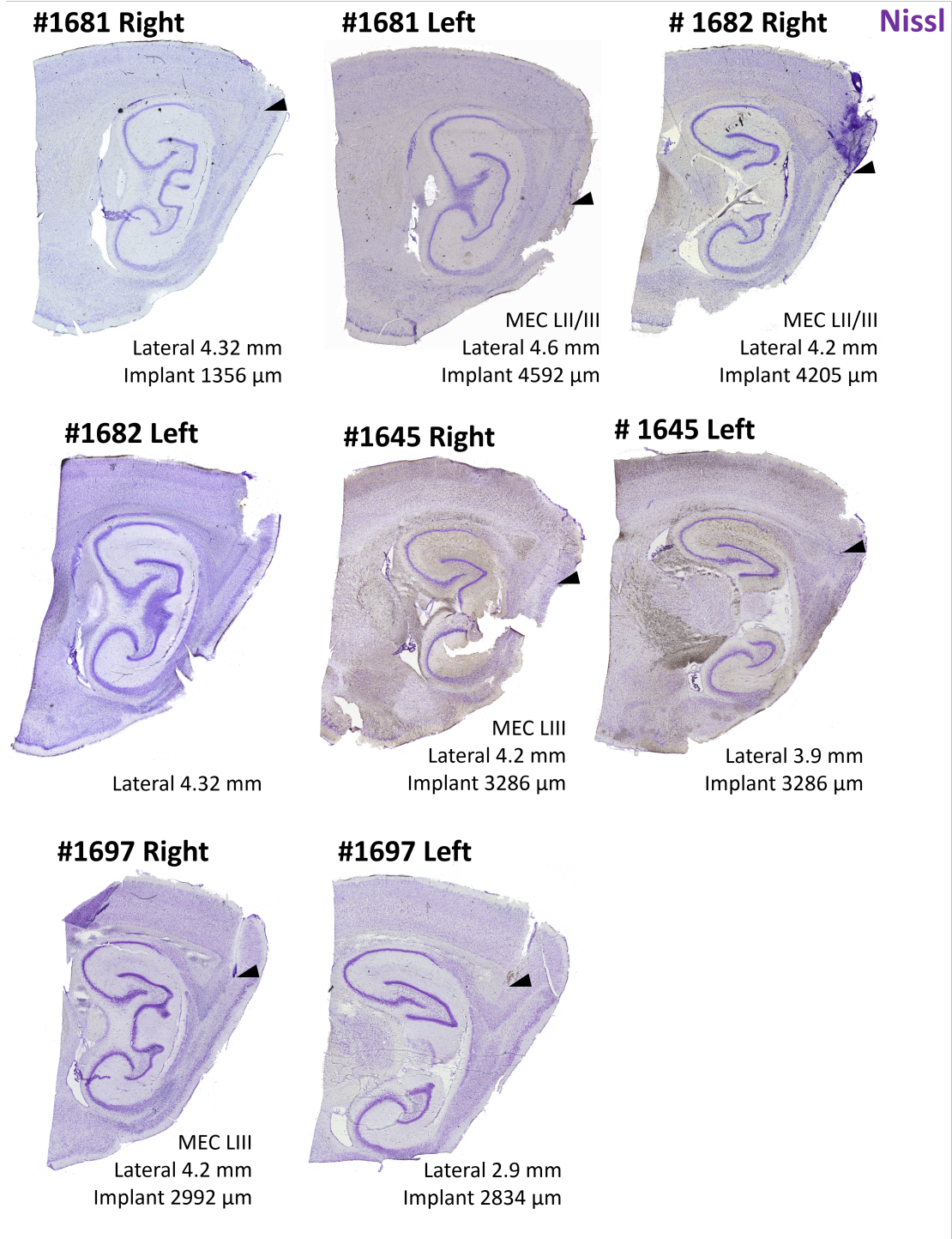Lateral 2.9 mm
Implant 2834 µm

Figure A.6: Sections stained for Nissl bodies to verify optetrode positions, for animals without response to optogenetics. Black arrows indicate deepest found DV and ML tetrode position measured along the tetrode track.

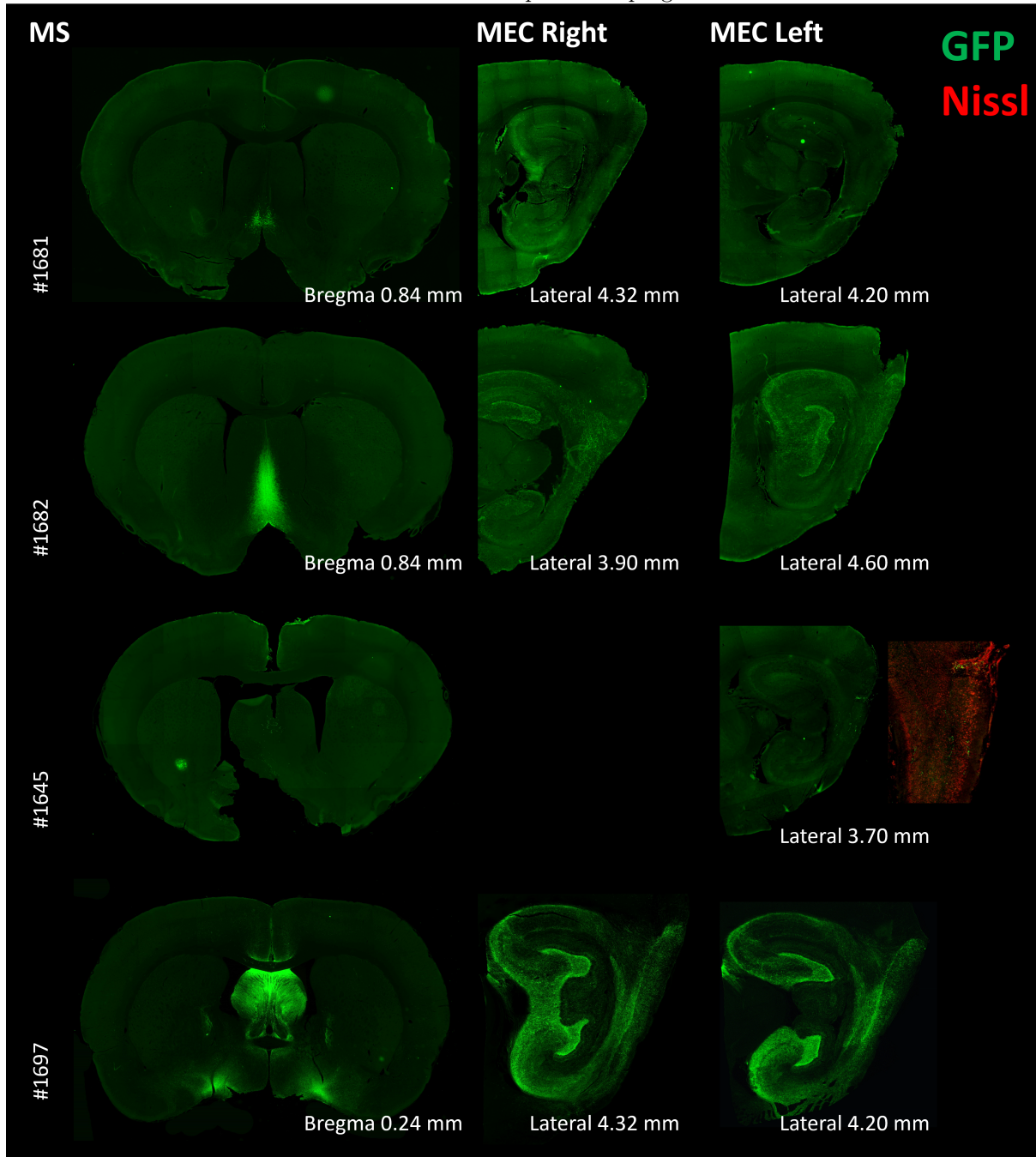### 5.3.7   MS-MEC viral expressions of ChR-GFP

Figure A.7: Viral expression of ChR fused with GFP tag, immunohistochemically stained for GFP proteins (green), and #1645 additionally stained for Nissl bodies (red) for rats without response to optogenetics. Coordinates are noted as AP for coronal sections and ML for sagittal sections.